# Design and Analysis of a Model Based Low Level Slip Controller Based on a Hybrid Braking System

## K.H.B. Lubbers

Master of Science Thesis

Delft University of Technology

Delft Center for Systems and Control

# Design and Analysis of a Model Based Low Level Slip Controller Based on a Hybrid Braking System

Master of Science Thesis

For the degree of Master of Science in Systems and Control at Delft University of Technology

K.H.B. Lubbers

April 9, 2014

Faculty of Mechanical, Maritime and Materials Engineering (3mE) · Delft University of Technology

The work in this thesis was supported by TNO Automotive Integrated Safety. Their cooperation is hereby gratefully acknowledged.

Delft University of Technology
Department of
Delft Center for Systems and Control (dcsc)

The undersigned hereby certify that they have read and recommend to the Faculty of Mechanical, Maritime and Materials Engineering (3mE) for acceptance a thesis entitled

Design and Analysis of a Model Based Low Level Slip Controller Based on a Hybrid Braking System

by

K.H.B. Lubbers

in partial fulfillment of the requirements for the degree of

Master of Science Systems and Control

Dated: April 9, 2014

Supervisor(s):

dr.ir. S. Kanarachos

dr.ir. M. Corno

Reader(s):

prof.dr.ir. E.G.M. Holweg

dr. G.A.D. Lopes

# Abstract

In the past decades, car manufacturers have improved the safety of road vehicles significantly. Besides passive safety measures like seat belts and airbags a lot of development has taken place in the field of active safety measures. Since 2011 all new car models being sold in the EU have to be equipped with an Electronic Stability Program (ESP), while since 2007 an Anti-lock Braking System (ABS) was already mandatory.

Since the introduction of the Toyota Prius in 1997 car manufacturers invested enormous amounts of resources on the development of hybrid and electric drive trains. Adding an electric motor to the vehicle increases both the complexity as well as the potential to recuperate energy while braking. Although this additional actuator is exploited during nominal driving conditions, in case of emergency braking the potential of the electric motor is often neglected and traditional ABS algorithms are evoked.

In this work the effect of incorporating the electric motor into the ABS algorithm will be investigated. For simulation and validation of the slip controller in combination with the control allocator Matlab/Simulink and CarSim will be used.

# Table of Contents

# List of Figures

# List of Tables

# Acknowledgments

I would like to thank everybody who has helped and supported me during my entire studies at Delft University of Technology and especially during my thesis work. It has been an exciting and interesting experience during which I have learned a lot, made a lot of friends and created a lot of memories.

I want to thank dr. ir. Matteo Corno and dr. ir. Stratis Kanarachos in special, being my supervisors at respectively Delft University of Technology and TNO Automotive. During my internship at TNO Automotive Stratis was a great support, showing a lot of patience and sharing some great insides into the subject of my work. Matteo has supported me throughout this entire project, keeping me on track and making me focus on the relevant matters. Whenever I got stuck, Matteo was there to help me along. The help of both Matteo and Stratis is hereby greatly appreciated.

Delft, University of Technology K.H.B. Lubbers
April 9, 2014

# Chapter 1

# Introduction

## 1-1 Motivation

The single most important active safety system in modern vehicles is the Anti-lock Braking System (ABS). A tire's potential to exert lateral forces degrades with increasing longitudinal slip, rendering the vehicle unsteerable when wheel-lock occurs. The longitudinal (braking) force exerted by the tire shows a maximum in the interval of 10% - 25% slip. Considering this knowledge, the primary goal of ABS is maintaining steerability by limiting the wheel slip. The secondary goal is minimizing the stopping distance. By regulating the slip to the value that maximizes the longitudinal braking force both goals are met.

The need for minimizing the vehicles' fuel consumption and $CO_2$ emissions has led the automotive industry to develop hybrid and electrical drive train technologies. According to [1], the well-to-wheels efficiency of an internal combustion engine (ICE) vehicle is ca. 14%, while this value for electric vehicles is ca. 20% and for gasoline hybrid vehicles it is ca. 26%.

Regenerative braking is key in increasing the efficiency of (hybrid) electric vehicles. In [2], the percentage of braking energy to traction energy is given for 5 different drive cycles. The percentages range from 34.0% up to 81.9% (see table 1-1).

**Table 1-1:** Percentage of braking energy to traction energy for 5 different drive cycles

| | FTP75 Urban | LA92 | US06 | New York | ECE15 |
|---|---|---|---|---|---|
| % braking energy / traction energy | 55.4 | 58.01 | 40.73 | 81.9 | 34.08 |

In literature many publications on hybrid braking (the combination of regenerative and friction braking) can be found, but most of these researches focus on maximizing the energy recuperation during normal braking conditions ([2],[3],[4]). Very little can be found on hybrid braking during emergency situations. In [5],[6] and [7] hybrid ABS algorithms are proposed, but the electric motors are assumed to drive separate wheels and are directly coupled to them. This is not the case in most commercially available vehicles.

In the automotive industry several hybrid ABS applications can be found (for example in the Toyota Prius), but these car manufacturers are not willing to share the control details publicly.

The goal of this work is to design an ABS control strategy for (hybrid) electric vehicles currently on the market, which combines the favorable properties of both actuators to negate the negative properties of these actuators. This control strategy consists of two steps. The first step is the design of a controller to regulate the slip. In the second step, a control allocator is responsible for distributing the required braking torque over the different actuators.

## 1-2 Considered Vehicle Architecture

First we need to determine the type of vehicle we want to design a hybrid ABS algorithm for. Electric and hybrid electric vehicles can have lots of different driveline architectures. For example electric vehicles can have several motors driving separate wheels or axles, or just one motor driving one axle. The amount of different drivelines for hybrid electric vehicles is even greater, but can be categorized in three different types:

- Series hybrid
- Parallel hybrid
- Series-parallel hybrid

We will not treat all types in great detail, but a short summary of the (dis)advantages of the different types of hybrid drivelines is given.

### Series Hybrid

In a series hybrid vehicle ([2],[8]), the traction is governed only by an electric motor. The coupling of the electric motor and the ICE is done electronically. The electric energy can be supplied by a battery which will be (re)charged by the ICE driving a generator.

Advantages of series hybrid vehicles are:

- The ICE and wheels are not mechanically coupled. This means that the ICE can operate in its maximum efficiency region on the power map. It also allows us to use high speed engines like gas turbines and engines with slow dynamics like the Stirling engine which are more efficient.
- The torque-speed characteristics of electric motors makes multi-gear transmissions obsolete, resulting in less complex and costly drive train structures.
- The drivability of the vehicle can be greatly enhanced by implementing multiple electric motors to propel the different wheels.

- The modeling and control of regenerative braking is simplified since there are no gearbox and ICE coupled to the electric motor, which otherwise would have introduced additional dynamics. Also the model and control algorithm do not have to be robust with respect to changes in gear or (dis)engaging the clutch.

Disadvantages are:

- The energy from the engine is converted twice. Depending on the efficiencies of the generator and motor, the energy losses can be significant.
- The generator adds costs and weight and requires more space.
- The motor has to be powerful enough to achieve good vehicle performance, since it is the only actuator propelling the wheels.

Driving a series hybrid vehicle is especially advantageous in an urban area, where lots of stopping and accelerating takes place. Series hybrid vehicles can be front wheel driven, like the Opel Ampera or Chevrolet Volt, rear while driven like the Lexus GS 450h or even four wheel driven.

#### Parallel Hybrid

Opposite to the series hybrid configuration, the ICE and the electric motor are mechanically coupled in the parallel hybrid configuration ([2],[8]). The coupling can be done in two forms: torque and speed coupling.

Advantages of this parallel hybrid approach compared to the series hybrid approach are:

- the redundancy of a generator
- the need for a smaller electric motor
- the lack of conversion of mechanical power produced by the ICE to electric power

Disadvantages are:

- the increased complexity of the system
- the ICE no longer being able of running at its optimal efficiency
- the reduced maximum regenerative braking power
- the increased complexity of regenerative braking control

The disadvantages of increased complexity of the system and of the regenerative braking control can be overcome by letting the ICE drive the front axle and the electric motor drive the rear axle. This architecture is used for example in the BMW Concept Active Tourer and Citroën DS5 Hybrid4.

### Series-Parallel Hybrid

The series-parallel approach ([2],[8]) combines the advantages of the series hybrid and parallel hybrid configurations. The ICE can operate at its optimal efficiency while part of the power delivered by the ICE bypasses the conversion to electrical power. The complexity of the system is however increased compared to the former two approaches.

Examples of series-parallel hybrid cars on the market are the Toyata Prius, BMW X6 Active-Hybrid (no longer for sale) and the Mercedes M-Class Hybrid.

### Considered Driveline in this Work

The differences among the different types of hybrid vehicles are quite significant. Depending on the type of architecture chosen, the differences in motor size are large. For series hybrid and full-electric vehicles, the electric motor needs to be powerful enough to drive the car at high speeds. For (series-) parallel hybrid vehicles, the electric motor will be supported by the ICE at high speeds and can be less powerful. The power of the motor is directly related to the amount of energy which can be recuperated and braking torque which can be exerted by the electric motor.

Regardless of the choice of type of powertrain, car manufacturers can design front-, rear- and all-wheel drive systems. However, only when implementing multiple electric motors the wheels can be controlled independently. Controlling the braking torques on each wheel independently is advantageous in both Traction Control System (TCS) and ABS braking maneuvers since then each wheel can exert the maximum amount of driving/braking force possible on the road.

Also, when the wheels are driven individually, drive shafts can be shortened or even omitted. This is a big advantage since drive shafts introduce additional dynamics to the system, resulting in losses and vibrations.

In this work, we will consider a parallel hybrid architecture like the one shown in figure 1-1. The ICE will drive the front wheels and the rear wheels will be driven by the electric motor. This choice is based on the reduced complexity by decoupling the motor from the engine, the advantage of having a 4-wheel drive for TCS implementation and the increased interest big OEMs like PSA and BMW have displayed for this architecture.

## 1-3 Main Contribution

For a significant part, this work is inspired by [5]. It treats the problem of wheel slip control in an electric vehicle driven by 4 in-wheel motors. The motor and Hydraulic Actuated Brake (HAB) dynamics are both modeled using first order time-delayed transfer functions. The dynamics of the motor are assumed to be much faster than those of the HAB.

A robust adaptive slip controller is presented consisting of a feedback linearisation term and a proportional control term. When we assume perfect feedback linearisation, the slip error decays exponentially to zero due to the proportional control term. To accommodate the feedback linearisation an online tire force estimator is designed as an integral part of the

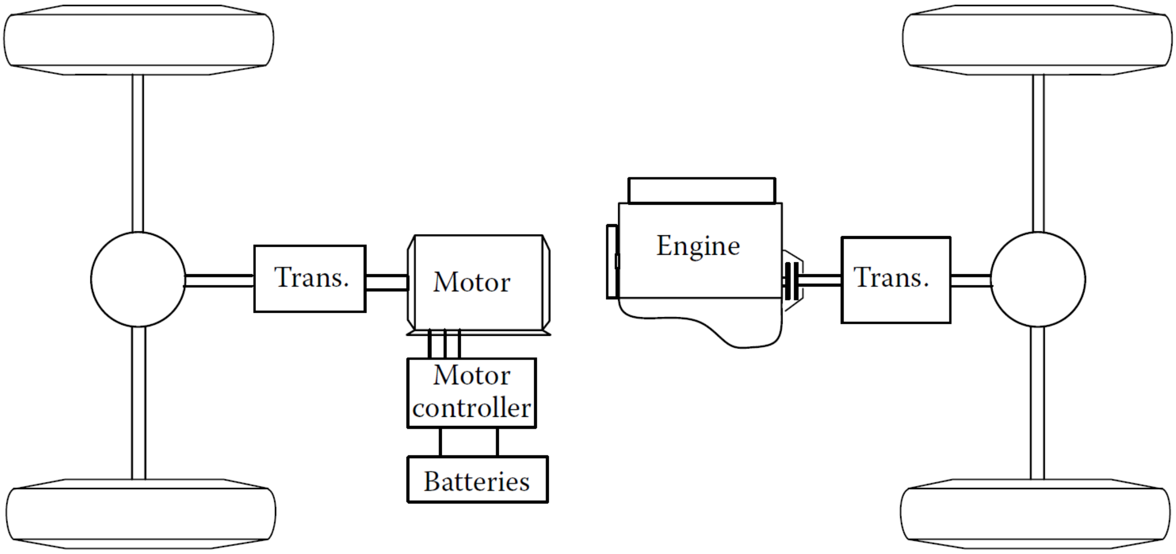

**Figure 1-1:** Driveline considered in this work: a parallel hybrid powertrain where the engine propels the front wheels and the motor propels the rear wheels [2]

control law, based on Lyapunov theory. Both terms in the control law are velocity dependent, since the wheel slip dynamics are scaled by the velocity of the vehicle (see equation 2-14).

The desired braking torque calculated by the wheel slip controller is distributed over both actuators by a control allocator. The allocation is based on the frequency content of the torque signal and the constraints on the actuators. A numerically efficient algorithm is developed to make actual implementation of the algorithm possible.

The results in this paper seem very promising, but some critical remarks can be made.

Where [5] explores the possibilities of the next generation vehicles with in-wheel motors, we choose a more realistic approach in this work based on vehicles currently commercially available. Nowadays the (hybrid) electric vehicles on the market have no in-wheel motors driving separate wheels, but usually one motor driving an entire axle. This means that the allocation of the braking torques can no longer be done for separate wheels, but should be done for an entire axle. Also, the motor is no longer directly coupled to a wheel, but a driveline is used to deliver the motor torque to the wheels, resulting in different actuator dynamics. To the best of the author's knowledge, little to no publications exist considering the hybrid ABS problem for vehicles with these types of driveline.

Also, in [5] the imprecise nature of the HAB is not taken into consideration. Due to varying parameters like braking pressure, velocity and temperature the friction coefficient between the braking pads and braking discs varies, resulting in an output uncertainty in the hydraulic braking torque. This uncertainty is likely to have a significant influence on the online estimation of the tire forces. In this work we do consider the friction coefficient uncertainty within the HAB and investigate its influence on the braking performance. Again, the author found little to no publications on the topic of hybrid ABS considering this phenomenon.

The braking maneuvers in [5] are performed within a limited velocity range (ca. $60\,[\mathrm{km/h}] \rightarrow 40\,[\mathrm{km/h}]$). In this work we will perform braking maneuvers from $100\,[\mathrm{km/h}] \rightarrow 15\,[\mathrm{km/h}]$.

Especially the lower velocity for which the controller is evaluated puts a strain on the controller, since for low velocities the slip dynamics become very fast. To cope with the lower velocities and slower actuators, the estimation law proposed in [5] needs to be improved.

Like in [5] we limit our scope to straight-line braking on a symmetric road. Also, it is assumed that the engine is fully decoupled from the front wheels while braking and thus engine braking is neglected.

## 1-4 Outline of the Thesis

In chapter 2 the dynamic models of the vehicle and its actuators are introduced and explained. These models are used for either design, simulation or both. Chapter 3 treats the topic of ABS. A detailed explanation of the robust adaptive slip controller used in this work is given, including the improved update law for the longitudinal tire force estimation. The control allocation problem is presented in chapter 4, where we introduce a numerically efficient method to distribute the required braking torque over the different actuators. In chapter 5 we discuss the results and the conclusions and recommendations can be found in chapter 6.

# Chapter 2

# Modeling

In chapter 1 we briefly introduced the vehicle model considered in this work. The vehicle has an internal combustion engine (ICE) driving the front wheels and an electric motor driving the rear wheels via a driveline, see figure 2-1. Since we only consider braking with a decoupled engine, no model of the ICE is required.

In section 2-1 we describe how braking torques influence the vehicle's dynamic behavior. First of all a model of the tire-road contact forces is presented, known as the static Burckhardt model. Next the quarter car model (QCM) is introduced, which describes the behavior of a single wheel attached to a quarter of the mass of the car. Both models are used for controller design and analysis purposes only.

During braking maneuvers, the electric motor can exert a certain braking torque on both rear wheels simultaneously while the four Hydraulic Actuated Brakes (HAB's) can exert braking torques on each wheel individually (see figure 2-1). Models of both actuators are presented in section 2-2. These models are used both for simulation purposes as well as selecting the weights of the control allocator (chapter 4).

For the simulation of braking maneuvers, a combination of CarSim [9] and Matlab/Simulink is used. CarSim is a commercially available simulation environment which accurately and efficiently simulates the performance of a vehicle's dynamics. The actuator models, slip controller and control allocator are modeled in Matlab/Simulink, the rest of the vehicle's models are provided by the CarSim simulation environment.

## 2-1 Braking Dynamics

### 2-1-1 Tire-road Contact Forces

The tire is the part of the vehicle that transfers the vertical load $F_z$ to the ground, where it is decomposed in the longitudinal friction force $F_x$ and lateral friction force $F_y$. $F_x$ is the force accelerating or decelerating the vehicle, while $F_y$ ensures steerability of the vehicle.

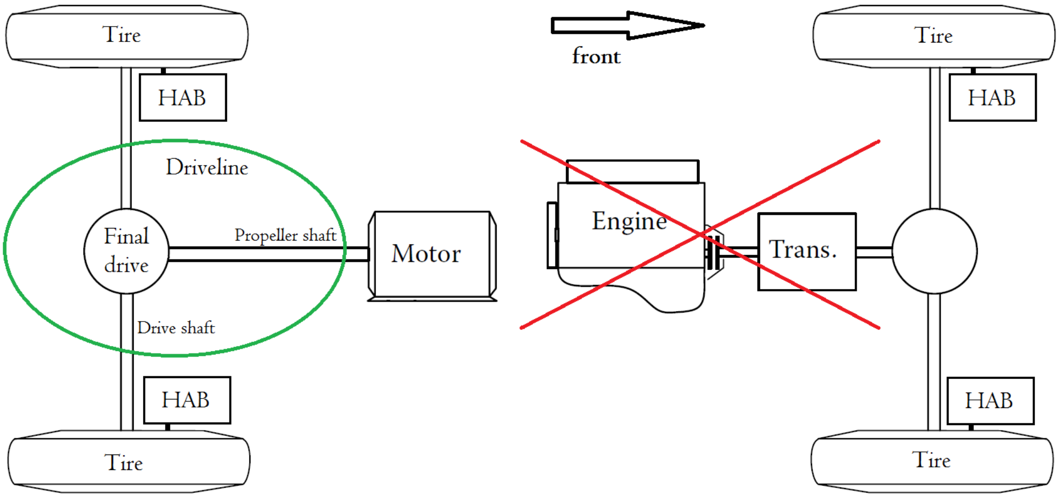

**Figure 2-1:** Vehicle configuration investigated in this work (based on [2]). The engine and transmission are decoupled during braking and thus neglected.

Both $F_x$ and $F_y$ depend on a large number of parameters describing the road, suspension and tire properties and can be described as:

$$F_x = F_x(F_z, \alpha_t, \gamma, \lambda) \tag{2-1}$$

$$F_y = F_y(F_z, \alpha_t, \gamma, \lambda), \tag{2-2}$$

where

- $F_z$ is the vertical load on the tire.
- $\alpha_t$ is the tire side slip angle; the angle between the longitudinal tire axis and the velocity vector (see figure 2-2).
- $\gamma$ is the camber angle; the tire inclination with respect to the vertical axis.
- $\lambda$ is the longitudinal tire slip defined as $\lambda = \frac{v - \omega r \cos(\alpha_t)}{\max(v, \omega r \cos(\alpha_t))}$, where $v$ is the vehicle ground speed, $r$ is the tire radius and $\omega$ is the rotational velocity of the wheel.

In general, the relation between the friction forces $F_x, F_y$ and the vertical load $F_z$ can be described as a linear one:

$$F_x = F_z \mu_x(\alpha_t, \gamma, \lambda) \tag{2-3}$$

$$F_y = F_z \mu_y(\alpha_t, \gamma, \lambda) \tag{2-4}$$

$$\mu_x := \frac{F_x}{F_z}$$

$$\mu_y := \frac{F_y}{F_z}$$

For very high values of $F_z$, the tire saturates and equations (2-3) and(2-4) are no longer accurate. However, for controller design equations (2-3) and (2-4) will suffice.

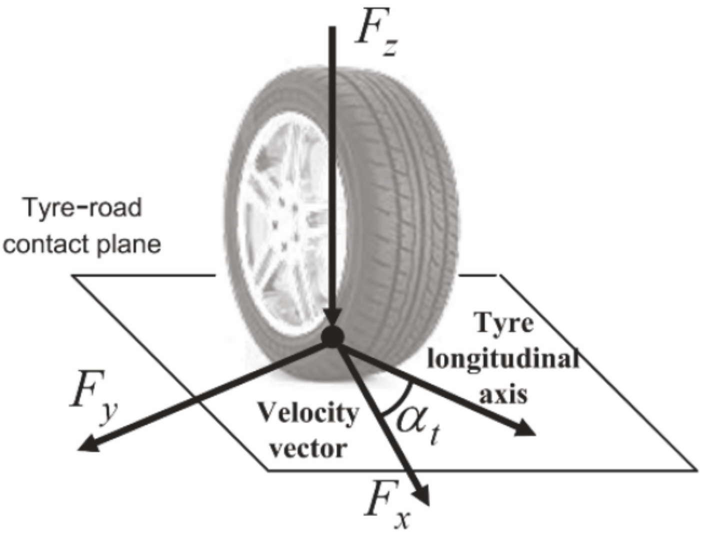

**Figure 2-2:** Tire forces [10]

In this work we consider straight line braking maneuvers. This means that the side slip angle will be small ($\alpha_t \approx 0 \rightarrow \cos(\alpha_t) \approx 1$) and the vehicle ground speed is larger than or equal to the linear wheel velocity ($v \geq \omega r$). This results in the following definition of the longitudinal slip $\lambda$.

$$\lambda = \frac{v - \omega r}{v}, \quad \lambda \in [0, 1] \tag{2-5}$$

Also, in the rest of this work when referring to the longitudinal friction coefficient $\mu_x(\lambda)$ we will omit the subscript and write $\mu(\lambda)$.

### Friction Models

In the literature many friction models, both static and dynamic, can be found describing the tire-road contact forces. In [11] a first principal based dynamic model called the "distributed LuGre model" describes the tire-road friction through a contact patch consisting of bristles. In [12] a semi-empirical model called the "Magic Formula" is described, which is often used in commercial simulation software. This model depends on numerous parameters which differ per tire. Both models are very useful for simulation purposes, but might be too complicated for controller synthesis.

**Static Burckhardt Model** In ([10],[13]) the (empirical) static Burckhardt model is proposed since it is both suitable for analytical purposes and accurate in describing the friction coefficient $\mu(\lambda)$. The model is given by:

$$\mu(\lambda, \boldsymbol{v}_r) = v_{r1}(1 - e^{-\lambda v_{r2}}) - \lambda v_{r3}, \tag{2-6}$$

where the parameters $\boldsymbol{v}_r$ depend on the road conditions and are in reality a function of time and location. In figure 2-3 the friction coefficient $\mu(\lambda)$ is plotted for several standard road conditions. The values of $\boldsymbol{v}_r$ used for this figure can be found in table A-1.

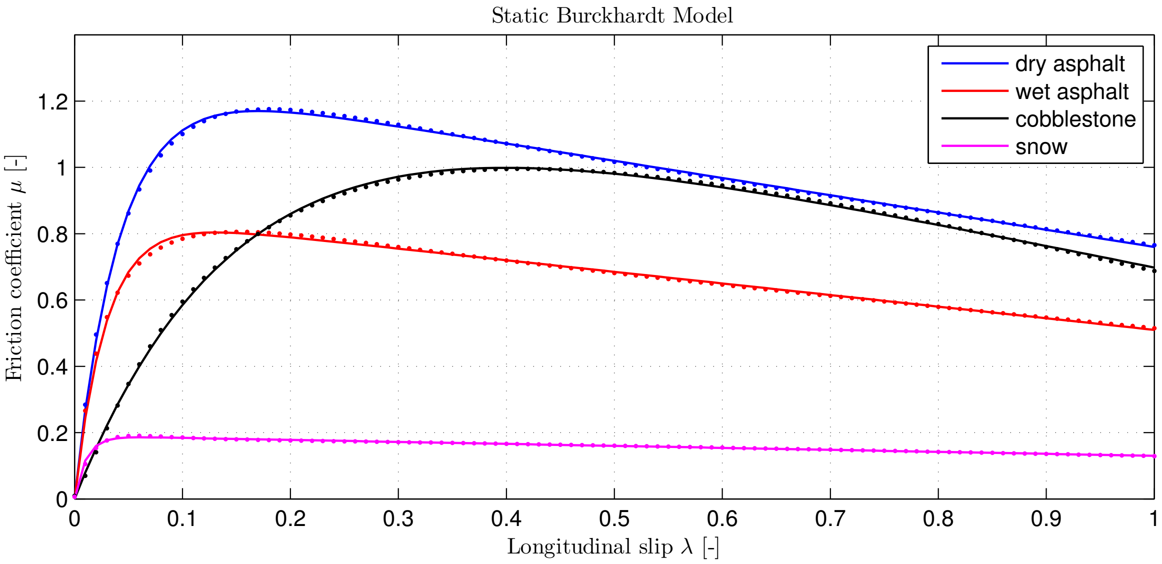

**Figure 2-3:** Static Burckhardt model (solid line) and its linear parameterisation (dotted line)

Due to the nonlinear term $e^{-\lambda v_{r2}}$ in equation (2-6), online identification of the model parameters is quite challenging. By approximating (2-6) with a linear parameterisation we can alleviate this problem [14]. The unknown parameters of the new nonlinear model can then be identified by linear techniques.

Consider the nonlinear term of the Burckhardt model $f(\lambda, v_{r2}) = e^{-v_{r2}\lambda}$ which defines the following mapping:

$$f : \mathcal{S} \times \mathcal{P} \to \mathbb{R} \tag{2-7}$$

where $(\lambda, v_{r2}) \in \mathcal{S} \times \mathcal{P} \subset [0, 1] \times \mathbb{R}$. To approximate this nonlinear term we consider the following parameterisation:

$$\hat{f}(\lambda, \boldsymbol{\beta}, \boldsymbol{\tau}) = [\tau_1 \dots \tau_n] \left[\hat{h}_1(\lambda, \boldsymbol{\beta}) \dots \hat{h}_n(\lambda, \boldsymbol{\beta})\right]^T = \boldsymbol{\tau}^T \hat{\boldsymbol{h}}(\lambda, \boldsymbol{\beta}) \tag{2-8}$$

where $\{\boldsymbol{\beta}, \boldsymbol{\tau}\} \in \mathbb{R}^m \times \mathbb{R}^n$ are vectors of parameters and $\hat{h}_i(\lambda, \boldsymbol{\beta})$, $i = 1, \dots, n$ are basis functions.

The problem of finding the optimal linear parameterisation can now be defined as finding the vector $\boldsymbol{\beta}^*$ which minimizes the modeling error $\epsilon(\boldsymbol{\beta})$ between $f(\lambda, v_{r2})$ and $\hat{f}(\lambda, \boldsymbol{\beta}, \boldsymbol{\tau})$ over a domain of interest $[\underline{\lambda}, \overline{\lambda}] \times \mathcal{D} \subset \mathcal{S} \times \mathcal{P}$:

$$\boldsymbol{\beta}^* = \arg\min_{\boldsymbol{\beta} \in \mathbb{R}^m} \epsilon(\boldsymbol{\beta}) = \arg\min_{\boldsymbol{\beta} \in \mathbb{R}^m} \left( \int_{v_{r2} \in \mathcal{D}} \left( \min_{\boldsymbol{\tau} \in \mathbb{R}^n} \int_{\underline{\lambda}}^{\overline{\lambda}} \left( f(\lambda, v_{r2}) - \boldsymbol{\tau}^T \hat{\boldsymbol{h}}(\lambda, \boldsymbol{\beta}) \right)^T d\lambda \right) \right) \tag{2-9}$$

To keep this problem tractable, we assume to know the type and the number $n$ of basis functions beforehand. Once a solution is obtained, we can compare it to solutions for other values of $n$ and other types of basis functions. This comparison was performed in [14], from which we obtained the information in table 2-1.

As we can see in table 2-1 the exponential basis functions are the best choice. For $n = 4$ the fitting error is smaller than for $n = 3$, but the fitting error for $n = 3$ provides a good enough

**Table 2-1:** Fitting error $\epsilon^*$ for different linear parameterisations

| type of basis function | $n = 1$ | $n = 2$ | $n = 3$ | $n = 4$ |
|---|---|---|---|---|
| polynomial | - | 0.6844 | 0.3857 | 0.2127 |
| logistic sigmoid | 0.2849 | 0.0467 | 0.2012 | 0.0059 |
| exponential | 0.2870 | 0.0362 | 0.0046 | 0.0005 |

fitting of the original nonlinear term and it decreases the number of parameters which need to be estimated online.

For the case of three exponential basis functions we find in [14] that

$$\boldsymbol{\beta}^* = [-4.99 \quad -18.43 \quad -65.62]^T$$

This yields the following linear parameterisation of $f(\lambda, v_{r2})$:

$$\hat{f}(\lambda, \boldsymbol{\tau}) = [\tau_1 \quad \tau_2 \quad \tau_3] \left[e^{-4.99\lambda} \quad e^{-18.43} \quad e^{-65.62}\right]^T \tag{2-10}$$

Replacing $f(\lambda, v_{r2})$ in (2-6) by $\hat{f}(\lambda, \boldsymbol{\tau})$ we arrive at the following linear parameterisation of the burckhardt model:

$$\hat{\mu}(\lambda, \boldsymbol{p}) = \boldsymbol{p}^T \boldsymbol{\phi}(\lambda) = \boldsymbol{p}^T \left[1 \quad \lambda \quad e^{-4.99\lambda} \quad e^{-18.43\lambda} \quad e^{-65.62\lambda}\right]^T \tag{2-11}$$

In figure 2-3 the linear parameterisation of the Burckhardt model described in (2-11) is compared to the nonlinear Burckhardt model described in (2-6).

### 2-1-2 Quarter Car Model

The QCM is one of the most simple and elemental braking models available and describes the behavior of a single wheel attached to a quarter of the mass of the vehicle. By assuming a constant normal load we neglect suspension dynamics and load transfer phenomena [10]. The QCM is a popular choice for designing and analyzing braking control algorithms, see for example ([5], [7], [15], [16]).

The QCM is given by:

$$\dot{\omega} = \frac{1}{J}(rF_x - T_b) \tag{2-12}$$

$$\dot{v} = -\frac{F_x}{m}, \tag{2-13}$$

where the variables and parameters are displayed in figure 2-4 and defined as:

- $\omega$ [rad/s] is the rotational velocity of the wheel
- $v$ [m/s] is the vehicle ground velocity
- $J$ [kg m$^2$] is the wheel inertia

- $m$ [kg] is a quarter of the vehicle weight
- $r$ [m] is the wheel radius
- $T_b$ [Nm] is the braking torque
- $F_x$ [N] is the longitudinal tire force

For slip control, it is beneficial to rewrite (2-12) as:

$$\dot{\lambda} = -\frac{r}{Jv}\left(\Psi(\lambda) - T_b\right) \tag{2-14}$$

where

$$\Psi(\lambda) = \left(r + \frac{J}{rm}(1-\lambda)\right) F_z \mu(\lambda) \tag{2-15}$$

As we can see in equation (2-14), the wheel slip dynamics are scaled by the reciprocal of the velocity of the vehicle. For $v \to 0$, the slip dynamics become infinitely fast. This is an issue that needs to be addressed when designing the slip controller.

When we take a closer look at equation (2-15), we find that since $rm \gg J$ we have that $\Psi(\lambda) \simeq rF_z\mu(\lambda)$. This means that in practice the wheel slip corresponding to the maximum of the friction coefficient $\mu(\lambda)$ is the same as the wheel slip corresponding to the maximum of $\Psi(\lambda)$.

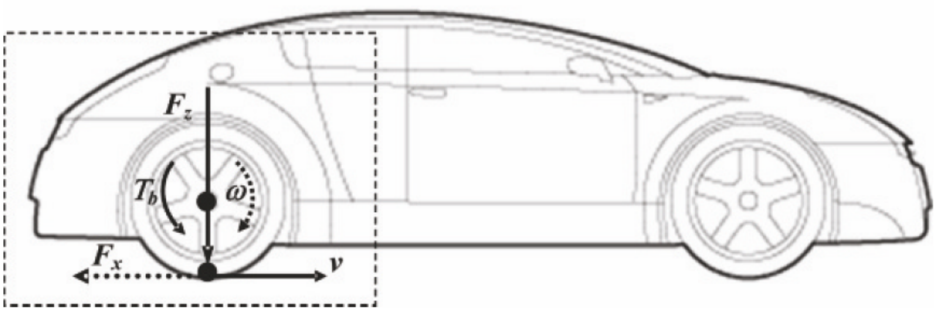

**Figure 2-4:** Quarter car model [10]

### Equilibria

A possible equilibrium of the QCM is $\dot{\omega} = 0$, $\dot{v} = 0$. This equilibrium corresponds to the case of constant velocity and is not of interest for braking maneuvers. The equilibria of interest are characterized by $\dot{\lambda} = 0$. This means that the slip and normalized wheel deceleration are constant: $\lambda = \overline{\lambda}$ and $\eta = \overline{\eta}$, where $\eta$ is defined as:

$$\eta = -\frac{r\dot{\omega}}{g} \tag{2-16}$$

Substituting $\dot{\lambda} = 0$ into (2-14) give us the following equilibria:

$$\overline{T}_b = \Psi(\overline{\lambda}) = \left(r + \frac{J}{rm}(1-\overline{\lambda})\right) F_z \mu(\overline{\lambda}) \tag{2-17}$$

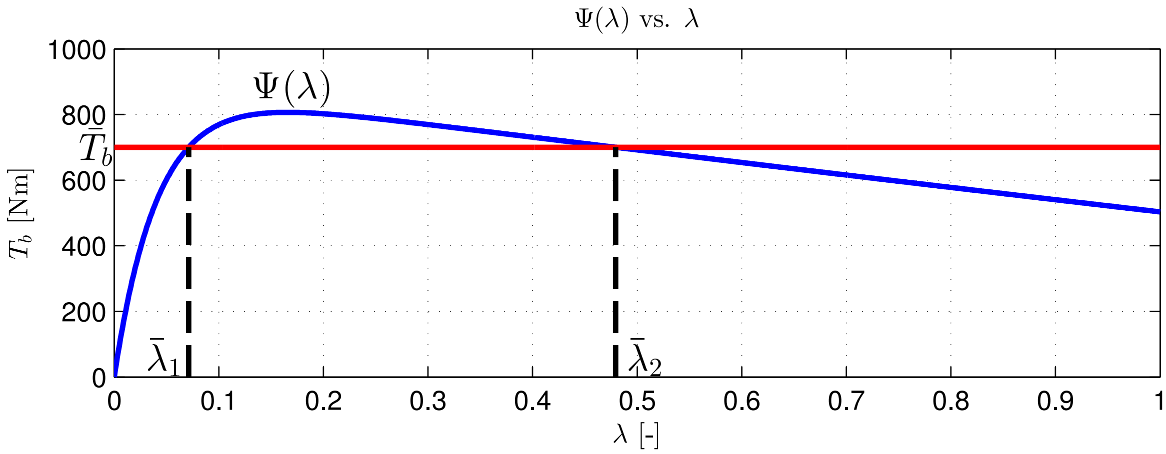

**(a)** Equilibrium points in the $(\lambda, T_b)$-plane

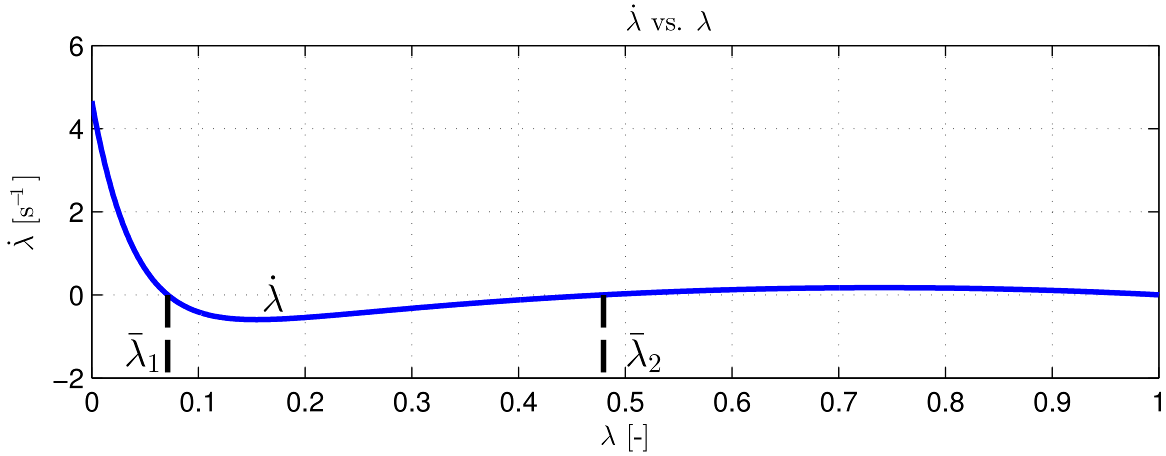

**(b)** Equilibrium points in the phase-plane

**Figure 2-5:** Equilibria analysis of the QCM (1)

In figure 2-5 the equilibria are shown both in the $(\lambda, T_b)$-plane and the $(\lambda, \dot{\lambda})$ phase-plane. For this particular case we used $\overline{T}_b = 700\,[\text{Nm}]$, $\omega = 150\,[\text{rad/s}]$ and the dry asphalt parameters from table A-1. As can be seen in figure 2-5a we can have either

- no equilibrium points when $\overline{T}_b > \max_\lambda \Psi(\lambda)$,
- 1 equilibrium point when we have $\overline{T}_b = \max_\lambda \Psi(\lambda)$ (which in practice never occurs) or
- 2 equilibrium points when $\overline{T}_b < \max_\lambda \Psi(\lambda)$

Figure 2-5b shows that the equilibrium at $\overline{\lambda}_1$ is locally asymptotically stable while the second equilibrium at $\overline{\lambda}_2$ is unstable. This confirms the fact that equilibria at the left of the friction peak are stable, while equilibria at the right of the friction peak are unstable. In [10] this is shown by applying Lyapunov's linearisation method to obtain linear models and performing an analysis of the pole location as a function of $\overline{\lambda}$.

Instead of expressing the equilibria in the $(\lambda, T_b)$-plane, it is also interesting to express them in the $(\lambda, \eta)$-plane. Recalling the definition of the wheel slip (equation (2-5)), setting its derivative equal to zero and rearranging it yields:

$$\dot{\omega} = \omega \frac{\dot{v}}{v} = \frac{1 - \overline{\lambda}}{r} \dot{v} \tag{2-18}$$

Replacing $\dot{v}$ by (2-13) and plugging the results in equation (2-16) yields the steady-state relationship between $\eta$ and $\lambda$:

$$\overline{\eta}(\overline{\lambda}) = \Xi(\overline{\lambda}) = \frac{F_z}{mg}(1 - \overline{\lambda})\mu(\overline{\lambda}) \tag{2-19}$$

Similar to the case of the $(\lambda, T_b)$-plane, we find that we have either $1\,, 2$ or 3 equilibria depending on the choice of $\overline{\eta}$. In figure 2-6a the equilibrium manifold $\Xi(\lambda)$ is displayed, along with the equilibria at $\overline{\lambda}_1$ and $\overline{\lambda}_2$ for $\overline{\eta} = 0.7$, $\omega = 150\,[\text{rad/s}]$ and dry asphalt conditions. To investigate the stability of the equilibria we use again the $(\lambda, \dot{\lambda})$ phase-plane. By plugging in the definition of the normalized deceleration $\eta$ (2-16) into (2-12), we have the following result:

$$\eta = \frac{r}{Jg}\left(T_b - rF_z\mu(\lambda)\right) \tag{2-20}$$

Substituting (2-19) and (2-20) into the wheel slip dynamics (2-14) yields:

$$\dot{\lambda} = -g\frac{1 - \lambda}{r\omega}\left(\Xi(\lambda) - \eta\right) \tag{2-21}$$

The phase-plane is displayed in figure 2-6b, were we find that the equilibrium at $\overline{\lambda}_1$ is locally asymptotically stable, while the equilibrium at $\overline{\lambda}_2$ is unstable.

In chapter 3 we will use this representation of the equilibria in the $(\lambda, \eta)$-plane to discuss the merits and disadvantages of wheel deceleration control.

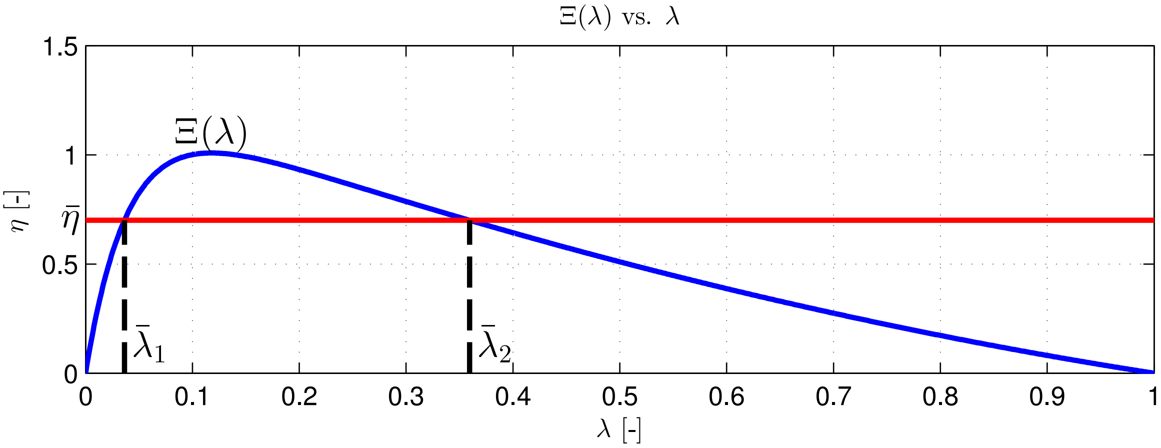

**(a)** Equilibrium points in the $(\lambda, \eta)$-plane

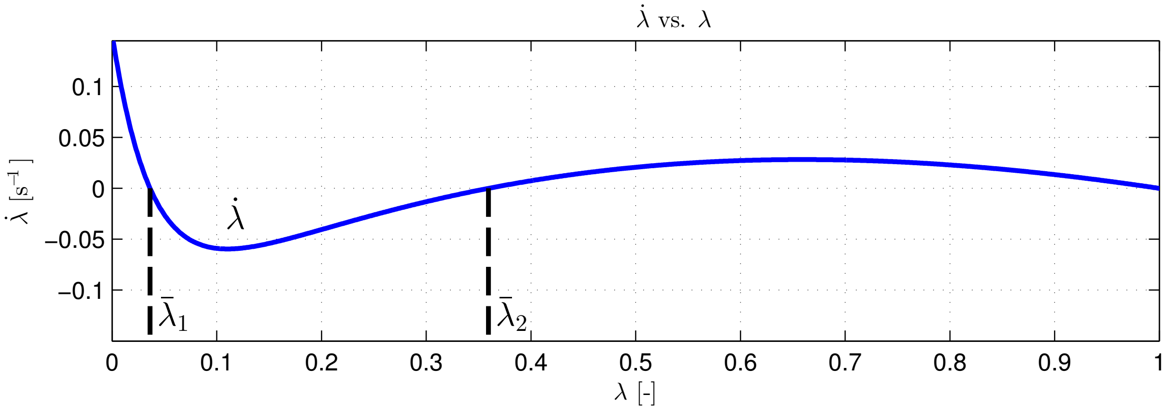

**(b)** Equilibrium points in the phase-plane

**Figure 2-6:** Equilibria analysis of the QCM (2)

## 2-2 Actuator Dynamics

In this work we consider two different brake actuators: an electric motor and a HAB. Both front and rear wheels are equipped with exactly the same HAB.

### 2-2-1 Hydraulic Actuated Brake Model

The relation between the braking torque $T_h$ generated by the HAB and the braking pressure $p_b$ is given by [10]:

$$T_h = r_d \nu A p_b \tag{2-22}$$

where $r_d$ is the brake disc radius, $\nu$ is the friction coefficient between the brake pad and brake disc and $A$ is the brake piston area. In literature (for example [10]) the friction coefficient $\nu$ is often assumed to be constant, but in reality it varies depending on different variables like the braking pressure, velocity, temperature and the wear of the pad. When $\nu$ is assumed to be a known constant, controlling the braking torque $T_h$ is equivalent to controlling the braking pressure $p_b$.

First principal models of a HAB can be found in literature (see for example [17], [18] or [19]). Although these models can be very accurate, their complexity makes it hard to use them for controller synthesis. For simulation purposes these models can be quite useful though.

A HAB consists of several components: a master cylinder, brake cylinders, a main chamber, a hydraulic ABS unit and pipelines connecting the aforementioned parts. The hydraulic ABS unit consists of an accumulator, a pump, valves and pipelines (see figure 2-7).

When the driver applies force to the brake lever, pressure is build up in the master cylinder resulting in pressure build-up in the brake cylinders. The brake cylinders press the brake pads against the brake discs creating a braking moment. When the Anti-lock Braking System (ABS) is active, the system transforms from an open loop into a closed loop system and the braking pressure is controlled by the hydraulic ABS unit via pulse width modulation of the build and dump valves [18].

For the purpose of controller design, the closed loop HAB can be approximated by a first order time delayed transfer function between the desired and the actual hydraulic braking torque [5]:

$$G_h(s) = \frac{e^{-0.015}}{0.016s + 1} \tag{2-23}$$

The range and rate limits are $T_{h,\max} = 2\,[\mathrm{kN}]$ and $\dot{T}_{h,\max} = 10\,[\mathrm{kN/s}]$.

#### Friction Coefficient Uncertainty

The model presented in (2-23) captures the braking pressure dynamics of the HAB well, but fails to capture the imprecise nature of the braking torque $T_h$ due to the unknown friction coefficient $\nu$. Little information can be found in literature on the precise nature of this uncertainty. However, in [20] a small scale friction tester was used to investigate the effect of metal fibers on the friction performance of automotive brake friction materials. Experiments were performed for six different combinations of brake disc and pad materials. During these

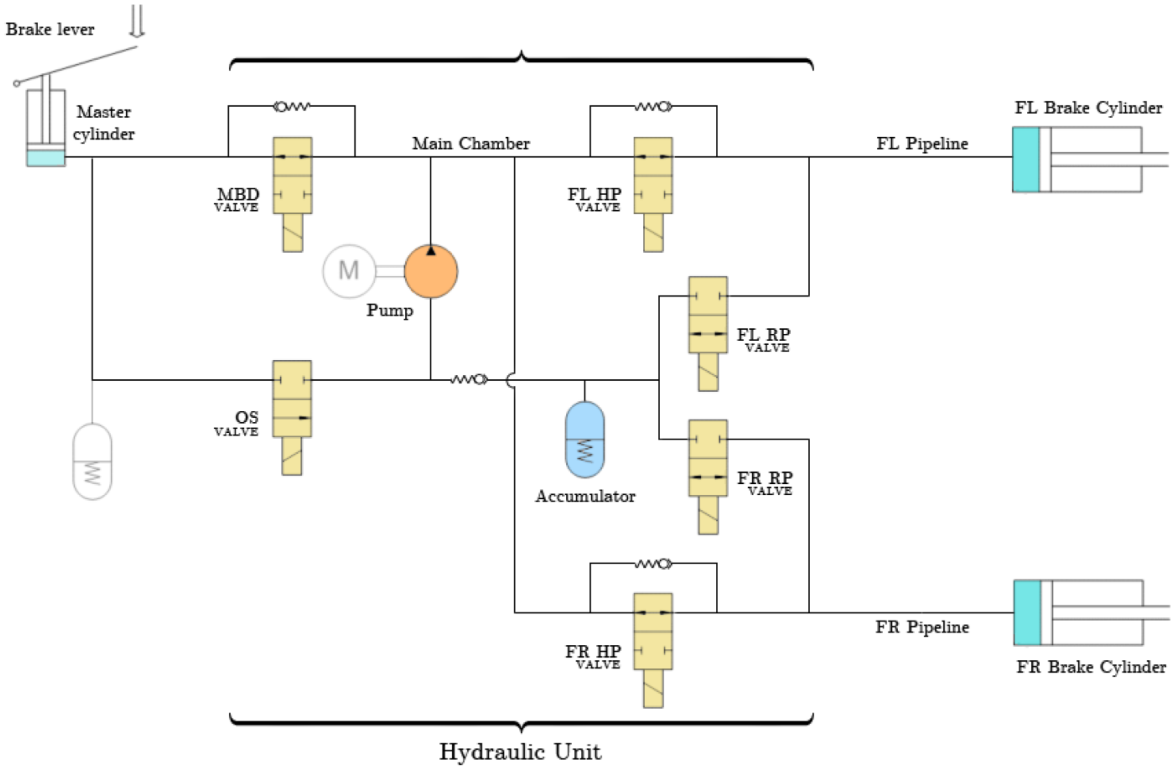

**Figure 2-7:** Overview of hydraulic braking circuit of the front wheels [17]

experiments the influences of sliding velocity, braking pressure and temperature on the friction coefficient $\nu$ were investigated.

To model the friction coefficient uncertainty, we used the results obtained for the combination of the grey cast iron brake disc and brake pads with copper fibers, see figure 2-8. This combination is one that resembles the combination actually used in commercial brake systems [20].

One of the difficulties of designing a model based on these results lies in the difference between the narrow ranges used in the experiments and the broad ranges encountered during driving conditions. To obtain a model, we need to extrapolate the results published in [20], while we do not fully understand the underlying phenomena [20]. Since the amount of information we need to base our model on is so limited, we only try to capture the main effects in a very crude model. These effects can be described as: $\nu$ remains approximately the same for all temperatures, $\nu$ decreases for increasing velocity $v$ and $\nu$ increases for increasing braking pressure $p_b$.

We assume that the nominal friction coefficient $\nu^*$ is defined in the middle of the ranges of interest of both the velocity and desired braking torque (and thus braking pressure). The middle of these ranges is defined as $v^* = 50\,[\text{km/h}]$ and $T^* = 600\,[\text{Nm}]$ (maximum torque exerted on a wet asphalt road is approximately $1200\,[\text{Nm}]$). Also we assume that the uncertainty in $\nu$ can be described as the sum of two affine functions of both $v$ and $T$, where at the limits of the velocity and braking torque ranges the value of $\nu$ deviates respectively $\Delta_{T_{\bar{v}}}$ [%]

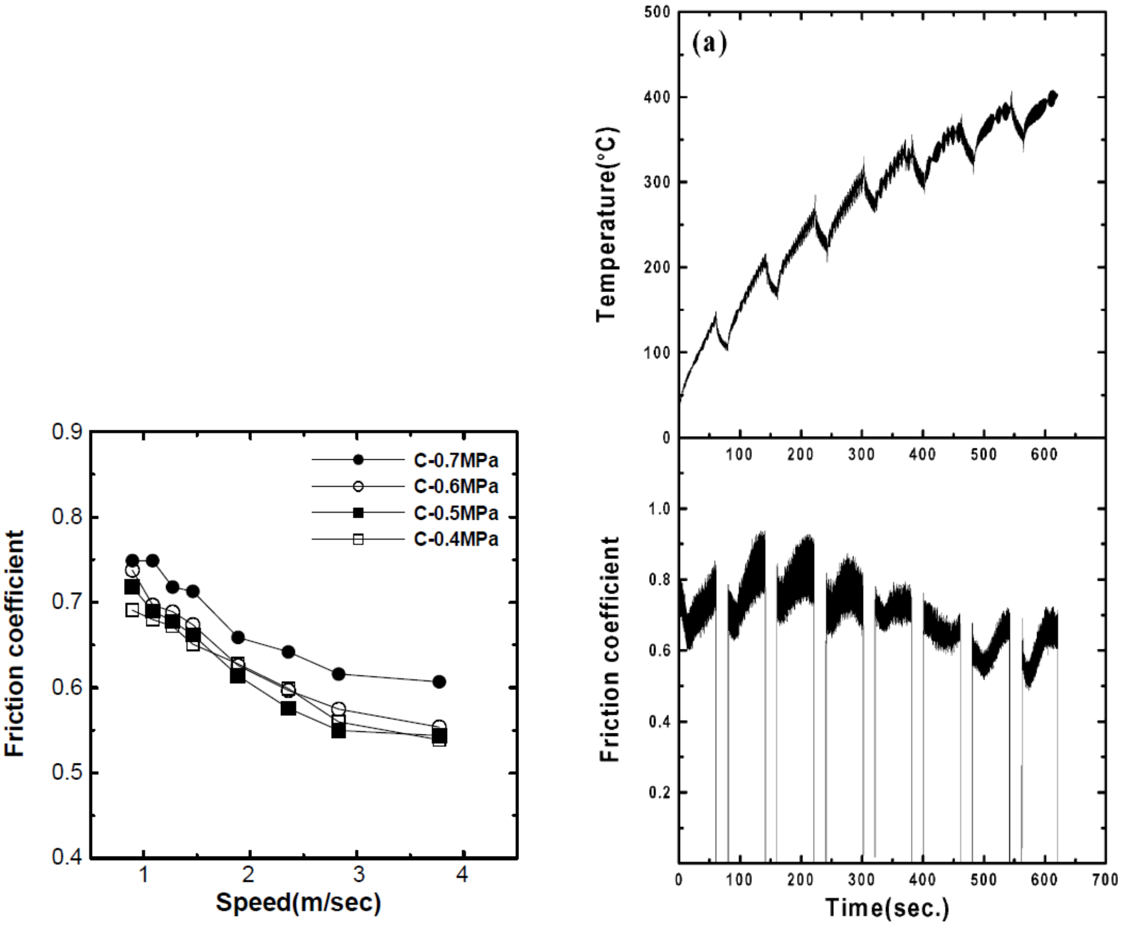

**(a)** The coefficient of friction as a function of sliding speed and applied pressure

**(b)** Disk temperature and friction coefficient measured during constant interval tests

**Figure 2-8:** Experimental results from [20], using a grey cast iron disc and braking pads with copper fibers and $\Delta_{T_{\bar{T}}}$ [%] from its nominal value $\nu^*$:

$$\begin{aligned} T_h &= (1 + \Delta_T)\,\hat{T}_h \\ \Delta_T &= \left( (\hat{T}_h - T^*)\frac{\Delta_{T_{\bar{T}}}}{T^*} - (v - v^*)\frac{\Delta_{T_{\bar{v}}}}{v^*} \right)/100, \end{aligned} \tag{2-24}$$

where $\hat{T}_h$ is the torque obtained using equation (2-23) and $T_h$ is the braking torque actually exerted by the hydraulic brakes.

In figure 2-8a we see that the pressure range used in the experiments is 40 [bar] to 70 [bar], which is a bit narrow range of the braking pressures during driving conditions (usually between 0 [bar] and approximately 160 [bar] [21]). When we compare $\nu$ at various velocities for the braking pressures $p_b = 40$ [bar] and $p_b = 70$ [bar], we find that for $p_b = 70$ [bar] $\nu \approx 10\%$ higher than for $p_b = 40$ [bar]. Therefore $\Delta_{T_{\bar{T}}} = 10$ [%] is deemed to be a reasonable value.

The sliding velocity range of the experiment is very small starting at 0.9 [m/s] to 3.8 [m/s], which corresponds to a driving velocity range of 6.5 [km/h] to 27.4 [km/h] when we assume a brake disc diameter of 0.15 [m] and a wheel diameter of 0.3 [m]. Since we consider braking maneuvers from 100 [km/h] → 15 [km/h], the need to extrapolate the results is obvious. However, the way in which to extrapolate is all but clear. With a little imagination the trend in the data can be interpreted as being linear or approaching an asymptote from above. In the speed range used in the experiment, the friction coefficient decreased approximately 20 [%] for $p_b = 40$ [bar] and 17 [%] for $p_b = 70$ [bar]. To be conservative, $\Delta_{T_{\bar{v}}} = 10$ [%] seems a reasonable value.

In figure 2-8b we see that in the temperature range of 50° [C] to 400° [C] the friction coefficient remains more or less the same. Therefore, we neglect the influence of the temperature on the friction coefficient $\nu$.

Finally, the author would like to stress that the purpose of the uncertainty modeled in equation (2-24) is not to present an accurate and detailed model of the friction coefficient uncertainty within a hydraulic braking system, but to investigate how the slip controller and control allocator deal with the imprecise torque output of the HAB.

### 2-2-2 Electric Motor and Driveline Model

The second brake operator is the electric motor. The electric motor is connected to the rear wheels by a driveline. In [22] excellent first principal models of electric motors can be found, while [13] is often referred to for models of drivelines.

However, this work is part of a thesis project at the Integrated Safety department of TNO Automotive and they supplied a second order model of an electric motor coupled to a similar driveline. The model is given by:

$$G_m = \frac{1894}{s^2 + 22.96s + 1894} \tag{2-25}$$

The rate limit is $\dot{T}_{\text{m,max}} = 10$ [kN/s] and due to the effect of field weakening the maximum torque is given by:

$$T_{m,\max} = \begin{cases} \hat{T}_{m,\max} & \text{if } v \leq v_n \\ \hat{T}_{m,\max}\frac{v_n}{v} & \text{if } v > v_n \end{cases} \tag{2-26}$$

where $v$ is the velocity, $v_n = 50\,[\text{km/h}]$ is the velocity corresponding to the nominal speed of the motor and $\hat{T}_{m,\max} = 714.7\,[\text{Nm}]$ is the peak braking torque.

An advantage of the electric motor is that we can control its torque accurately. However, we added additional dynamics to the motor by coupling it to a driveline. When the motor is in a (more or less) steady state, the torque is known accurately. During transient phases, this is unfortunately no longer the case.

## 2-2-3 Actuator Comparison

In this section we will compare the performance of both actuators. In figure 2-9 the magnitude of the bode plots of both actuators are depicted. However we have to keep in mind that in the bode plot of the HAB we did not account for the output uncertainty due to the unknown friction coefficient $\nu$.

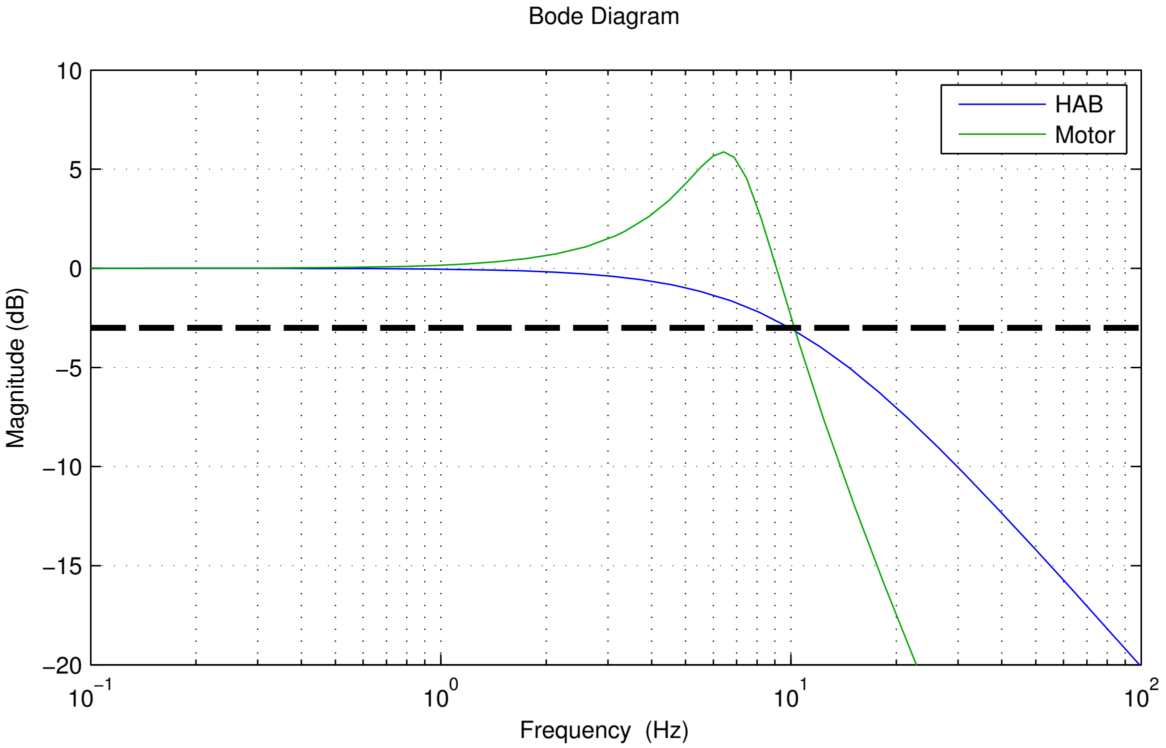

**Figure 2-9:** Bode diagrams of $G_h$ and $G_m$

In figure 2-9 we see that both actuators have approximately the same bandwidth (defined as the frequency where the bode diagram intersects the $-3\,[\text{dB}]$ line). However, the electric motor exhibits a resonance peak around $6.5\,[\text{Hz}]$ indicating amplification of the control signal around this frequency, while the gain of the HAB is close to $0\,[\text{dB}]$.

To highlight the different properties of the actuators, we performed open loop simulations of braking maneuvers of which the results are displayed in figure 2-10. For all braking maneuvers, we started the simulation with a velocity of $v = 100\,[\text{km/h}]$ and a constant braking torque on the front wheels of $T_b = 600\,[\text{Nm}]$.

In figure 2-10a we set the reference torque at 375 [Nm]. We see that the hydraulic torque exhibits no oscillations and is inaccurate. As time elapses and the velocity decreases, the friction coefficient $\nu$ increases resulting in an increase of the hydraulic braking torque. When we look at the electric motor torque, we see that torque oscillates in the beginning due to the step input and is not able to reach the reference value. This is due to the field weakening property, which limits the maximum torque for high velocities. As the velocity decreases, the maximum electric torque increases until the velocity passes the base speed of the motor, at which point we have reached the maximum torque the motor can exert. The motor torque is now at its constant maximum value.

In figure 2-10b we set the reference torque at a constant value of 125 [Nm]. Even at high velocity, this is well within the limits of the electric motor and aside from some significant overshoot in the first 0.5 [s] the motor torque tracks the reference torque very accurately. The hydraulic torque shows no overshoot or oscillations, but is also not capable of tracking the reference torque accurately.

In figure 2-10c we used a sinusoidal reference torque oscillating with an amplitude of 50 [Nm] and a frequency of 1 [Hz] around the DC value of 125 [Nm]. Like in figure 2-10b, we see that the electric motor is very well capable of tracking the reference torque, aside from the initial oscillations. The HAB is capable of tracking the oscillations in the reference, but it is inaccurate due to the unknown $\nu$. In figure 2-10e the time derivatives of the torque signals from figure 2-10c are displayed. The derivative of the motor torque is almost a perfect match to the time derivative of the reference signal, but also the time derivative of the hydraulic braking torque is quite accurate.

In figure 2-10d we increased the frequency of the sinusoidal reference to 6.5 [Hz]. The reference torque is amplified by the motor and driveline dynamics, resulting in a high amplitude sinusoidal torque. On the other hand, the hydraulic torque is an inaccurate, slightly attenuated copy of the reference torque. When we look at the time derivative of these signals in figure 2-10f we see that the time derivative of the hydraulic torque is much better in tracking the time derivative of the reference torque than the time derivative of the electric torque.

The conclusion from this open loop analysis is that the tracking performance of the electric motor is better than the tracking performance of the HAB when the frequency content of the reference signal is negligible at frequencies higher than 1 [Hz]. However, the amount of electric motor torque is limited, especially at velocities above the base speed of 50 [km/h]. The tracking performance of the HAB is superior to the tracking performance of the electric motor when a significant portion of the frequency content of the control signal is concentrated at frequencies above 1 [Hz].

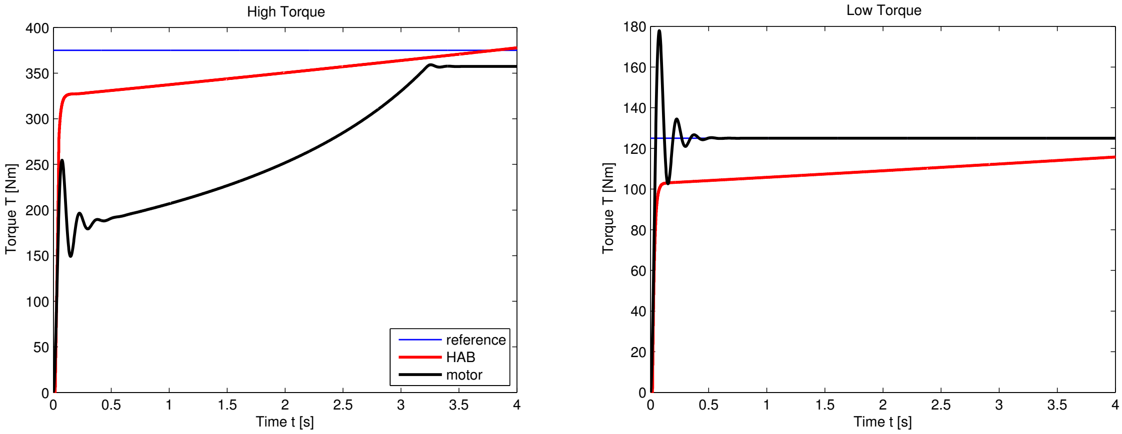

**(a)** Open loop response to a constant reference torque of $375\,[\mathrm{Nm}]$

**(b)** Open loop response to a constant reference torque of $125\,[\mathrm{Nm}]$

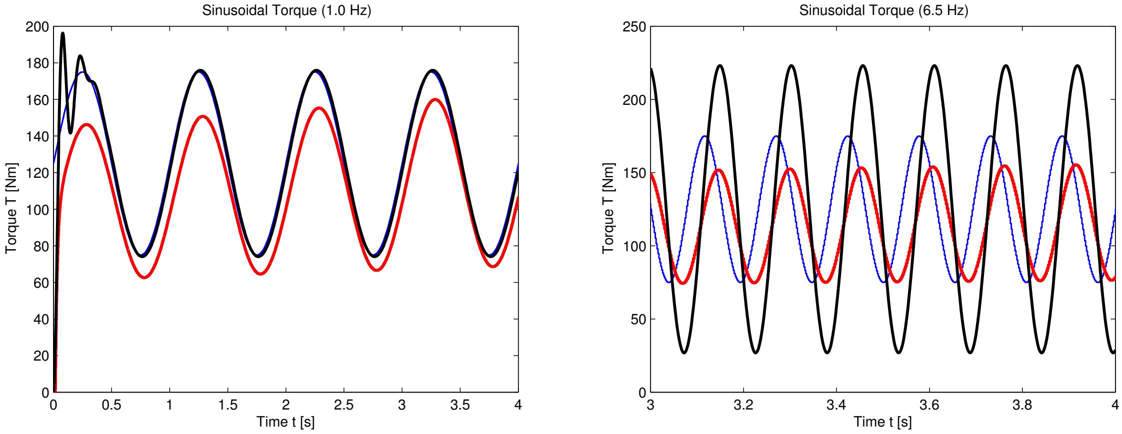

**(c)** Open loop response to a sinusoidal reference torque with an amplitude of $50\,[\mathrm{Nm}]$, a DC value of $125\,[\mathrm{Nm}]$ and a frequency of $1\,[\mathrm{Hz}]$

**(d)** Open loop response to a sinusoidal reference torque with an amplitude of $50\,[\mathrm{Nm}]$, a DC value of $125\,[\mathrm{Nm}]$ and a frequency of $6.5\,[\mathrm{Hz}]$

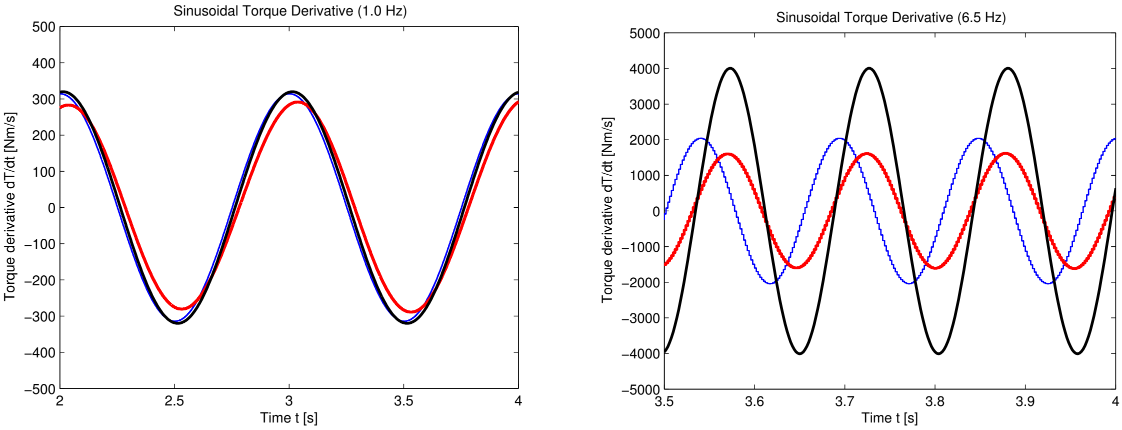

**(e)** Time derivatives of the signals in figure 2-10c

**(f)** Time derivatives of the signals in figure 2-10d

**Figure 2-10:** Open loop comparison of both actuators

# Chapter 3

# ABS Controller

In the past decades, many ABS algorithms have been investigated and developed. Important aspects to consider are the types of actuators and sensors one has at his disposal. In braking control, usually two output variables are considered for control: normalized wheel deceleration $\eta$ and wheel slip $\lambda$. To minimize the braking distance, one should try to control the brakes at the peaks of the tire-road friction coefficient $\mu(\lambda)$.

The first section treats wheel deceleration control, the second section treats wheel slip control and the final section offers some conclusions on the subject of braking control with respect to this work.

To highlight some fundamental differences between wheel deceleration and wheel slip control, figure 3-1 has been included. It shows both the wheel deceleration equilibrium manifold $\Xi(\lambda)$ and the friction coefficient $\mu(\lambda)$ for different road types (no load transfer is assumed: $\frac{F_z}{mg} = 1$). The equilibrium manifold $\Psi(\lambda)$ is not shown here since $J << mr$ and thus $\Psi(\lambda)$ practically corresponds to a scaling of the friction coefficient $\mu$ by a factor $rF_z$ (see section 2-1-2).

## 3-1 Wheel Deceleration Control

The traditional Anti-lock Braking System (ABS) is based on controlling the normalized wheel deceleration $\eta$. The prime motivator for this choice is the availability of cheap and reliable wheel deceleration sensors, whereas measuring wheel slip is complicated and sensitive to measurement noise.

In figure 3-1 it can be seen that there is no setpoint $\eta^*$ which results in reasonable behavior for every road surface. Depending on the road type and the $\eta^*$ chosen, there are either zero, one or two equilibrium points with corresponding values of $\lambda$. Also, the open loop dynamics are non-minimum phase for values of $\lambda$ beyond the peak of the friction curve. For these reasons, wheel deceleration has never been implemented as a classical regulation scheme.

Instead, most ABS algorithms consists of many heuristically tuned logic rules forming a rule base (see for example [13] and [23]). Though this technique has proven itself in the past

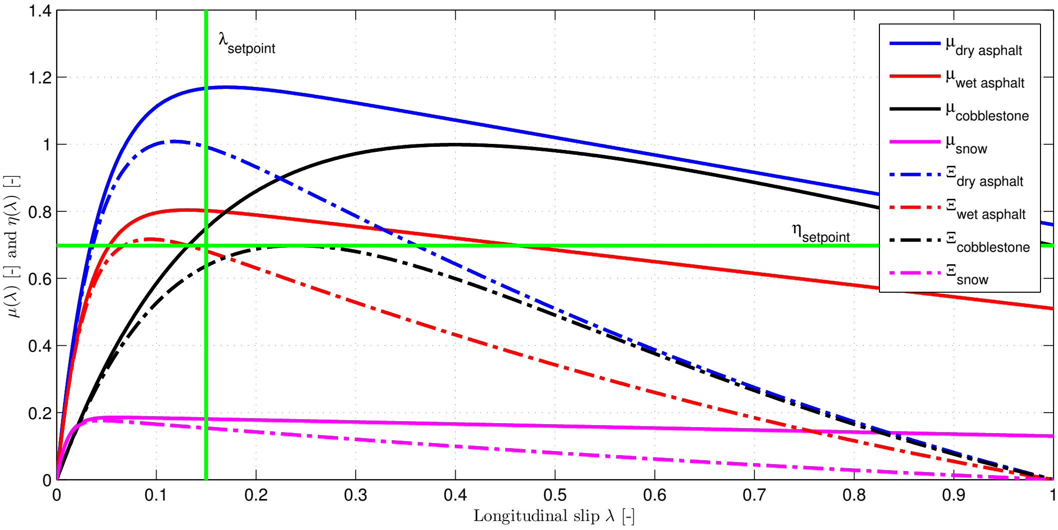

**Figure 3-1:** Friction coefficient $\mu(\lambda)$ and equilibrium manifold $\Xi(\lambda)$ for different road types

decades, it is difficult to fully understand how the observed performance is obtained by the heuristic rules. Also, there is no theory to determine and analyse the stability of the controller.

In [24] a 5-phase hybrid control algorithm is proposed where the switching logic depends on thresholds on the wheel deceleration. In each state the dynamics have a clear mathematical description and the stability of the limit cycle can be assessed. Since the wheel deceleration is both used as the controlled variable and to detect the peak of the friction curve, the performance is limited.

In [25] a 2-phase ABS algorithm is proposed where a force-sensing bearing is used to measure the longitudinal braking force of the tire. This variable is then used to determine the peak of the friction curve, making the 'hold pressure' phases in the 5-phase algorithm obsolete. This enables the limit cycle to become smaller, improving braking performance.

Although deceleration-based algorithms are robust with regard to sensor noise, their performance is never optimal. Instead of reaching the point of optimal friction, the algorithm circles around the peak. Another disadvantage is that for surfaces with a 'flat' friction curve, the peak is hard to distinguish and the wheel might end up being locked after all.

## 3-2 Wheel Slip Control

Wheel slip control has the benefit that the choice of set point is robust with respect to changes in road surface. There exists a setpoint $\lambda^*$ which might be a good compromise for every road surface, see figure 3-1. Also, for any choice of $\lambda^*$ the equilibrium will be unique, whereas for deceleration control there are either zero, one or two equilibria. The downside of slip control however is that measuring the slip is complicated and sensitive to measurement errors.

In [26] quite promising results were presented using a gain scheduling wheel slip controller. However, an important drawback is that for robustness it was necessary to make sure the slip setpoint is left from the friction peak. Also, the effort in tuning the controller for several velocities is considered to be a big disadvantage.

In [27] and [28] a second-order sliding-mode (SOSM) controller is proposed which has a fixed structure. The control law does not depend on the velocity and is configured to handle the worst possible conditions, resulting in a robust but conservative controller.

The robust adaptive slip controller presented in [5] is able to identify the road conditions online and adapts when these road conditions change. It treats the control and estimation problem in a unified approach. Also the control law is velocity dependent, which makes gain scheduling unnecessary. These advantages make the robust adaptive wheel slip controller the best candidate for the job.

### 3-2-1 Robust Adaptive Slip Control

In [5] the quarter car model (QCM) (equations (2-12) - (2-13)) is rewritten to include torque and force disturbances resulting from unmodelled dynamics:

$$\dot{\omega} = \frac{1}{J_w}\Big(rF_z\mu(\lambda) - T_b - \Delta_\omega(t,\omega)\Big) \tag{3-1}$$

$$\dot{v} = -\frac{1}{m}\Big(F_z\mu(\lambda) + \Delta_v(t,v)\Big), \tag{3-2}$$

where $(v,\omega) \in \mathcal{D} = (0,\infty) \times [0,\infty) \subset \mathbb{R}^2$. Both the torque disturbance $\Delta_\omega$ and force disturbance $\Delta_v$ are assumed to be uniformly bounded:

$$|\Delta_v(t,v)| \leq \overline{\Delta}_v, \quad |\Delta_\omega(t,\omega)| \leq \overline{\Delta}_\omega, \quad \forall (t,v,\omega) \in [0,\infty) \times \mathcal{D} \tag{3-3}$$

The slip dynamics are then given by:

$$\dot{\lambda} = -\frac{p_1}{v}\Big(\Psi(\lambda) - T_b - \Delta_\omega(t,\omega) + (1-\lambda)p_2 r \Delta_v(t,v)\Big) \tag{3-4}$$

where

$$p_1 = \frac{r}{J_w}, \quad p_2 = \frac{J}{mr^2}, \quad \Psi(\lambda) = \big(1 + (1-\lambda)p_2\big) r\mu(\lambda)F_z \tag{3-5}$$

Assuming perfect knowledge of $\Psi(\lambda)$ and negligible disturbances ($\Delta_v = \Delta_\omega = 0$), input-output linearisation can be used to obtain a control law that makes the wheel slip exponentially converge to the desired wheel slip $\lambda^*$:

$$T_b = \Psi(\lambda) - vk(\lambda - \lambda^*) \tag{3-6}$$

Plugging (3-6) into (3-4) and neglecting the disturbances yields

$$\dot{\lambda} = -p_1 k(\lambda - \lambda^*) \tag{3-7}$$

The key assumption here is that $\Psi(\lambda)$ (and thus $\mu(\lambda)$) is known, which is in real-life never the case. However, $\Psi(\lambda)$ can be approximated using an on-line friction estimation algorithm that uses a linear parameterisation as described in (2-11) and [14].

$$\mu(\lambda) = \boldsymbol{p}^T\boldsymbol{\phi}(\lambda) + \Delta_\mu(\lambda), \quad |\Delta_\mu(\lambda)| \leq \overline{\Delta}_\mu \quad \forall\lambda \in \Lambda \tag{3-8}$$

$$\boldsymbol{\phi}(\lambda) = [1\,\lambda\,e^{-4.99\lambda}\;e^{-18.43\lambda}\;e^{-65.62\lambda}]^T \tag{3-9}$$

where $\boldsymbol{p} \in \mathbb{R}^5$ is the set of linear parameters, $\boldsymbol{\phi}(\lambda)$ is the known regressor and $\Delta_\mu(\lambda)$ is the approximation error induced by the linear parameterisation, bounded by the known constant $\overline{\Delta}_\mu$.

By considering that $mr^2 \gg J$ and writing $\boldsymbol{\theta} = rF_z\boldsymbol{p}$, $\Psi(\lambda)$ can be rewritten as:

$$\Psi(\lambda) = \boldsymbol{\theta}^T\boldsymbol{\phi}(\lambda) + \Delta_{\Psi_1}(t,\lambda) + \Delta_{\Psi_2}(t,\lambda) \tag{3-10}$$

where

$$\left.\begin{array}{ll} \Delta_{\Psi_1}(t,\lambda) = (1-\lambda)p_2r\mu(\lambda)F_z, & |\Delta_{\Psi_1}(t,\lambda)| \leq p_2r\mu_{\max}\overline{F}_z \leq p_2r\overline{\Delta}_{\Psi_1} \\ \Delta_{\Psi_2}(t,\lambda) = rF_z\Delta_\mu, & |\Delta_{\Psi_2}(t,\lambda)| \leq r\overline{F}_z\overline{\Delta}_\mu \leq \overline{\Delta}_{\Psi_2} \end{array}\right\} \forall(t,\lambda) \in [0,\infty) \times \Lambda \tag{3-11}$$

and $\mu_{\max} = \max_\lambda \mu(\lambda)$ and $\overline{F}_z = \max_t F_z(t)$.

Defining the slip error as $e = \lambda - \lambda^*$ and using (3-4) and (3-10), the slip error dynamics are given by:

$$\dot{e} = -\frac{p_1}{v}\left(\boldsymbol{\theta}^T\boldsymbol{\phi}(\lambda) - T_b + \Delta(t,\lambda,v,\omega)\right) \tag{3-12}$$

where all model uncertainties are combined into $\Delta(t,\lambda,v,\omega)$.

$$\Delta(t,\lambda,v,\omega) = \Delta_{\Psi_1}(t,\lambda) + \Delta_{\Psi_2}(t,\lambda) - \Delta_\omega(t,\omega) + (1-\lambda)p_2r\Delta_v(t,v) \tag{3-13}$$

$$|\Delta(t,\lambda,v,\omega)| \leq \overline{\Delta}_{\Psi_2} + \overline{\Delta}_\omega + p_2r\left(\overline{\Delta}_v + \overline{\Delta}_{\Psi_1}\right) \leq \overline{\Delta} \quad \forall(t,\lambda,v,\omega) \in [0,\infty) \times \Lambda \times D \tag{3-14}$$

In analogue to the control law (3-6) for the perfect system the following control law is proposed:

$$T_b = \hat{\boldsymbol{\theta}}^T\boldsymbol{\phi}(\lambda) - vke \tag{3-15}$$

where $\hat{\boldsymbol{\theta}}$ is the estimate of $\boldsymbol{\theta}$, which will be defined by an adaptive algorithm. For the design of the adaptation law of $\hat{\boldsymbol{\theta}}$ the following Lyapunov function is considered:

$$V(e_\epsilon, \tilde{\boldsymbol{\theta}}) = \frac{1}{2}e_\epsilon^2 + \frac{p_1}{2\gamma v^2}\tilde{\boldsymbol{\theta}}^T\tilde{\boldsymbol{\theta}} \tag{3-16}$$

where $\tilde{\boldsymbol{\theta}} = \hat{\boldsymbol{\theta}} - \boldsymbol{\theta}$, $\gamma$ is a constant tuning parameter and $e_\epsilon$ is the regulation error with dead zone $\epsilon$:

$$e_\epsilon = \begin{cases} 0 & \text{if } |e| < \epsilon \\ e - \operatorname{sgn}(\epsilon)\epsilon & \text{if } |e| \geq \epsilon \end{cases} \tag{3-17}$$

$$\dot{e}_\epsilon = \begin{cases} 0 & \text{if } e_\epsilon = 0 \\ \dot{e} & \text{if } e_\epsilon \neq 0 \end{cases} \tag{3-18}$$

Due to the large differences in inertia, the longitudinal dynamics (3-2) are much slower than the rotational dynamics (3-1). Therefore we can assume that the velocity $v$ in (3-16) is a slowly varying parameter. Based on this assumption the time derivative of the Lyapunov function (3-16) is given by:

$$\dot{V} = e_\epsilon\dot{e}_\epsilon + \frac{p_1}{\gamma v^2}\tilde{\boldsymbol{\theta}}^T\dot{\hat{\boldsymbol{\theta}}} \tag{3-19}$$

For $e_\epsilon \neq 0$ we can rewrite this as

$$\begin{aligned}
\dot{V} &= e_\epsilon \dot{e} + \frac{p_1}{\gamma v^2}\tilde{\boldsymbol{\theta}}^T\dot{\tilde{\boldsymbol{\theta}}} \quad \forall e_\epsilon \neq 0 \\
&= -\frac{p_1}{v} e_\epsilon \left(-\tilde{\boldsymbol{\theta}}^T \boldsymbol{\phi}(\lambda) + vke + \Delta(t,\lambda,v,\omega)\right) + \frac{p_1}{\gamma v^2}\tilde{\boldsymbol{\theta}}^T\dot{\tilde{\boldsymbol{\theta}}} \\
&\leq -p_1 k e_\epsilon e + \frac{p_1}{v}\overline{\Delta}|e_\epsilon| + p_1\tilde{\boldsymbol{\theta}}^T\left(\frac{e_\epsilon}{v}\boldsymbol{\phi}(\lambda) + \frac{\dot{\tilde{\boldsymbol{\theta}}}}{\gamma v^2}\right) \quad \forall e_\epsilon \neq 0
\end{aligned} \tag{3-20}$$

To eliminate the last term the adaptation law is chosen to be

$$\hat{\boldsymbol{\theta}}(t) = \hat{\boldsymbol{\theta}}(t_i) - \int_{t_i}^{t} \gamma e_\epsilon(\tau) v(\tau) \boldsymbol{\phi}(\lambda(\tau)) d\tau \tag{3-21}$$

where $t_i$ is the activation instant of the controller. With the last term in (3-20) being canceled, plugging in $e = e_\epsilon + \epsilon\,\mathrm{sgn}(e_\epsilon)$ yields:

$$\dot{V} \leq -p_1 k e_\epsilon^2 - p_1 k |e_\epsilon| \left(\epsilon - \frac{\overline{\Delta}}{vk}\right) \quad \forall e_\epsilon \neq 0 \tag{3-22}$$

By selecting $\epsilon > \frac{\overline{\Delta}}{kv_0}$, where $v_0$ is the lowest velocity for which the controller is still active, we achieve $\dot{v} \leq -p_1 k e_\epsilon^2 \quad \forall e_\epsilon$. For $e_\epsilon = 0$, the adaptation law (3-21) remains constant and $\dot{V}(0, \tilde{\boldsymbol{\theta}}) = 0$. Hence,

$$\dot{V} \leq 0 \quad \forall e_\epsilon \tag{3-23}$$

We can also prove that the chosen update law (3-21) and dead zone $\epsilon$ are appropriate when we no longer consider $v$ to be a slowly varying parameter. In this case we should extend the Lyapunov function (3-16) with the term $\rho v$:

$$V(e_\epsilon, \tilde{\boldsymbol{\theta}}) = \frac{1}{2}e_\epsilon^2 + \frac{p_1}{2\gamma v^2}\tilde{\boldsymbol{\theta}}^T\tilde{\boldsymbol{\theta}} + \rho v \tag{3-24}$$

where $\rho$ is a constant. The derivative of the Lyapunov function then becomes:

$$\begin{aligned}
\dot{V} &= e_\epsilon \dot{e} + \frac{p_1}{\gamma v^2}\tilde{\boldsymbol{\theta}}^T\dot{\tilde{\boldsymbol{\theta}}} - \frac{p_1}{\gamma v^3}\tilde{\boldsymbol{\theta}}^T\tilde{\boldsymbol{\theta}}\dot{v} + \rho\dot{v} \quad \forall e_\epsilon \neq 0 \\
&= -\frac{p_1}{v} e_\epsilon \left(-\tilde{\boldsymbol{\theta}}^T \boldsymbol{\phi}(\lambda) + vke + \Delta(t,\lambda,v,\omega)\right) + \frac{p_1}{\gamma v^2}\tilde{\boldsymbol{\theta}}^T\dot{\tilde{\boldsymbol{\theta}}} - \frac{p_1}{\gamma v^3}\tilde{\boldsymbol{\theta}}^T\tilde{\boldsymbol{\theta}}\dot{v} + \rho\dot{v} \\
&\leq -p_1 k e_\epsilon e + \frac{p_1}{v}\overline{\Delta}|e_\epsilon| + p_1\tilde{\boldsymbol{\theta}}^T\left(\frac{e_\epsilon}{v}\boldsymbol{\phi}(\lambda) + \frac{\dot{\tilde{\boldsymbol{\theta}}}}{\gamma v^2}\right) + \left(\rho - \frac{p_1}{\gamma v^3}\tilde{\boldsymbol{\theta}}^T\tilde{\boldsymbol{\theta}}\right)\dot{v} \quad \forall e_\epsilon \neq 0
\end{aligned} \tag{3-25}$$

Since we consider a braking maneuver we know that $\dot{v} < 0$. To make sure the last term in (3-25) is $\leq 0$, we need to make sure that $\rho \geq \frac{p_1}{\gamma v^3}\tilde{\boldsymbol{\theta}}^T\tilde{\boldsymbol{\theta}}$. To prove such a $\rho$ exists, we need to prove that $\frac{p_1}{\gamma v^3}\tilde{\boldsymbol{\theta}}^T\tilde{\boldsymbol{\theta}} < \infty$. We know that $p_1$ and $\gamma$ are positive parameters and that the velocity is bounded from below by $v_0 > 0$ (the controller shuts down for lower velocities lower than $v_0$). Also, from physical reasoning we know that $\tilde{\boldsymbol{\theta}}^T\tilde{\boldsymbol{\theta}}$ is a positive finite term (the friction coefficient is finite). Hence there exists a $\rho$ such that $\rho \geq \frac{p_1}{\gamma v^3}\tilde{\boldsymbol{\theta}}^T\tilde{\boldsymbol{\theta}}$. With the last term proven to be non-positive we can now apply the same reasoning to the remainder of equation (3-25) as we did to equation (3-20).

### Initial Estimate Of The Tire-Road Forces

The controller presented above uses an estimate of the longitudinal tire force $F_z\mu(\lambda)$ to apply feedback linearisation. The (transient) performance of the controller is heavily influenced by the initialization of the tire force estimate.

The slip controller is activated when a certain slip threshold is exceeded at time $t = t_i$. Up to this point $t_i$ the braking torque $T_b$ is determined by the driver ($T_b(t) = T_d(t)$ for $t < t_i$). When the controller is activated, the braking torque $T_b$ is no longer determined by the driver, but by the controller ($T_b(t) = \hat{\boldsymbol{\theta}}^T(t)\boldsymbol{\Phi}(\lambda(t)) - kv(t)e(t)$). To avoid undesirable behavior as a result of discontinuities in the braking torque at time $t_i$ ($T_d(t_i) \neq \hat{\boldsymbol{\theta}}^T(t_i)\boldsymbol{\Phi}(\lambda(t_i)) - kv(t_i)e(t_i)$), the initial estimate of $\boldsymbol{\theta}$ should be chosen carefully:

$$\hat{\boldsymbol{\theta}}(t_i) = \boldsymbol{\theta}_N \frac{T_d(t_i) + kv(t_i)e(t_i)}{\boldsymbol{\theta}_N^T \boldsymbol{\Phi}(\lambda(t_i))}, \tag{3-26}$$

where $\boldsymbol{\theta}_N$ is the initial parameter estimate chosen by the designer. At the time the slip controller is initiated, the road surface is unknown. However, a reasonable initial guess for any road surface might be a wet asphalt track (see figure 2-3).

## 3-2-2 Braking Maneuver without Actuator Dynamics

To see how the controller performs, we simulated a $\mu$-jump braking maneuver without incorporating the actuator dynamics. We start at a velocity of $v = 100\,[\text{km/h}]$ and end the braking maneuver at $v = 15\,[\text{km/h}]$. The first $40\,[\text{m}]$ of the track have a friction coefficient of $\mu_{\max} = 0.6$ and for the second part of the track we have $\mu_{\max} = 0.2$. The results are displayed in figure 3-2.

In the top plot we see that the wheel slip increases as the braking torque is increased by the driver until the wheel slip exceeds the activation threshold $\lambda_{th} = 0.12$. Then the controller takes over and regulates the slip to 0.12. Around $t \approx 1.7\,[\text{s}]$, we see a spike in the wheel slip. This is the result of the change in friction coefficient ($\mu_{\max} = 0.6 \rightarrow \mu_{\max} = 0.2$). In the third plot we see that the controller quickly adapts the feedback linearisation term and the slip is once again regulated to its setpoint.

In the second plot you can clearly see that the deceleration is higher during the first couple of meters, where the friction coefficient is high. After the $\mu$-jump, the deceleration is lower.

The third plot displays the torque output of the controller (blue line). In the beginning the torque is increased by the driver, until at $t \approx 0.9\,[\text{s}]$ the controller is activated. The red line displays the proportional control term when the controller is active and the black line represents the feedback linearisation term. This figure clearly shows the importance of the feedback part of the control law, as it constitutes a major part of the total control output.

In the plot at the bottom, the actual and estimated tire forces are compared. Again, we see that the actual torque is gradually increased by the driver. During the activation of the controller we see that the initial value of the estimated tire force is a bit too high. The estimated value quickly converges to the actual value. When the $\mu$-jump happens, the friction coefficient is suddenly much lower and thus the actual tire force is also much lower. The controller quickly adapts to the different road surface and in a fraction of a second the estimated tire force converges to the actual tire force again.

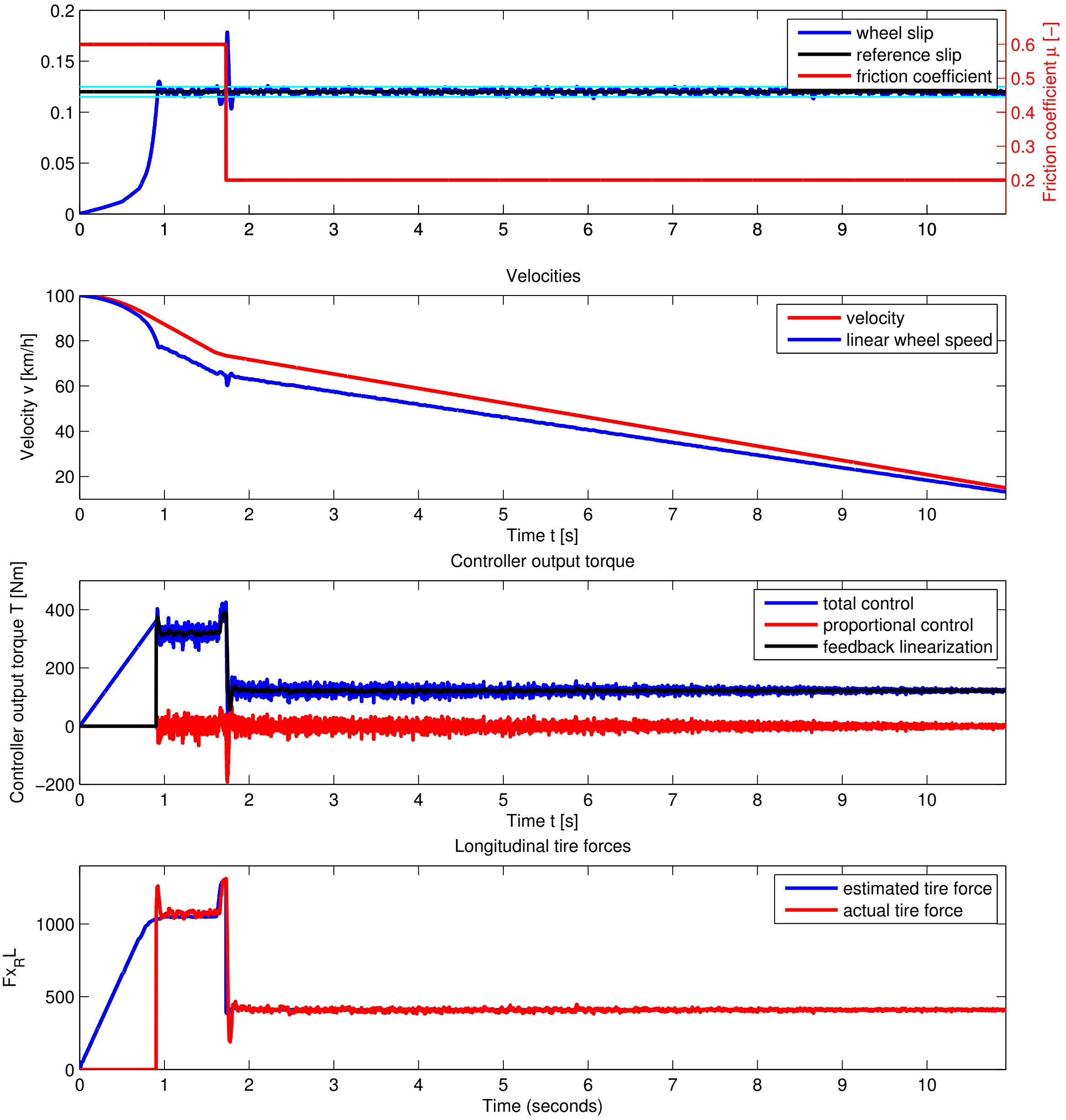

**Figure 3-2:** Braking maneuver on a $\mu$-jump surface without actuator dynamics

### 3-2-3 Influence of Output Uncertainty HAB on Controller Performance

When we recall equation (3-1), we know that the slip controller is designed to be able to cope with a torque disturbance $\Delta_\omega$. However, it is unclear to what extent the output uncertainty of the HAB influences the performance of the slip controller. To investigate this, we perform a braking maneuver on a wet asphalt track ($\mu_{\max} = 0.6$) from $100\,[\text{km/h}] \rightarrow 15\,[\text{km/h}]$ and we assign all braking torques to the hydraulic brakes for two different cases. The first case neglects the torque disturbance on the rear wheels and the second case takes the torque disturbance into account. The results of these maneuvers are shown in table 3-1 and figures 3-3 and 3-4, where the performance of the controller is measured by evaluating the root mean square (RMS) of the slip error $e_{rear}$.

As we can see in table 3-1 both the RMS of the slip error $e_{rear}$ and the estimation error $e_{est,rear}$ are significantly larger for the case where we do consider a torque disturbance compared to the case where we don't consider this disturbance. Not only during the transient period is the performance degraded, but the performance during the whole braking maneuver is worse. This can also be seen in the wheel slip plots in figures 3-3 and 3-4.

The controller output torque in figure 3-4 decreases after the transient period, but the actuator torque remains approximately constant during this period. This shows that the controller is able to compensate for the uncertainty in the friction coefficient $\nu$.

In the beginning of the braking maneuver the high velocity $v$ results in a decrease of the friction coefficient $\nu$ (see section 2-2-1). Also, during the entire maneuver the braking torque $T_b < 600\,[\text{Nm}]$ and remains approximately constant after the transient period, resulting in a lower value of the friction coefficient $\nu$. As time elapses and the velocity decreases, the friction coefficient $\nu$ increases. This phenomenon can be observed in the plot of the estimated tire forces in figure 3-4. In the beginning the tire force is overestimated since in reality the exerted braking torque is lower than the output of the slip controller, but as time elapses the estimated tire force approaches its actual value.

When we look at figure 3-3 we see that the slip converges nicely to its setpoint and remains within the deadzone, while in figure 3-4 the slip oscillates around the upper bound of the deadzone. It is the velocity dependence of $\nu$ that makes the slip do this. When the slip is within the deadzone, the tire force estimation is frozen. Since we are braking the velocity decreases and $\nu$ increases and thus the braking torque increases resulting in an increasing slip. When the slip leaves the deadzone, the tire-force estimation is updated again resulting in a lower feedback linearisation term which in turn lowers the slip until the slip is once again within the deadzone and we are at the starting point of the cycle.

**Table 3-1:** Influence of the output uncertainty of the hydraulic brakes on the controller performance. The transient part is considered to be the $1^{\text{st}}$ second after reaching the slip threshold

| Torque uncertainty | RMS $e_{rear}$ | | | RMS $e_{est,rear}$ | | |
|---|---|---|---|---|---|---|
| | total | transient | remainder | total | transient | remainder |
| on | 0.0108 | 0.0186 | 0.0053 | 54.65 | 94.70 | 26.32 |
| off | 0.0141 | 0.0218 | 0.0093 | 128.68 | 201.97 | 83.12 |

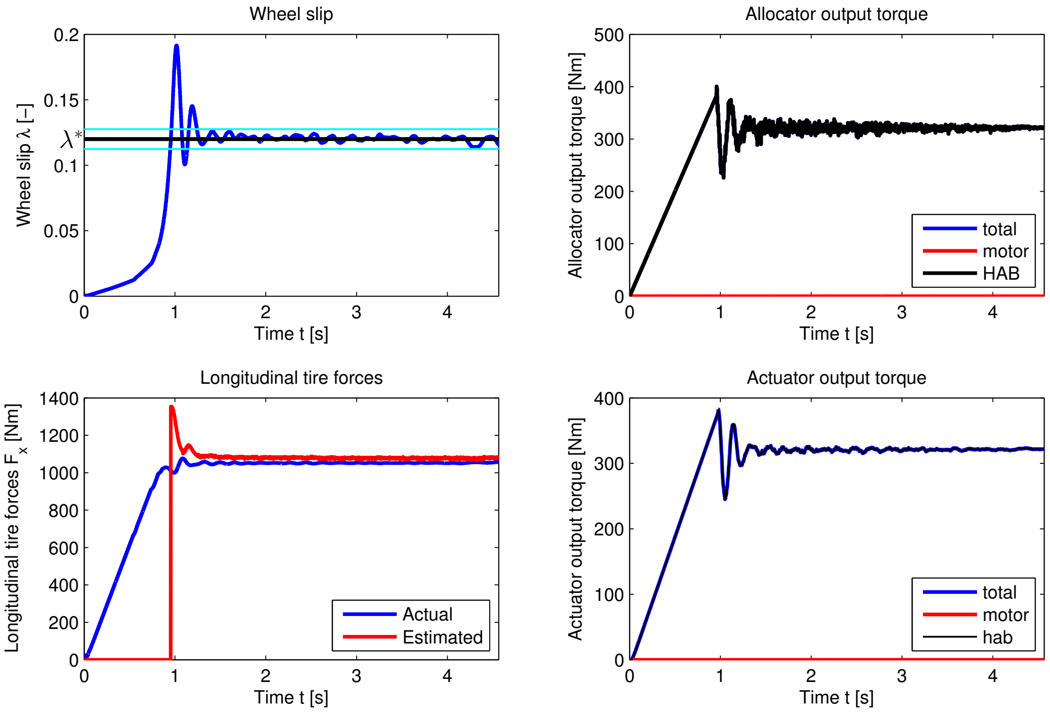

**Figure 3-3:** Braking on a wet asphalt track ($\mu_{\max} = 0.6$) using the hydraulic brakes without a torque disturbance on the rear wheels

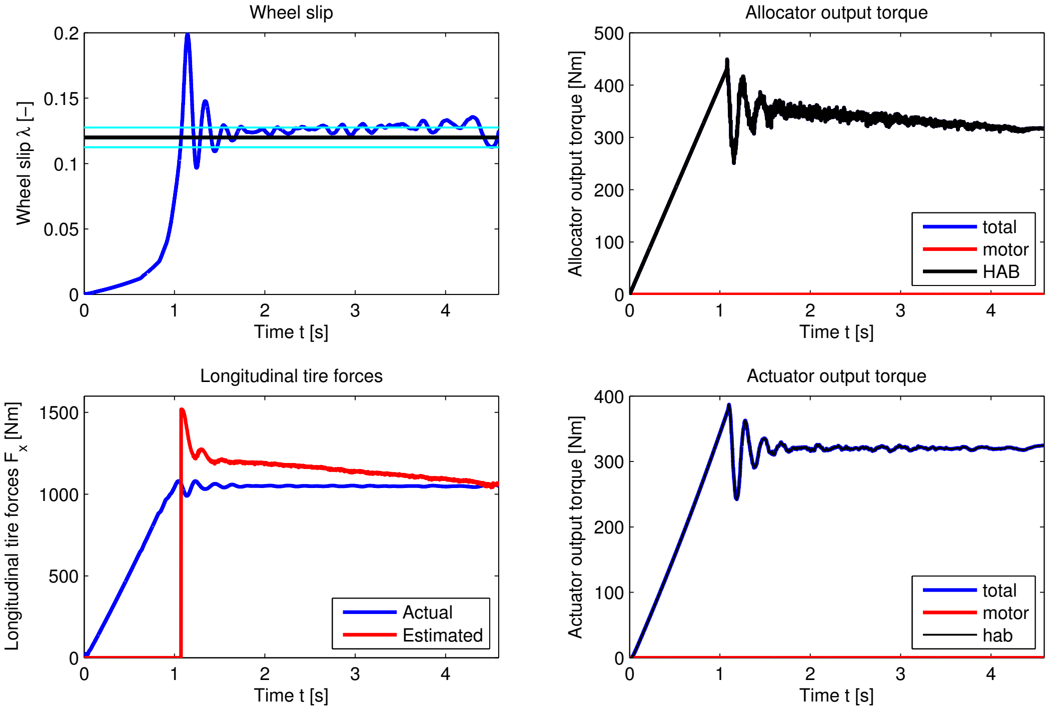

**Figure 3-4:** Braking on a wet asphalt track ($\mu_{\max} = 0.6$) using the hydraulic brakes with a torque disturbance on the rear wheels

### 3-2-4 Some Remarks on the Slip Controller

In section 2-1-2 it was pointed out that the braking dynamics are scaled by the reciprocal of the velocity $v$. This problem is dealt with in this controller by multiplying both the control gain $k$ and estimator gain $\gamma$ with the velocity. This is a significant different approach as proposed in [5], where the estimator gain $\gamma$ was divided by the velocity. For the approach in [5], despite a lot of tuning effort no tuning could be found that could deal with the low stopping velocity of 15 [km/h] when actuator dynamics are involved.

We could rewrite the update law (3-21) as

$$\hat{\boldsymbol{\theta}}(t) = \hat{\boldsymbol{\theta}}(t_i) - \int_{t_i}^{t} k_{ff}(\tau) e_\epsilon(\tau) \boldsymbol{\phi}(\lambda(\tau)) d\tau, \tag{3-27}$$

where in this work we use $k_{ff}(\tau) = \gamma v(\tau)$ and in [5] $k_{ff}(\tau) = \frac{\gamma}{v(\tau)}$ is used. When we perform a braking maneuver on a wet asphalt surface ($\mu_{\text{max}} = 0.6$) starting at a velocity of 100 [km/h] and using blended braking, we obtain the results displayed in figures 3-5 and 3-6. Comparable results are obtained using only the Hydraulic Actuated Brake (HAB) or different blended braking strategies.

In the bottom plots of figures 3-5 and 3-6 the term $k_{ff}$ is displayed as a function of time. In figure 3-5 we see that $k_{ff}$ starts at a low value, resulting in poor converge of the tire force estimate, and increases progressively when the velocity decreases. The high estimation gain results in instabilities at low velocities. By defining the estimation gain $k_{ff} = \gamma v$, we have a nice convergence of the estimated tire force and no instabilities at low velocity, see figure 3-6.

The velocity has also an influence on the robustness of the slip controller. This can be seen by looking at the term associated with the dead zone in equation (3-22):

$$-p_1 k |e_\epsilon| \left( \epsilon - \frac{\overline{\Delta}}{vk} \right)$$

We find that for higher velocities the influence of the uncertainties becomes smaller and a smaller dead zone $\epsilon$ is required. This suggests that the controller is better able to cope with the disturbances at high velocities. This is illustrated in figure 3-7.

In figure 3-7a we used a dead zone $\epsilon = 0.0005$. As time progresses (and velocity decreases), we see that the oscillations in the wheel slip increase resulting in a locked wheel at low velocity. In figure 3-7b we used a dead zone $\epsilon = 0.0075$ and we find that the controller is capable of dealing with the unmodelled dynamics and measurement noise and the wheel slip is regulated to its setpoint.

To analyse the performance of the controller in depth, we first need to design a control allocator that distributes the desired braking torque $T_b$ over both actuators. This will be the subject of the next chapter.

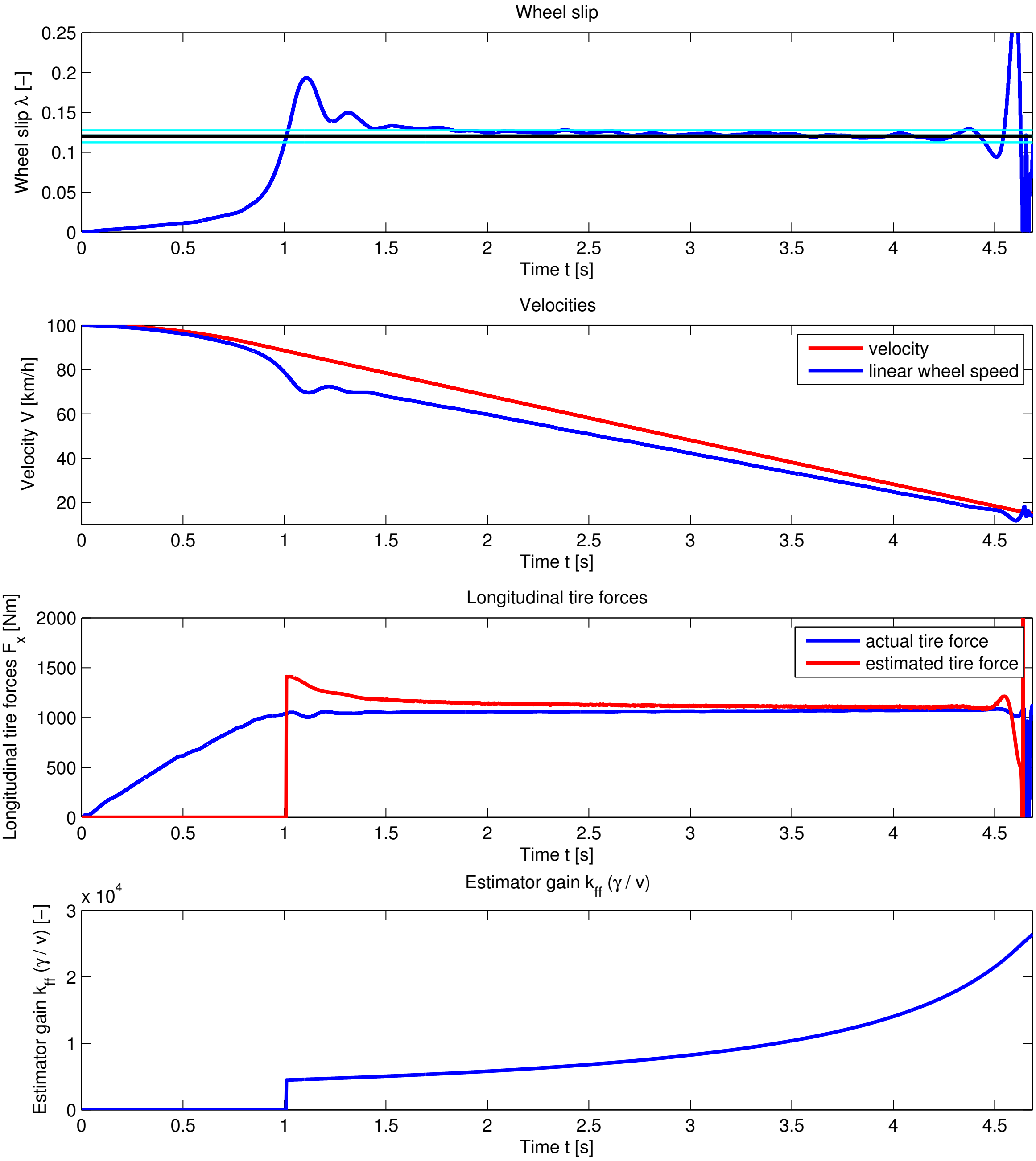

**Figure 3-5:** Braking maneuver on wet asphalt ($\mu_{\max} = 0.6$) using $k_{ff}(\tau) = \frac{\gamma}{v(\tau)}$

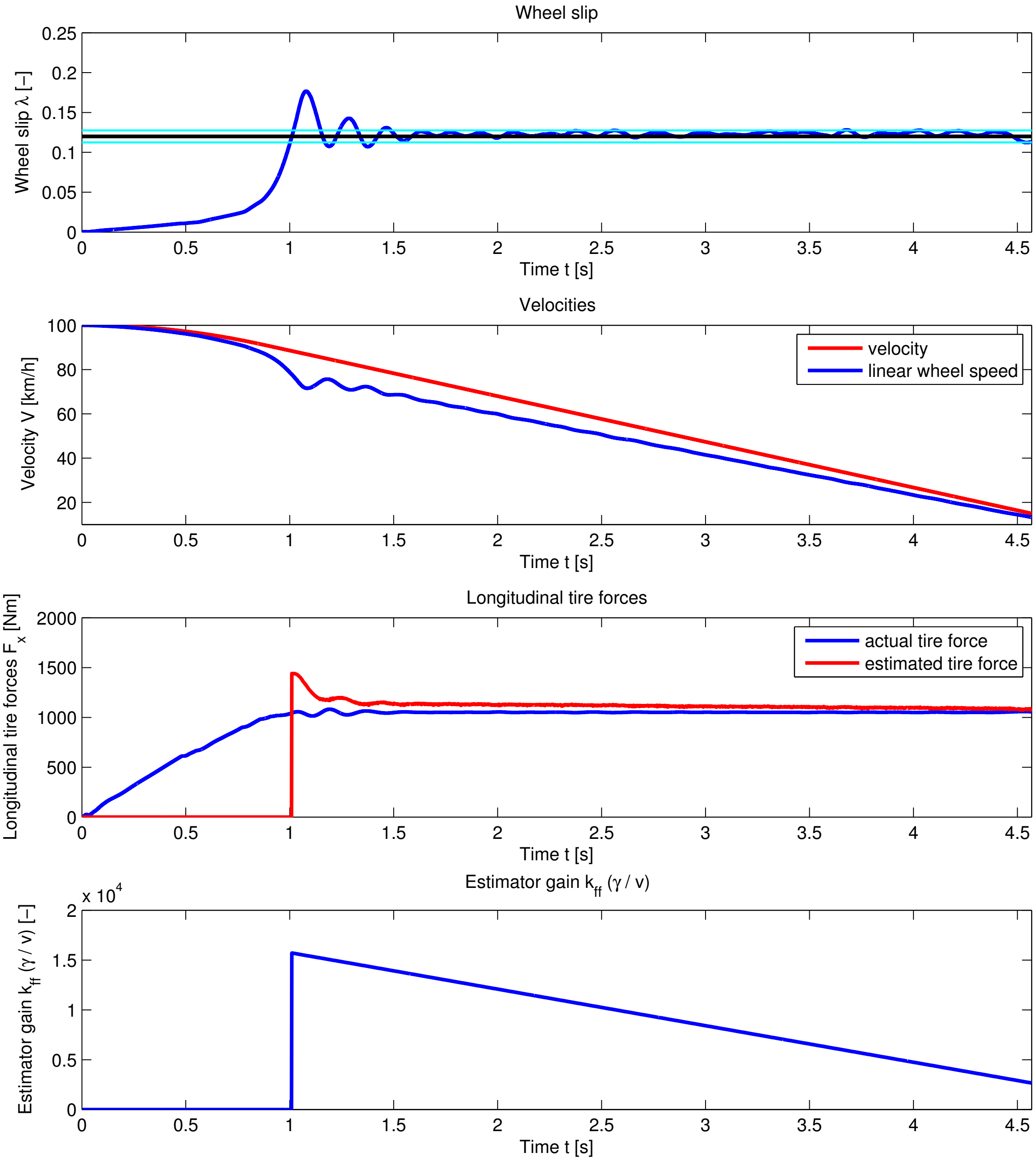

**Figure 3-6:** Braking maneuver on wet asphalt $(\mu_{\max} = 0.6)$ using $k_{ff}(\tau) = \gamma v(\tau)$

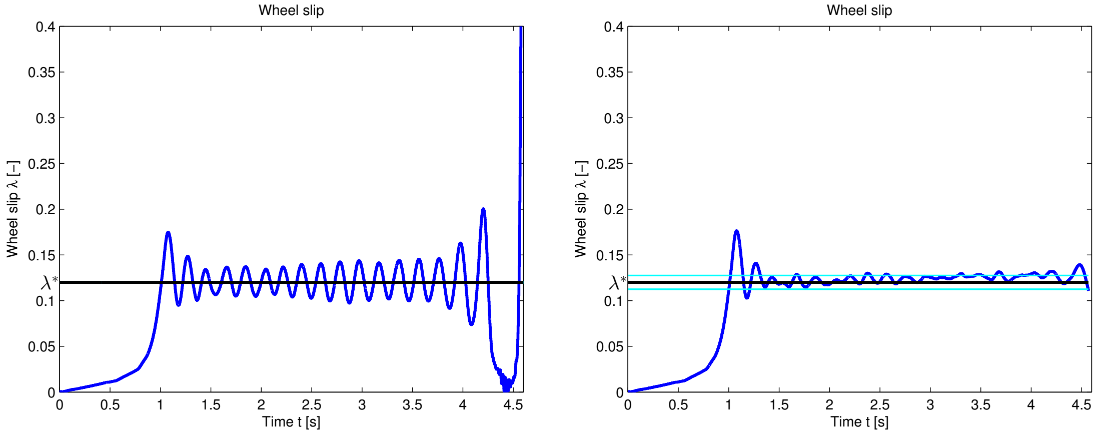

**(a)** Influence of dead zone ($\epsilon = 0.0005$)

**(b)** Influence of dead zone ($\epsilon = 0.0075$)

**Figure 3-7:** The effect of dead zone $\epsilon$

# Chapter 4

# Control Allocation

## 4-1 The Control Allocation Problem

In figure 2-1 the vehicle architecture considered in this work was displayed. It consists of four wheels being controlled by separate hydraulic actuators plus an electric motor braking both rear wheels. Since there are more actuators than controlled variables, the problem arises on how to distribute the necessary control action between the different actuators (see figure 4-1). It is assumed that the road conditions are symmetrical resulting in equal braking moments at both the left and right hand side of the vehicle.

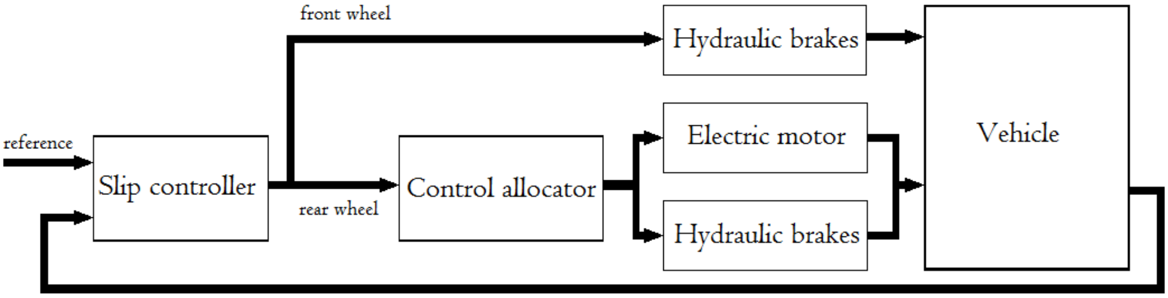

**Figure 4-1:** Control architecture

A general description of an over-actuated system is given by [29]:

$$\dot{\boldsymbol{x}} = f(t, \boldsymbol{x}) + g(t, \boldsymbol{x})\boldsymbol{\tau} \tag{4-1}$$

$$\boldsymbol{\tau} = h(t, \boldsymbol{x}, \boldsymbol{u}) \tag{4-2}$$

$$\dot{\boldsymbol{u}} = m(t, \boldsymbol{x}, \boldsymbol{u}, \boldsymbol{u}_d) \tag{4-3}$$

where $\boldsymbol{x} \in \mathbb{R}^n$ are the states, $\boldsymbol{\tau} \in \mathbb{R}^m$ is the virtual input vector, $\boldsymbol{u}_d \in \mathbb{R}^p$ is the desired control action sent to the actuators and $\boldsymbol{u} \in \mathbb{R}^p$ is the actual control action performed by the actuators. Since the system is over-actuated, we have $p > m$.

The control allocation problem is to find the desired control vector $\boldsymbol{u}_d \in \mathbb{R}^p$, such that

$$h(t, \boldsymbol{x}, \boldsymbol{u}) = \boldsymbol{\tau}^*, \quad \text{subject to} \tag{4-4}$$

$$\underline{\boldsymbol{u}}_c \leq \boldsymbol{u} \leq \overline{\boldsymbol{u}}_c \tag{4-5}$$

$$\underline{\dot{\boldsymbol{u}}}_c \leq \dot{\boldsymbol{u}} \leq \dot{\overline{\boldsymbol{u}}}_c \tag{4-6}$$

where $\underline{\boldsymbol{u}}_c$, $\underline{\dot{\boldsymbol{u}}}_c$, $\overline{\boldsymbol{u}}_c$ and $\dot{\overline{\boldsymbol{u}}}_c$ are limits on the range and rate of the actuators and $\boldsymbol{\tau}^*$ is the desired virtual control action.

In literature the actuator dynamics (4-3) are often neglected (($\boldsymbol{u} = \boldsymbol{u}_d$), see for example ([4],[30]). Furthermore, the mapping (4-2) of the control effectors $\boldsymbol{u}$ to the virtual control $\boldsymbol{\tau}$ is often assumed to be linear time-invariant:

$$\boldsymbol{\tau} = \boldsymbol{B}\boldsymbol{u} \tag{4-7}$$

In this work (4-7) holds and we take the actuator dynamics (4-3) into consideration, albeit implicitly. The control allocation problem then reduces to a linear control allocation problem which can be described as: find the desired control vector $\boldsymbol{u}_\mathrm{d} \in \mathbb{R}^n$, such that

$$\boldsymbol{B}\boldsymbol{u} = \boldsymbol{\tau}^*, \quad \text{subject to} \tag{4-8}$$

$$\underline{\boldsymbol{u}}_c \leq \boldsymbol{u} \leq \overline{\boldsymbol{u}}_c \tag{4-9}$$

$$\underline{\dot{\boldsymbol{u}}}_c \leq \dot{\boldsymbol{u}} \leq \dot{\overline{\boldsymbol{u}}}_c \tag{4-10}$$

where

$$\boldsymbol{B} = \begin{pmatrix} 1 & 0 & \frac{1}{2} \\ 0 & 1 & \frac{1}{2} \end{pmatrix}, \quad \boldsymbol{u} = \begin{pmatrix} T_{h_l} \\ T_{h_r} \\ T_m \end{pmatrix}, \quad \boldsymbol{u}_d = \begin{pmatrix} T_{h_l,d} \\ T_{h_r,d} \\ T_{m,d} \end{pmatrix} \quad \text{and} \quad \boldsymbol{\tau}^* = \begin{pmatrix} T_{b_l} \\ T_{b_r} \end{pmatrix} \tag{4-11}$$

and the subscripts $_l$ and $_r$ represent "left" and "right". Since we consider straight line braking on a symmetric road in this work, we have $T_{b_l} = T_{b_r}$, $T_{h_l} = T_{h_r}$ and $T_{h_l,d} = T_{h_r,d}$. Therefore we can simplify the allocation problem by defining:

$$\boldsymbol{B} = \begin{pmatrix} 1 & \frac{1}{2} \end{pmatrix}, \quad \boldsymbol{u} = \begin{pmatrix} T_h \\ T_m \end{pmatrix}, \quad \boldsymbol{u}_d = \begin{pmatrix} T_{h,d} \\ T_{m,d} \end{pmatrix} \quad \text{and} \quad \boldsymbol{\tau}^* = T_b \tag{4-12}$$

In practice, the control allocation is implemented in discrete time and (4-5) and (4-6) can be combined into a single constraint on the actuator range:

$$\underline{\boldsymbol{u}} \leq \boldsymbol{u} \leq \overline{\boldsymbol{u}} \tag{4-13}$$

where

$$\overline{\boldsymbol{u}} = \min(\overline{\boldsymbol{u}}_c, \boldsymbol{u} + t_s \dot{\overline{\boldsymbol{u}}}_c) \tag{4-14}$$

$$\underline{\boldsymbol{u}} = \max(\underline{\boldsymbol{u}}_c, \boldsymbol{u} - t_s \underline{\dot{\boldsymbol{u}}}_c) \tag{4-15}$$

and $t_s$ is the sample time.

In [30] several control allocation techniques like explicit ganging, daisy chaining and the weighted pseudo inverse method are presented. However, neither one of them take the actuator dynamics into consideration.

In [31] a model predictive control allocation scheme is presented which takes the actuator dynamics into account explicitly. A fundamental limitation of this allocation method is that the virtual control input $\boldsymbol{\tau}$ is assumed to be known in advance for the duration of the prediction horizon. This assumption is invalid in the field of braking control, since the future road conditions are unknown.

Härkegård proposes in [32] to pose the control allocation problem as a sequential quadratic programming (SQP) problem:

$$\boldsymbol{u}(t) = \arg \min_{\boldsymbol{u}(t)\in\Omega} \left( ||\boldsymbol{W}_1 \left(\boldsymbol{u}(t) - \boldsymbol{u}_s(t)\right)||_2^2 + ||\boldsymbol{W}_2 \left(\boldsymbol{u}(t) - \boldsymbol{u}(t-t_s)\right)||_2^2 \right) \tag{4-16}$$

$$\Omega = \arg \min_{\underline{\boldsymbol{u}}(t)\leq \boldsymbol{u}(t) \leq \overline{\boldsymbol{u}}(t)} ||\boldsymbol{W}_\tau \left(\boldsymbol{B}\boldsymbol{u}(t) - \boldsymbol{\tau}^*(t)\right)||_2 \tag{4-17}$$

where $\boldsymbol{W}_1$, $\boldsymbol{W}_2$ and $\boldsymbol{W}_\tau$ are weighting matrices, $\boldsymbol{u}_s(t)$ is the desired steady state control action and $t_s$ is the sampling time.

Equation (4-17) determines the set of feasible control inputs with respect to the actuator constraints that minimizes the weighted virtual control error. When $\Omega$ is not a single point, (4-16) determines the control action that minimizes a cost function that penalizes both deviations from the desired steady-state value and changes in the control action. Large values on the diagonal of $\boldsymbol{W}_1$ result in quick convergence to the desired steady-state values whereas large values on the diagonal of $\boldsymbol{W}_2$ prevent the actuator from moving too quickly. This way the actuator dynamics are taken into account implicitly.

In [5] a control allocation scheme is presented which is in essence similar to the SQP method. However, a numerically efficient solver is introduced using a closed-form solution of the optimization problem. This makes this method the best candidate to solve the control allocation problem. The dynamic allocation method is presented in detail in the next section.

## 4-2 Dynamic Allocation

In [5] the hybrid braking problem of a vehicle with 4 separate in-wheel motors is discussed. A numerically efficient method is developed to make real-time implementation of the optimization based algorithm possible. We adapted the method slightly, since we limit the motor to act in its braking mode.

For each rear wheel the torque allocation can be formulated as the following optimization problem:

$$\min_{T_h,T_m} \left(\alpha_h T_h^2 + \alpha_m T_m^2\right) + \left(\beta_h (T_h - T_h[k-1])^2 + \beta_m (T_m - T_m[k-1])^2\right) \tag{4-18}$$

$$\text{s.t.}\, T_h + T_m = T_b, \quad \underline{T_i} \leq T_i \leq \overline{T_i}, \quad i \in \{e, f\}, \tag{4-19}$$

where $T_h$, $T_m$ and $T_b$ are the commanded torques of the Hydraulic Actuated Brake (HAB) and the electric motor and the total desired torque computed by the slip controller. The rate and range limits of the actuators are given by:

$$\left.\begin{aligned} \underline{T_i} &= \max\left(T_{i,min}, T_i[k-1] - t_s \dot{T}_{i,max}\right) \\ \overline{T_i} &= \min\left(T_{i,max}, T_i[k-1] + t_s \dot{T}_{i,max}\right) \end{aligned}\right\} i = \{h, m\} \tag{4-20}$$

The first term in (4-18) penalizes the use of both actuators using the weights $\alpha_h$ and $\alpha_m$. The second term in (4-18) puts weights on the frequency contents of the control signal. This term assigns the high-frequency content of the control signal to the fastest actuator.

## 4-2-1 Numerical Solver

A numerically efficient solver for finding the solution of (4-18) subject to the actuator constraints (4-19) is presented next:

1. check if the requested torque $T_b$ is feasible:

$$\boldsymbol{T} = (T_h, T_m) = \begin{cases} (\overline{T_h}, \overline{T_m}) & \text{if } T_b > \overline{T_h} + \overline{T_m} \\ (\underline{T_h}, \underline{T_m}) & \text{if } T_b < \underline{T_h} + \underline{T_m} \\ \text{go to step 2} & \text{otherwise} \end{cases} \tag{4-21}$$

2. compute the unconstrained optimal solution $\boldsymbol{T^u} = (T_h^u\, T_m^u)^T$ using:

$$\frac{T_h}{T_b}(z) = \frac{\alpha_m + \beta_m}{l}\frac{z - a_f}{z - p}, \quad \frac{T_m}{T_b}(z) = \frac{\alpha_h + \beta_h}{l}\frac{z - a_e}{z - p}, \tag{4-22}$$

$$a_f = \frac{\beta_m}{\alpha_m + \beta_m}, \quad a_e = \frac{\beta_h}{\alpha_h + \beta_h}, \quad p = \frac{\beta_h + \beta_m}{l}, \tag{4-23}$$

$$l = \alpha_h + \alpha_m + \beta_h + \beta_m \tag{4-24}$$

   If this solution satisfies the inequality constraints, then $\boldsymbol{T} = \boldsymbol{T^u}$. Otherwise, go to step 3.

3. $T_b$ is feasible but $\boldsymbol{T^u}$ does not fulfill the inequality constraints. Using the equality constraint in (4-19) and individually activating each of the inequalities results in four candidate solutions: $\left\{(T_b - \overline{T_m}, \overline{T_m}), (T_b - \underline{T_m}, \underline{T_m}), (\overline{T_h}, T_b - \overline{T_h}), (\underline{T_h}, T_b - \underline{T_h})\right\}$. We neglect the candidates that violate (4-19) and choose the candidate that minimizes (4-18).

What follows next is the derivation of the transfer functions used in step 2. When we neglect the inequality constraints in (4-19), the Lagrangian function of the optimization problem is defined as:

$$\begin{aligned} \mathcal{L}(T_h, T_m, \lambda_L) =& \alpha_h T_h^2 + \alpha_m T_m^2 + \beta_h (T_h - T_h[k-1])^2 + \\ & \beta_m (T_m - T_m[k-1])^2 + \lambda_L (T_m + T_h - T_b), \end{aligned} \tag{4-25}$$

where $\lambda_L$ is the Lagrange multiplier. The first order optimality conditions are:

$$\frac{\partial \mathcal{L}}{T_m} = 2\alpha_m T_m + 2\beta_m (T_m - T_m[k-1]) + \lambda_L = 0 \tag{4-26}$$

$$\frac{\partial \mathcal{L}}{T_h} = 2\alpha_h T_h + 2\beta_h (T_h - T_h[k-1]) + \lambda_L = 0 \tag{4-27}$$

$$\frac{\partial \mathcal{L}}{\lambda_L} = T_h + T_m - T_b = 0 \tag{4-28}$$

The optimal solution obtained by solving equations (4-26) - (4-28) is given by:

$$\begin{bmatrix} T_m \\ T_h \end{bmatrix} = \frac{1}{l} \begin{bmatrix} \beta_m & -\beta_h \\ -\beta_m & \beta_h \end{bmatrix} \begin{bmatrix} T_m[k-1] \\ T_h[k-1] \end{bmatrix} + \frac{1}{l} \begin{bmatrix} \alpha_h + \beta_h \\ \alpha_m + \beta_m \end{bmatrix} T_b = \boldsymbol{A} \begin{bmatrix} T_m[k-1] \\ T_h[k-1] \end{bmatrix} + \boldsymbol{B} T_b, \tag{4-29}$$

which can be rewritten using the shift operator $q$ as:

$$\begin{bmatrix} T_m \\ T_h \end{bmatrix} = (q\boldsymbol{I} - \boldsymbol{A})^{-1} q \boldsymbol{B} T_b = \begin{bmatrix} \frac{\alpha_h+\beta_h}{l} \frac{z-a_e}{z-p} \\ \frac{\alpha_m+\beta_m}{l} \frac{z-a_f}{z-p} \end{bmatrix} T_b \tag{4-30}$$

The actuator dynamics are taken into account implicitly by constructing the weights $\beta_m$ and $\beta_h$ so that the high frequency content of the control signal is fed to the fastest actuator.

### 4-2-2 Selection of Allocation Weights

In chapter 2 we presented the models of both actuators. When we compare the magnitude of the bode diagrams of the transfer functions of both actuators (equations 2-23 and 2-25), we find that they have approximately the same bandwidth (defined as the frequency where the bode diagram intersects the $-3$ [dB] line). This can be seen in figure 4-2, which was already introduced earlier in chapter 2.

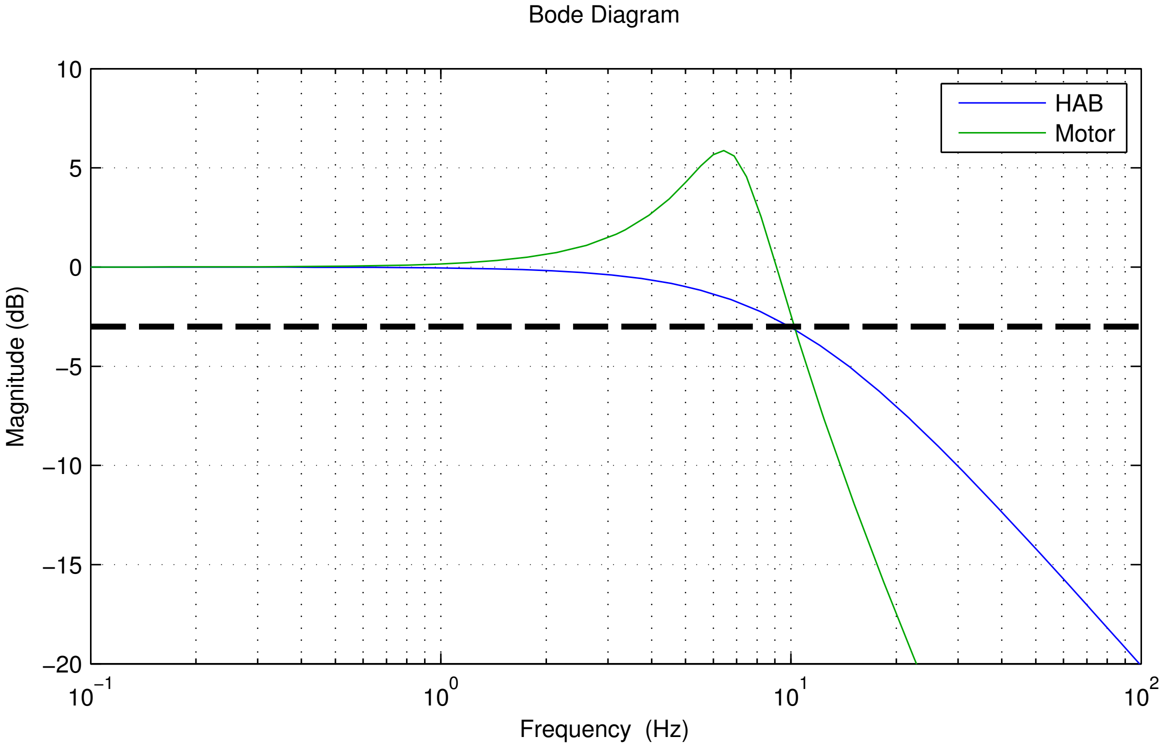

**Figure 4-2:** Bode diagrams of $G_h$ and $G_m$

The motor model has a damped resonance peak around 6.5 [Hz], but its effects are already noticeable at frequencies $> 1$ [Hz]. Therefore it seems favorable to allocate the frequency content of the torque signal $T_b$ at frequencies higher than 1 [Hz] to the HAB. This means that $\beta_m > \beta_h$.

For the allocation of the low frequency content of the torque signal there are two considerations we need to bear in mind. First of all we need to consider the imprecise nature of the HAB, as explained in chapter 2. Since the electric motor is better able to track a low frequency reference signal than the HAB (see figures 2-10c and 2-10e), allocating the low frequency content of $T_b$ to the motor would be favorable.

On the other side we have that the minimum lower bound of the braking torque of the HAB is $\underline{T_h} = 0\,[\mathrm{Nm}]$. As we saw in figures 2-10d and 2-10f the HAB is better able to follow a high frequency reference signal than the electric motor. However, to be able to decrease the hydraulic braking torque by a certain amount $\Delta_T$ at time $t = t_{\text{decrease}}$, we need that $T_h(t^-_{\text{decrease}}) > \Delta_T$. Therefore it is paramount that a sufficient large portion of the low frequency content of $T_b$ is allocated to the HAB.

We will consider five different control allocation strategies. The first one is an immediate shutdown of the motor, the second on is a gradual shutdown of the motor and the final three strategies have different ratios of distribution of the low frequency part of the control signal over the motor and the hydraulic brakes. The resulting allocation filters are displayed in figure 4-3 and the weights are given in table 4-1. Using these different configurations, we are able to investigate how the incorporation of the electric motor into the ABS algorithm influences its performance.

**Table 4-1:** Allocation weights for the different control allocation strategies

| allocation strategy | # | $\alpha_m$ | $\alpha_h$ | $\beta_m$ | $\beta_h$ |
|---|---|---|---|---|---|
| shut down motor | 1 | [-] | [-] | [-] | [-] |
| gradual shut down motor | 2 | 0.01 | 0 | 0.95 | 0.05 |
| 25% motor, 75% HAB | 3 | 0.003 | 0.001 | 0.95 | 0.05 |
| 50% motor, 50% HAB | 4 | 0.001 | 0.001 | 0.95 | 0.05 |
| 75% motor, 25% HAB | 5 | 0.00045 | 0.00135 | 0.95 | 0.05 |

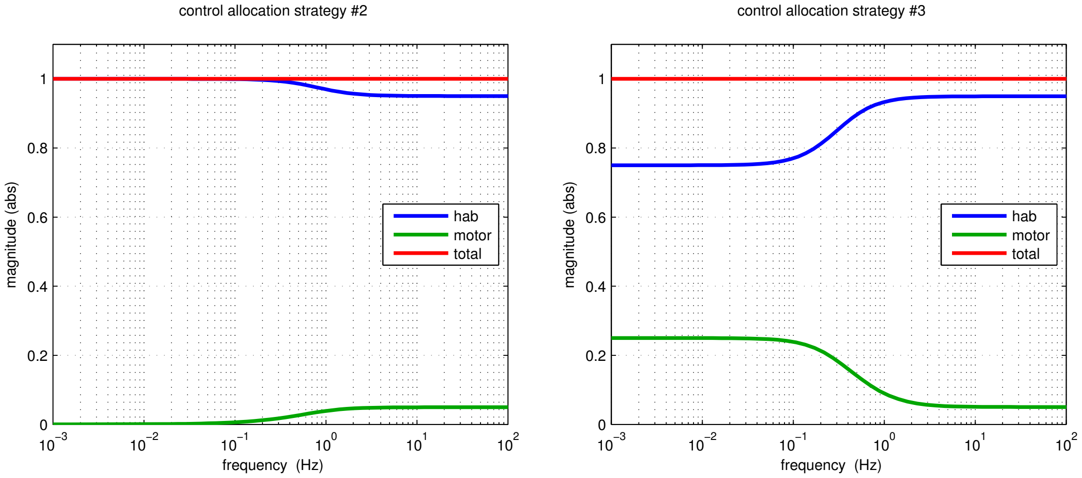

**(a)** Control allocation strategy $\#2$ **(b)** Control allocation strategy $\#3$

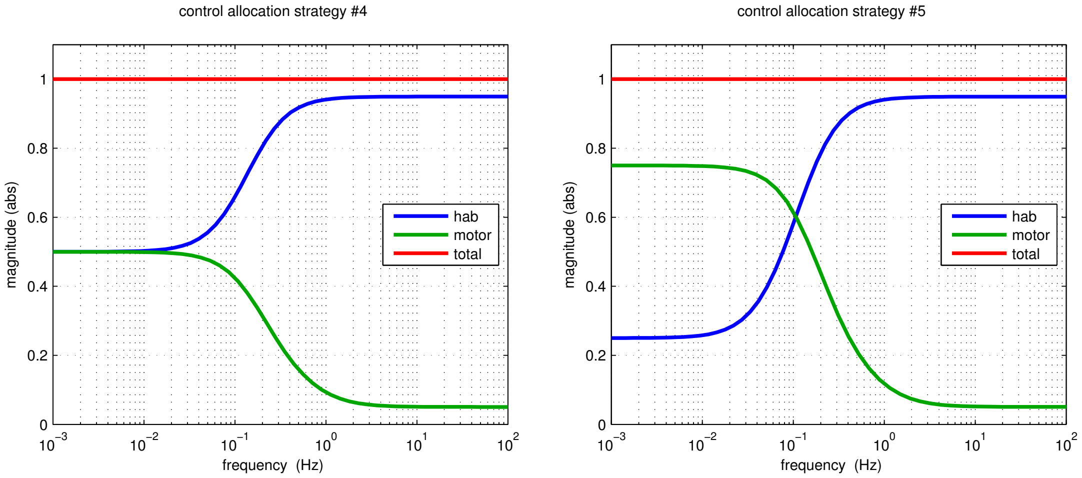

**(c)** Control allocation strategy $\#4$ **(d)** Control allocation strategy $\#5$

**Figure 4-3:** Filters for the unconstrained optimal solution of equation 4-18 using $4$ different combinations of allocation weights

# Chapter 5

# Results

Now that we have a control allocator in place, we can start analyzing the difference in performance when the electric motor is incorporated in the Anti-lock Braking System (ABS) algorithm. For this analysis, we assume that the braking maneuver starts as a regular braking maneuver where recuperating energy has a high priority. Therefore, only the motor is being used to brake the rear wheels until it either reaches its maximum torque or the slip threshold is exceeded. At that point the control allocator will distribute the torque using one of the five control allocation strategies defined in chapter 4 and summarized in table 4-1.

To analyze the difference in performance when using these five strategies we perform the following braking maneuvers. Braking on:

1. a wet asphalt track ($\mu_{\max} = 0.6$) from 100 [km/h] → 15 [km/h]
2. a snowy track ($\mu_{\max} = 0.2$) from 100 [km/h] → 15 [km/h]
3. a wet asphalt track which changes abruptly to a snowy track after 40 [m] ($\mu$-jump track) from 100 [km/h] → 15 [km/h]

The choice for these road surfaces is based on the fact that their friction coefficients are relatively low, increasing the odds for wheel-lock to occur without ABS. The use of the wet asphalt and snow track will reveal the ability of the controller to cope with different road conditions. The $\mu$-jump surface is a great way to test how the controller adapts to sudden changes in these road conditions.

The performance criterion used in this work is the root mean square (RMS) of the slip error of one of the rear wheels. Using the braking distance is not a good criterion, since we do not necessarily use the slip corresponding to the maximum friction coefficient as the setpoint. Finding the optimum slip setpoint is outside the scope of this work and it is assumed that a slip setpoint is given by a high level controller (like the Electronic Stability Program (ESP)). In this chapter we will use $\lambda^* = 0.12$ as the setpoint, but the controller is perfectly capable of regulating the slip at different setpoints. See for example figure 5-1, where we used allocation strategy #4 on a $\mu$-jump track with a setpoint of $\lambda^* = 0.6$.

All results presented in this chapter are based on data from the rear wheels.

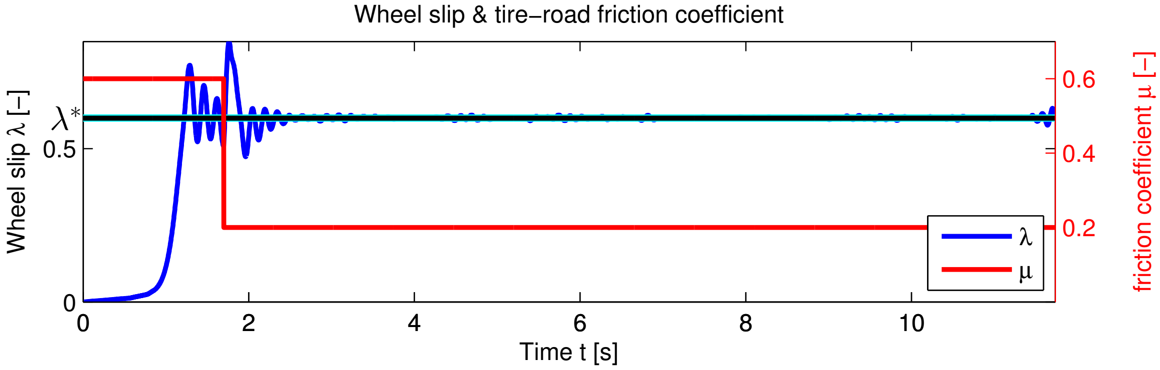

**Figure 5-1:** Braking on a $\mu$-jump track using allocator strategy $\#4$ and setpoint $\lambda^* = 0.6$

## 5-1 Tuning the Controller

Since the controller and allocator are designed as a modular system we have that from the controller's point of view, the model of the vehicle changes whenever we change the actuator configuration. This means we need to find separate tunings for each allocation strategy. Ideally, we would also have different tunings for the different road surfaces. However, the slip controller has to work for all surfaces. When we use different tunings for different surfaces, we have to incorporate some gain scheduling mechanism based on the road conditions, which would complicate the design of the controller enormously.

The controller tunings for all five control allocation strategies are obtained by brute force; for each allocation strategy and road surface we simulated braking maneuvers for a wide range of tuning parameters $k$ and $\gamma$, which are stored in vectors $\boldsymbol{k} \in \mathbb{R}^n$ and $\boldsymbol{\gamma} \in \mathbb{R}^n$. For each allocation strategy this resulted in three vectors containing the RMS of the slip error: $\boldsymbol{e}_c \in \mathbb{R}^n$, where $c = \{w, s, \mu\}$. The set of subscripts $\{w, s, \mu\}$ stands for respectively wet asphalt, snow and $\mu$-jump. From these three vectors we obtain three new vectors $\boldsymbol{x}_c \in \mathbb{R}^n$ whose entries represent the relative deviation of their corresponding entries in $\boldsymbol{e}_c$ from the optimum value in $\boldsymbol{e}_c$:

$$x_c(i) = \frac{e_c(i) - \min_i e_c(i)}{\min_i e_c(i)}, \qquad c = \{w, s, \mu\}, \qquad i = 1, \ldots, n \tag{5-1}$$

We now define the following cost function:

$$\boldsymbol{J} = \boldsymbol{x}_w + \boldsymbol{x}_s + \boldsymbol{x}_\mu \tag{5-2}$$

We than have that the the optimal tuning is given by:

$$k^* = k(i^*) \tag{5-3}$$

$$\gamma^* = \gamma(i^*) \tag{5-4}$$

where $i^*$ is the argument of the following optimization problem:

$$i^* = \arg\min_i J(i) \qquad \text{subject to} \tag{5-5}$$

$$1 \leq i \leq n \tag{5-6}$$

The values of the tuning parameters for the five different control allocation strategies are given in table A-2.

## 5-2 Comparison of Control Allocation Strategies

In this section we will present the results from the three braking maneuvers using the five different control allocation strategies. The RMS values of the slip error $e$ and estimation error $e_{est}$ are displayed in table 5-1. For each braking maneuver we will display a relevant selection of figures to support the discussion of the results. For more figures of all braking simulations performed, the reader is referred to appendix B.

In this chapter we will often refer to the 'transient' period and the 'remainder' of the braking maneuver. The transient period is for maneuvers 1 and 2 considered to be the $1^{st}$ second after reaching the slip threshold and for maneuver 3 we chose this period to be 2 seconds. The remainder of the braking maneuver is of course the time interval after the transient period. Dividing the braking maneuver in these two intervals allows us to better understand how the different control allocation strategies influence the slip regulation performance.

Let us first take a look at the values of the RMS of the estimation error $e_{est}$ in table 5-1. For all three braking maneuvers, we observe that these values decrease when we increase the low frequency contribution of the electric motor. For the snowy road the RMS of $e_{est}$ has decreased by 42.2% comparing strategy #1 with strategy #5. Including the electric motor in the ABS algorithm instead of (gradually) shutting down the electric motor does have a beneficial effect on the estimation error.

When we look at the RMS value of $e$ we see that an improved tire force estimate does not necessarily mean that the performance is improved. When we are braking on a wet asphalt track, the performance does improve when we incorporate regenerative braking into the ABS algorithm. On a snowy road however this conclusion would be incorrect and for the $\mu$-jump track this conclusion would only be partially correct. In the next sections we will study the results of each maneuver in greater detail.

**Table 5-1:** Comparison of the performance using five different control allocation strategies

| Maneuver | Strategy | RMS $e$ | | | RMS $e_{est}$ | | |
|---|---|---|---|---|---|---|---|
| | | total | transient | remainder | total | transient | remainder |
| wet asphalt | #1 | 0.0158 | 0.0250 | 0.0101 | 124.95 | 196.60 | 81.20 |
| wet asphalt | #2 | 0.0122 | 0.0168 | 0.0098 | 122.73 | 189.31 | 83.26 |
| wet asphalt | #3 | 0.0118 | 0.0175 | 0.0087 | 110.12 | 162.30 | 81.01 |
| wet asphalt | #4 | 0.0121 | 0.0186 | 0.0082 | 102.08 | 154.78 | 71.54 |
| wet asphalt | #5 | 0.0117 | 0.0190 | 0.0070 | 93.48 | 148.91 | 58.97 |
| snow | #1 | 0.0073 | 0.0186 | 0.0053 | 57.32 | 132.48 | 45.84 |
| snow | #2 | 0.0073 | 0.0184 | 0.0054 | 54.48 | 118.55 | 45.25 |
| snow | #3 | 0.0075 | 0.0199 | 0.0053 | 44.94 | 107.75 | 34.97 |
| snow | #4 | 0.0075 | 0.0201 | 0.0052 | 38.34 | 108.06 | 24.87 |
| snow | #5 | 0.0075 | 0.0202 | 0.0052 | 33.15 | 106.94 | 15.44 |
| $\mu$-jump | #1 | 0.0237 | 0.0522 | 0.0055 | 94.17 | 201.86 | 32.44 |
| $\mu$-jump | #2 | 0.0229 | 0.0505 | 0.0055 | 92.61 | 197.84 | 32.95 |
| $\mu$-jump | #3 | 0.0218 | 0.0480 | 0.0053 | 84.38 | 182.57 | 26.33 |
| $\mu$-jump | #4 | 0.0225 | 0.0497 | 0.0053 | 81.54 | 178.91 | 20.76 |
| $\mu$-jump | #5 | 0.0239 | 0.0528 | 0.0052 | 80.45 | 179.13 | 13.81 |

### 5-2-1 Wet Asphalt Braking Maneuver

Based on the RMS values of the slip error presented in table 5-1, we can conclude that suddenly shutting down the motor when entering an emergency braking situation is not the best strategy when braking on a wet asphalt track. As we can see in figure 5-2 this strategy introduces discontinuities in the torque signals sent to the HAB and the motor. The HAB is not capable of following the sudden increase in its input and the motor torque starts to oscillate due to the sudden decrease in its input. This explains the much larger slip error in the transient time interval compared to the other allocation strategies. By shutting down the motor gradually the slip regulation improves significantly. We no longer have discontinuities in the input signals of the motor and the HAB, see figure 5-3. This is translated in much smaller differences between the output of the allocator and the actuators.

When we increase the percentage of low frequency content of the control signal sent to the motor, two things happen. In table 5-1 we see that the transient performance degrades while the performance during the remainder of the maneuver improves. This does not only hold for the case of braking on wet asphalt, but also for the other two maneuvers.

The decrease of performance during the transient period is due to a larger excitation of the motor and driveline dynamics in the mid frequency range ($\approx 0.05\,[\text{Hz}] \leftrightarrow 1.5\,[\text{Hz}]$) for higher ratios of $\frac{\alpha_h}{\alpha_m}$, where $\alpha_m$ and $\alpha_h$ are allocation weights defined in chapter 4. This can also be seen in figure 4-3, where the magnitude of the bode diagrams of the optimal filters are displayed. The transition from low frequency to high frequency distribution is steeper for strategies with higher ratios of $\frac{\alpha_h}{\alpha_m}$.

The increase in performance in the remainder of the maneuver is the result of the fact that the estimation of the longitudinal tire force is improved. This can be seen in figures 5-4 to 5-6. In section 3-2-3 we already investigated the influence of the torque uncertainty on the performance. When for the low frequency content the ratio $\frac{T_m}{T_h}$ increases, the controller has less output uncertainty to compensate for and after the transient period of the maneuver the slip is less prone to oscillate around the upper bound of the deadzone.

### 5-2-2 Snowy Road Braking Maneuver

When we compare the RMS values of the slip error of the braking maneuver on a snowy road (see table 5-1), we find that gradually and immediately shutting down the motor results in almost the same performance. Both strategies quickly reduce the motor torque which results in some oscillations for a short period of time, see figure 5-7 and 5-8.

Including the motor in the ABS algorithm seems to degrade the performance a little. This is especially the case during the transient period of the maneuver, because at the time the slip controller is activated the hydraulic brakes are barely exerting any torque while at this time a large decrease of torque is demanded. Since the HAB is barely activated, this decrease of torque is demanded from the motor resulting in oscillations, see for example figure 5-9.

During the remainder of the braking maneuver the performance is slightly increased by incorporating the electric motor in the ABS, but this is negligible compared to the loss of performance during the transient period. For this particular braking maneuver, gradually shutting down the motor is the best option.

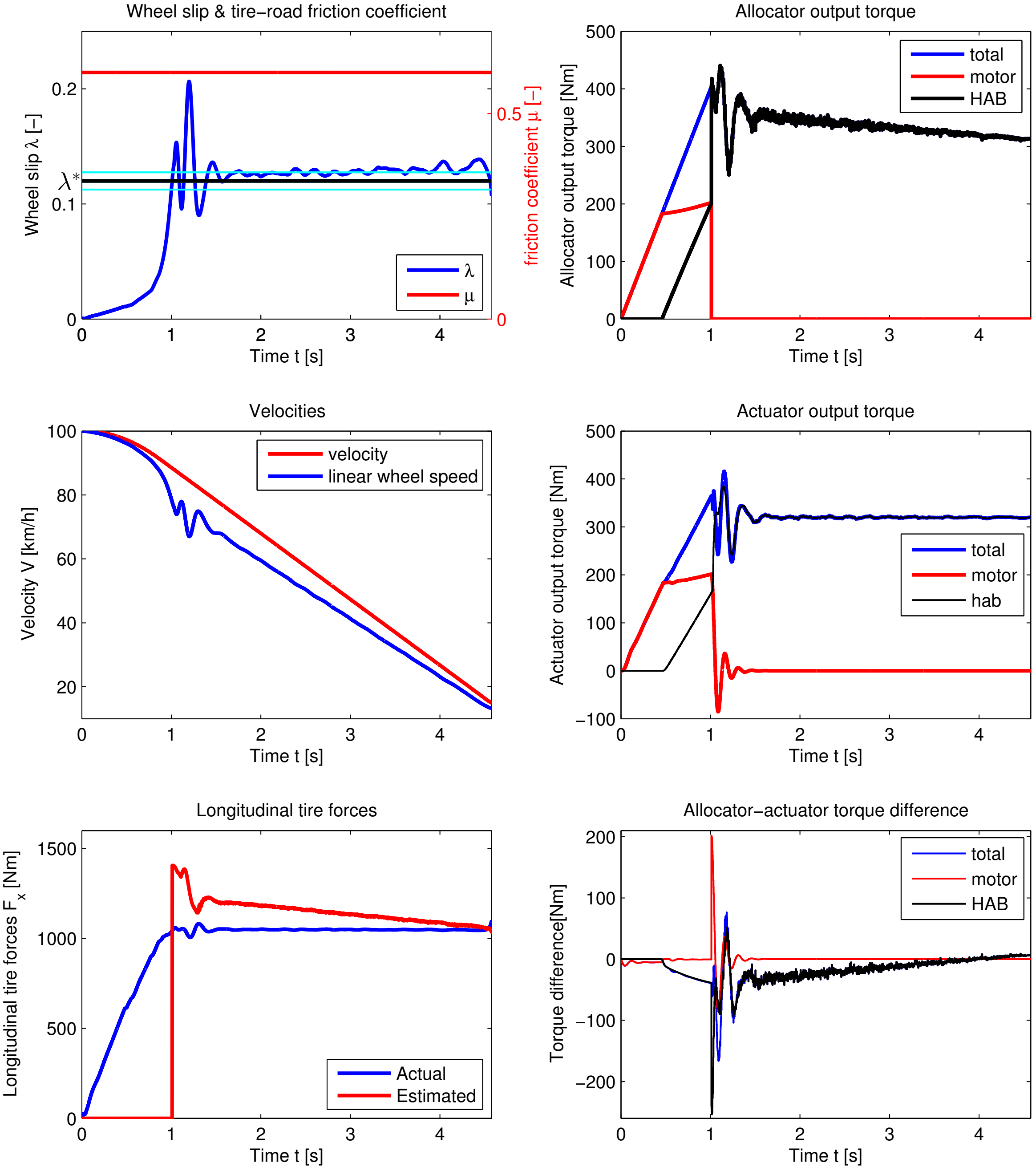

**Figure 5-2:** Braking on a wet asphalt track ($\mu_{\max} = 0.6$) using allocator strategy $\#1$

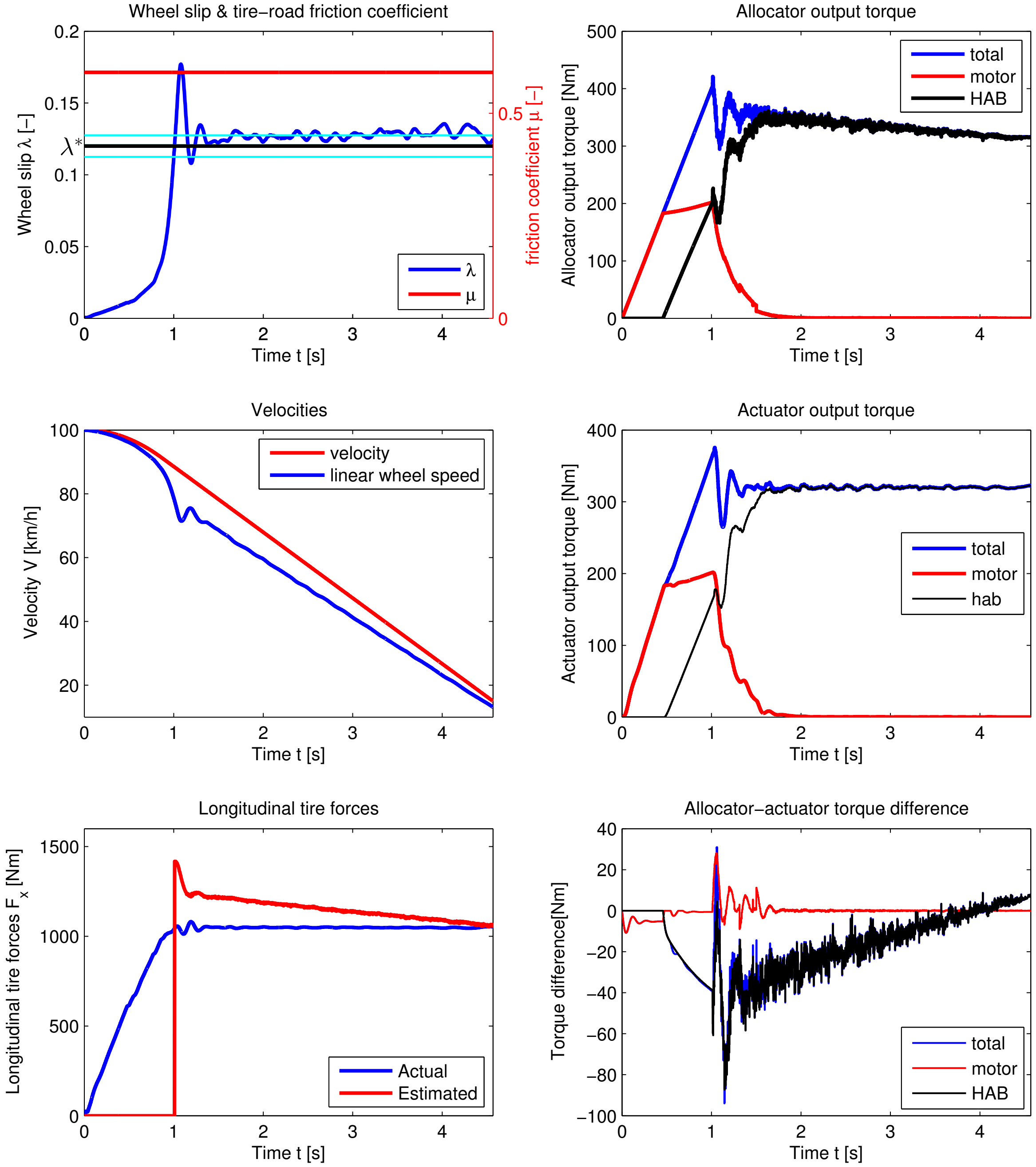

**Figure 5-3:** Braking on a wet asphalt track ($\mu_{\max} = 0.6$) using allocator strategy $\#2$

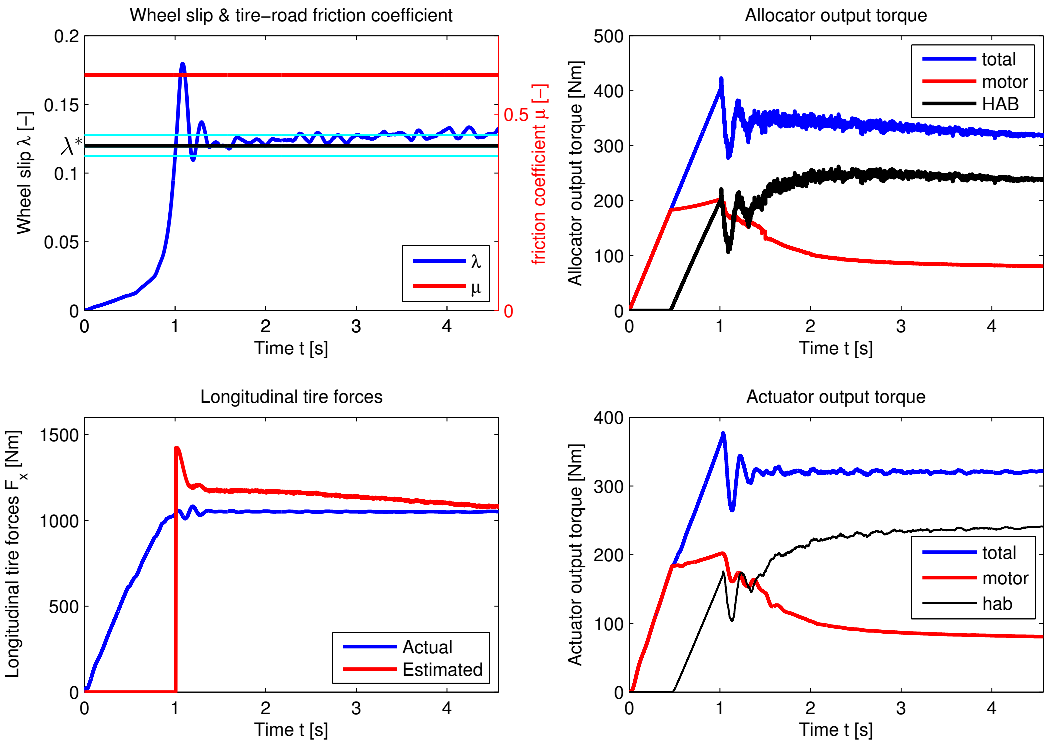

Figure 5-4: Braking on a wet asphalt track ($\mu_{\max} = 0.6$) using allocator strategy $\#3$

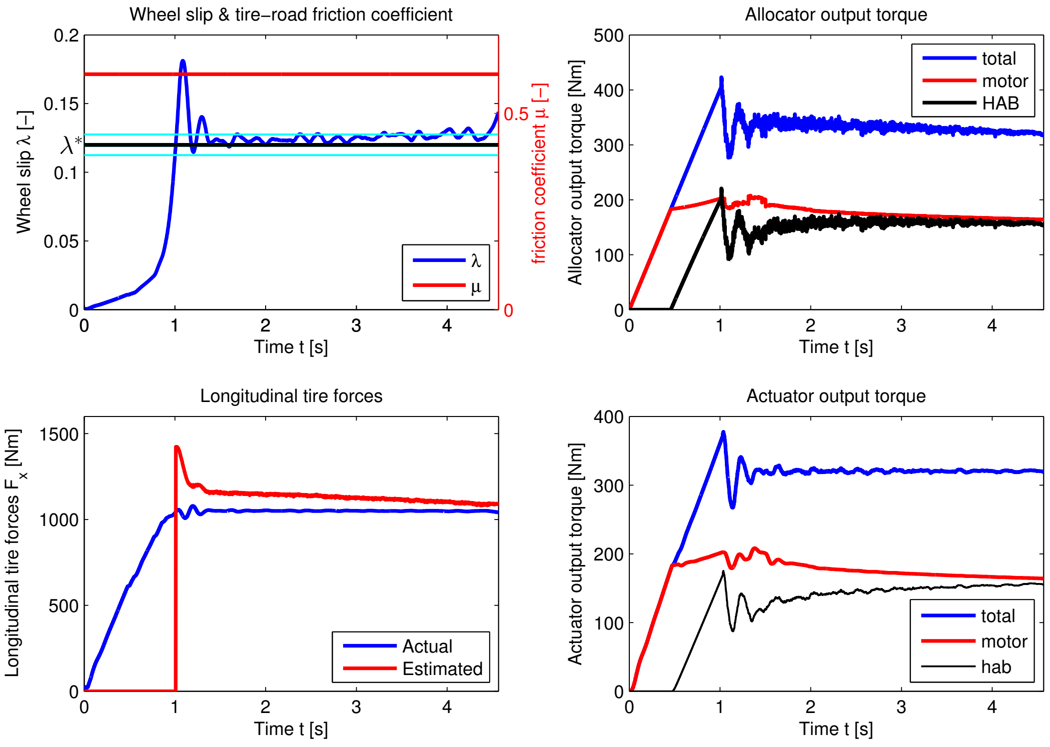

Figure 5-5: Braking on a wet asphalt track ($\mu_{\max} = 0.6$) using allocator strategy $\#4$

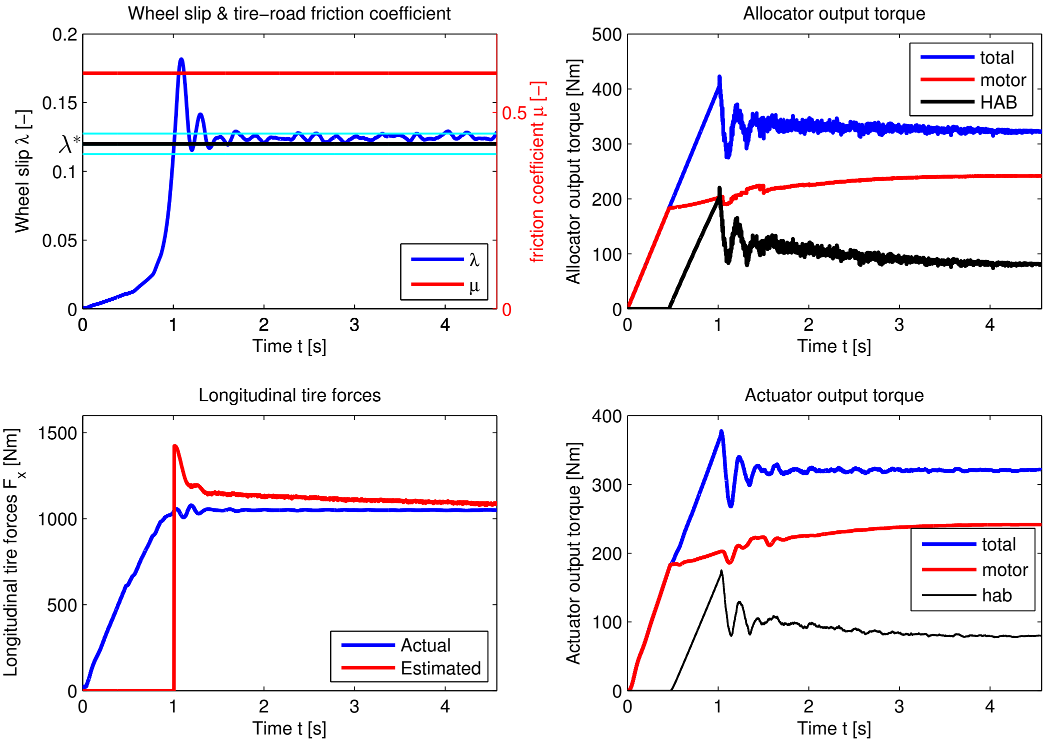

**Figure 5-6:** Braking on a wet asphalt track ($\mu_{\max} = 0.6$) using allocator strategy $\#5$

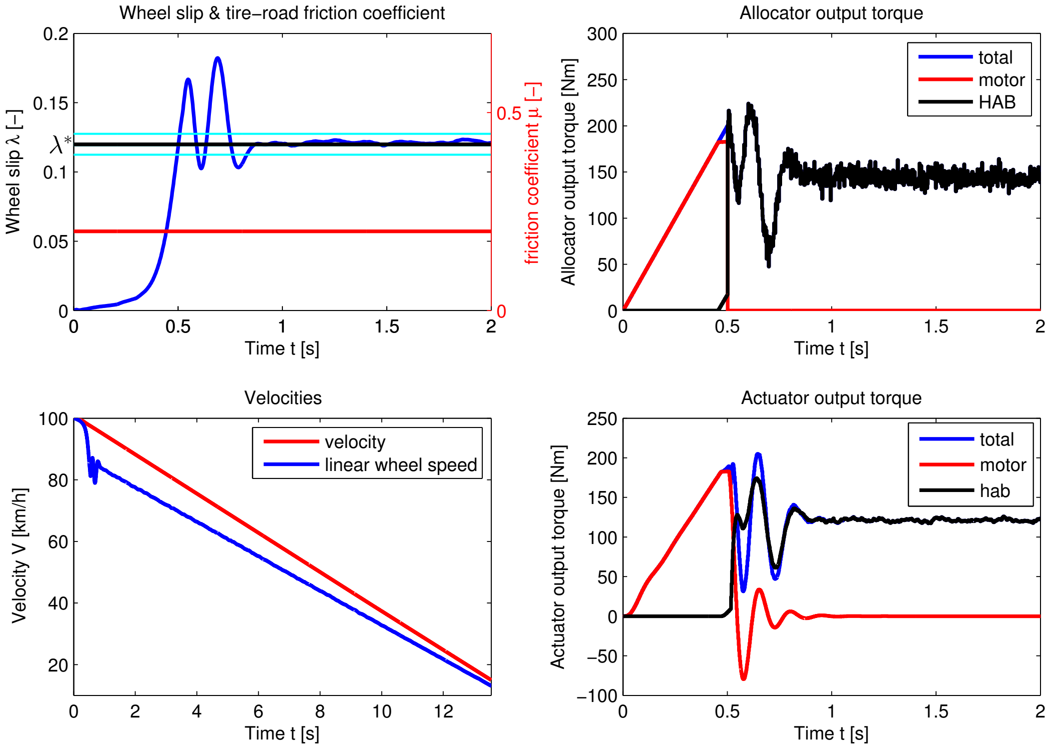

**Figure 5-7:** Braking on a snowy track ($\mu_{\max} = 0.2$) using allocator strategy $\#1$

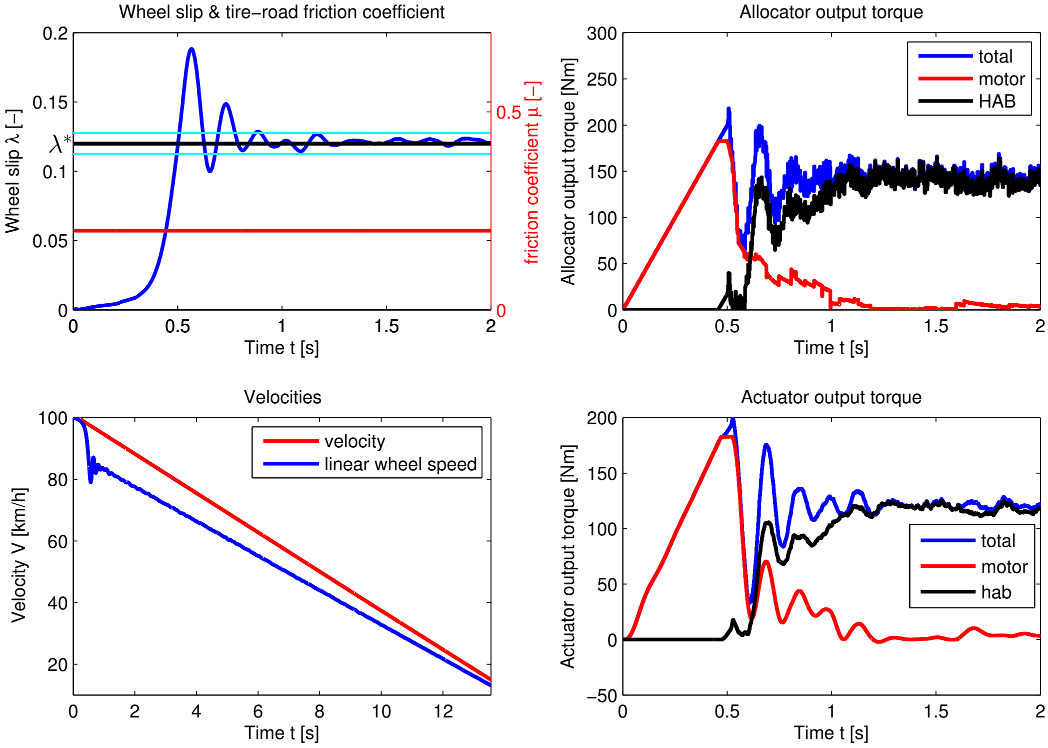

**Figure 5-8:** Braking on a snowy track ($\mu_{\max} = 0.2$) using allocator strategy $\#2$

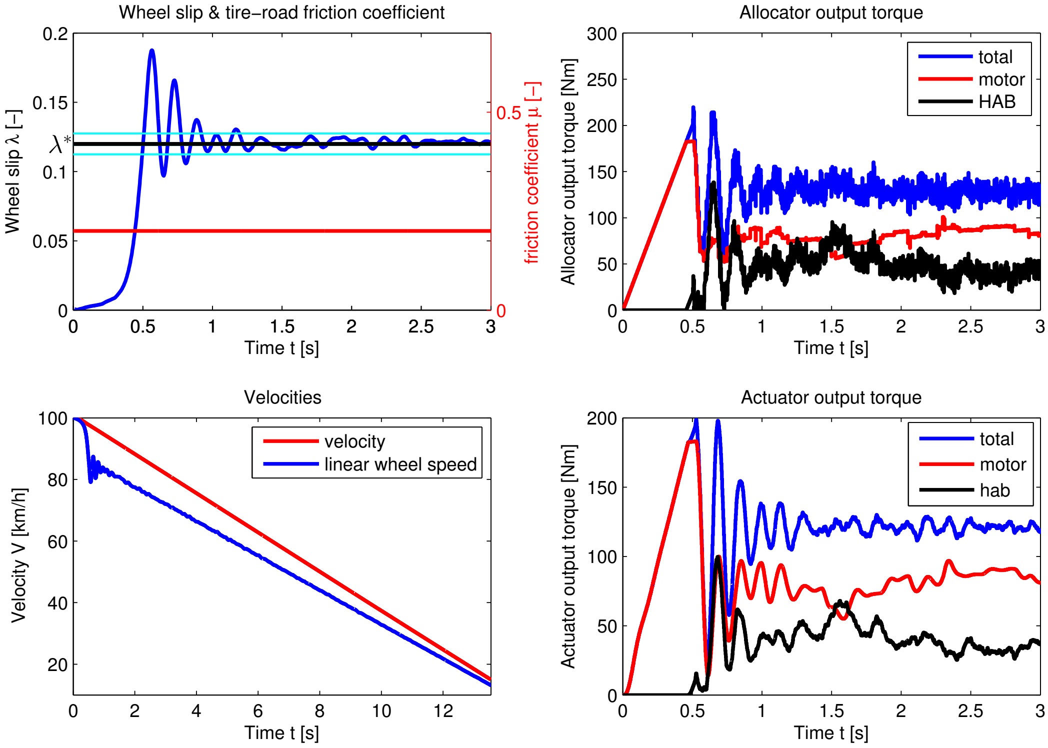

**Figure 5-9:** Braking on a snowy track ($\mu_{\max} = 0.2$) using allocator strategy $\#5$

### 5-2-3 $\mu$-jump Road Braking Maneuver

When we compare the RMS values of the slip error of the braking maneuver on a $\mu$-jump road (see table 5-1), we find that gradually shutting down the motor instead of immediately shutting down the motor yields a significant improved performance. Looking at the numbers in table 5-1, one could suggest that including the motor in the ABS using allocation strategy #3 is the best choice for this particular maneuver. However, the performance degrades rapidly when we increase the ratio of $\frac{T_m}{T_h}$ for the low frequency content of the control signal. Using allocation strategy #5 is even worse than an immediate shutdown of the motor.

The reason for this lies within the transient period. The braking maneuver starts on a wet asphalt track. At a certain point in time, the slip controller is activated and the controller output is distributed over the actuators. At the time the slip has converged to its setpoint, a change in road conditions occur. The track changes from a wet asphalt track into a snowy track with low friction. This results in a quick decrease of the controller output, which even becomes negative for a short time interval. For strategies #1 and #2 the only actuator active at this time is the hydraulic brake. It quickly reduces its torque without any overshoot, but it can never exert a negative torque (see figure 5-10 and 5-11).

For allocation strategies #3, #4 and #5 the motor is still being used during the $\mu$-jump and thus both the hydraulic brake and the motor inputs are decreased rapidly to zero. This introduces oscillations in the motor torque around $0\,[\mathrm{Nm}]$, making the motor torque negative at short periods of time. For allocation strategy #3 this negative overshoot results in a small controller/actuator error and good performance (figure 5-12). For strategies #4 and #5, the large oscillations in the motor torque result in poor tire force estimation and thus in poor feedback linearisation which in turn results in poor performance. The results of allocation strategy #5 are displayed in figure 5-13.

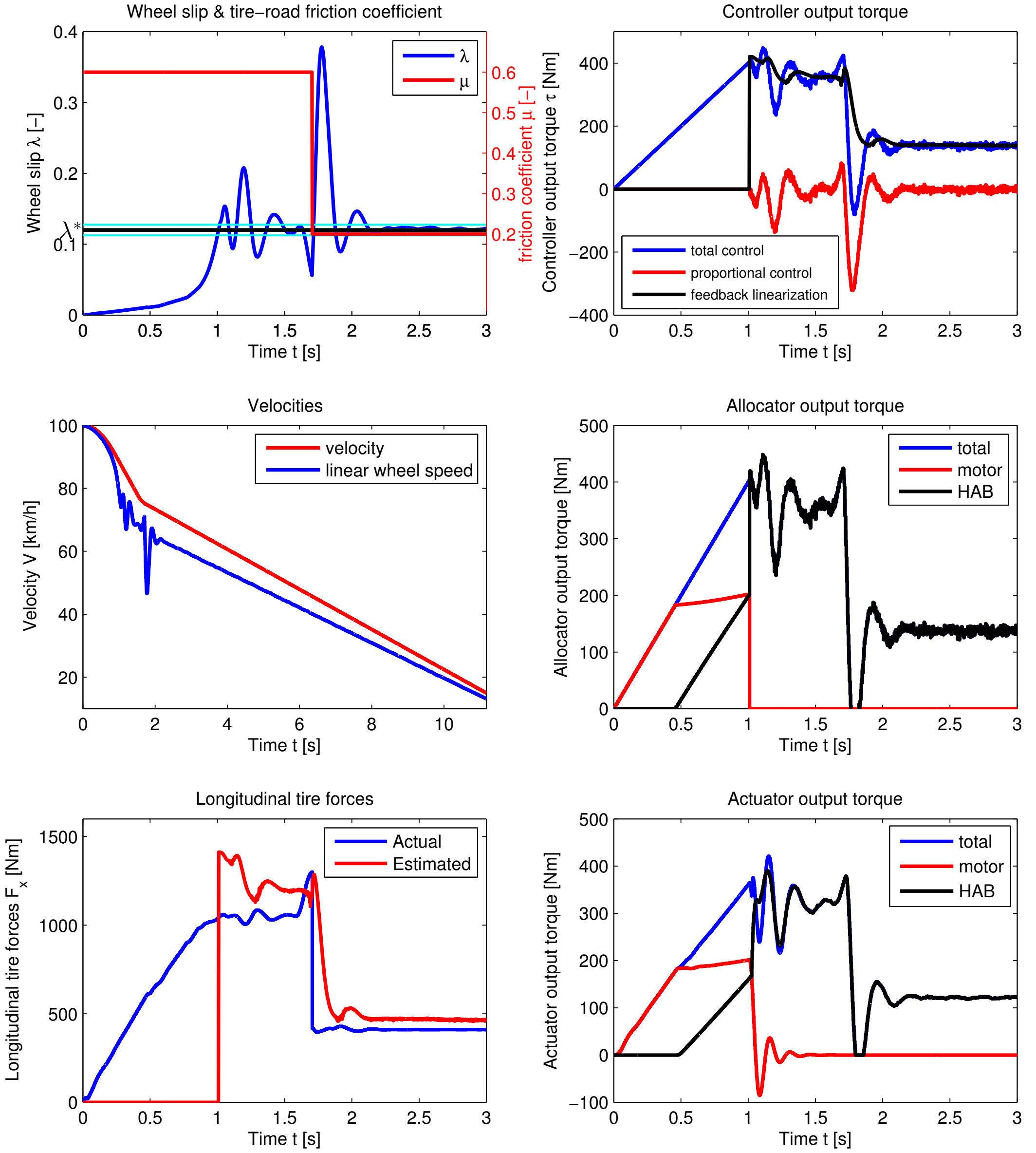

**Figure 5-10:** Braking on a $\mu$-jump track ($\mu_{\max} = 0.6 \rightarrow \mu_{\max} = 0.2$) using allocator strategy $\#1$

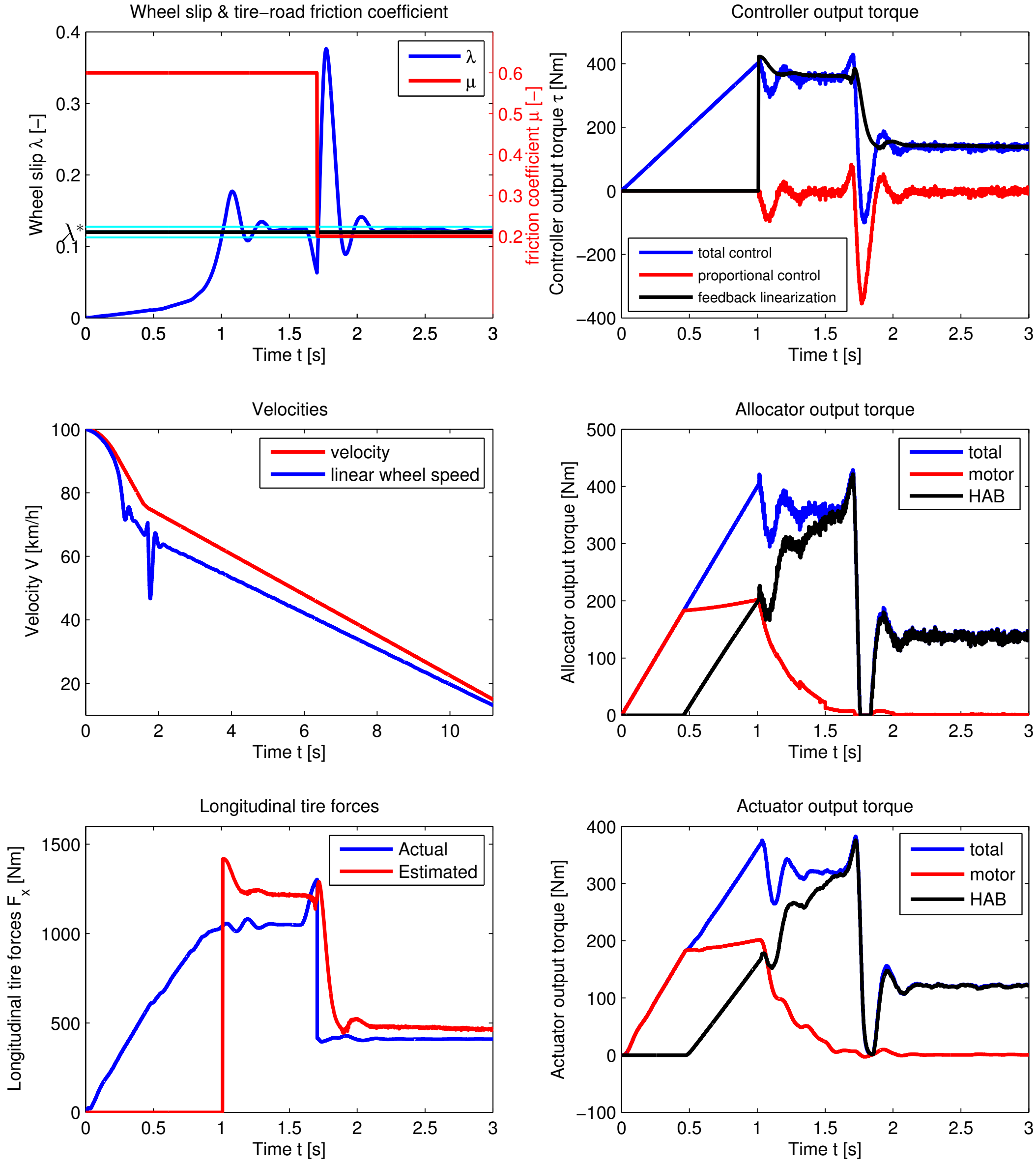

**Figure 5-11:** Braking on a $\mu$-jump track ($\mu_{\max} = 0.6 \rightarrow \mu_{\max} = 0.2$) using allocator strategy $\#2$

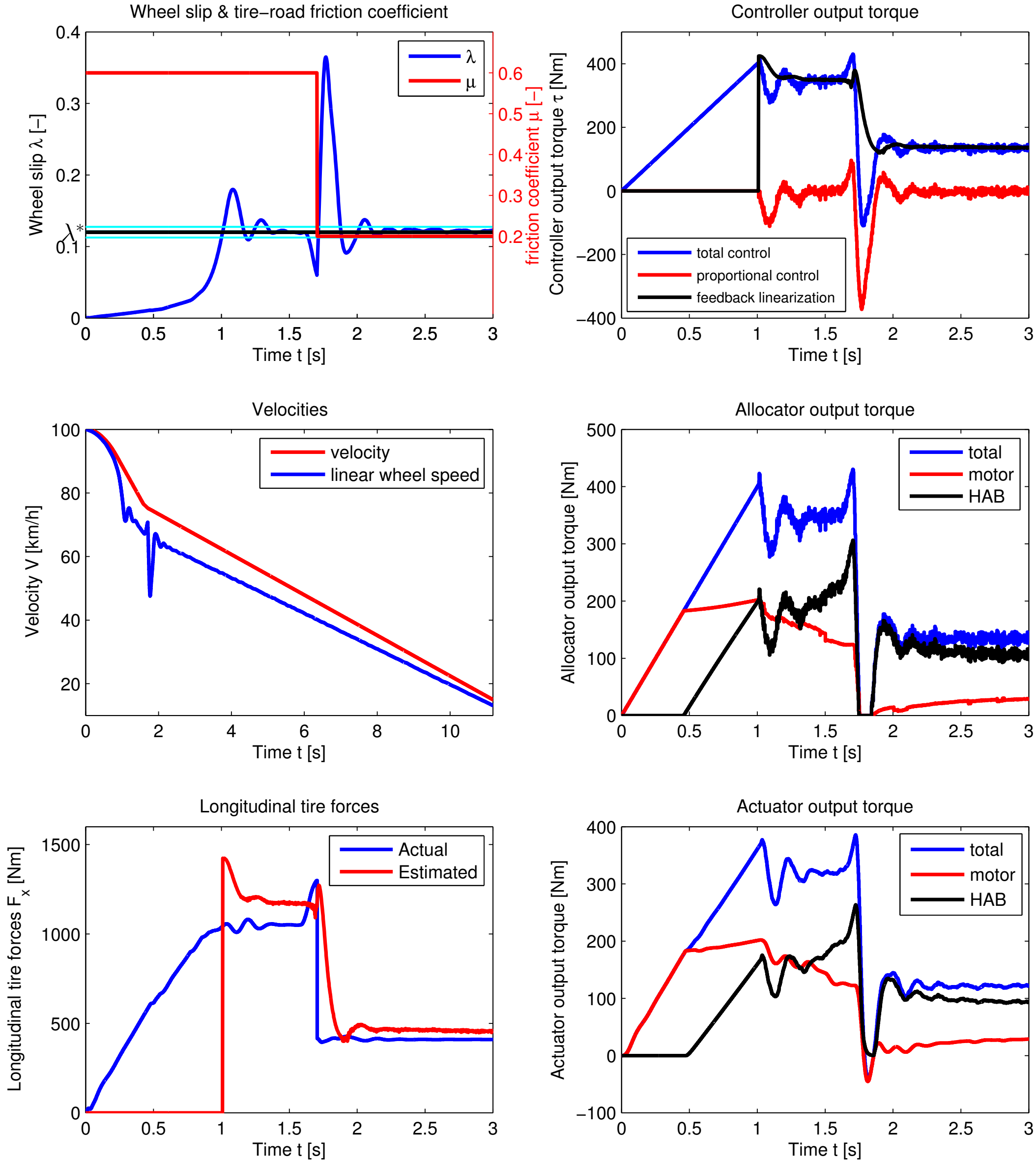

**Figure 5-12:** Braking on a $\mu$-jump track ($\mu_{\max} = 0.6 \to \mu_{\max} = 0.2$) using allocator strategy $\#3$

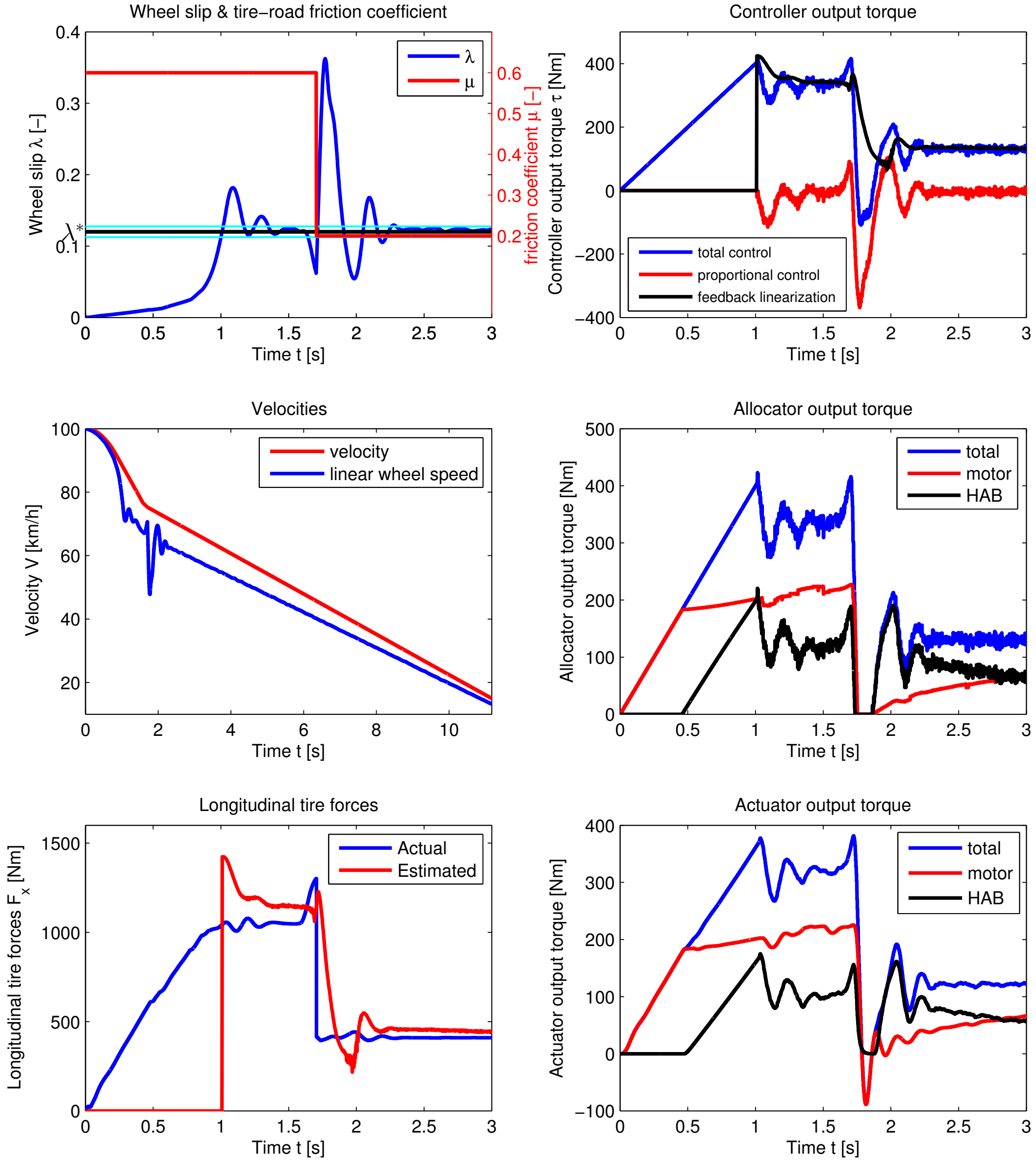

**Figure 5-13:** Braking on a $\mu$-jump track ($\mu_{\max} = 0.6 \rightarrow \mu_{\max} = 0.2$) using allocator strategy $\#5$

## 5-3 Conclusions

When we were braking on wet asphalt, incorporating the motor into the ABS algorithm improved the performance. Despite the fact that the transient performance when incorporating the motor was less good than when you gradually shut down the motor, the improved performance due to better tire force estimation outweighed this.

The performance improvement due to better tire force estimation on the snowy road and $\mu$-jump track was less significant as the improvement on the wet asphalt track. Incorporating the motor in the ABS algorithm did degrade the transient performance significantly on the snowy road and in most cases also on the $\mu$-jump track. On these surfaces the motor and driveline dynamics are excited by a high frequency control signal, resulting in oscillations and bad performance. On the $\mu$-jump track the oscillations that occurred using strategy #3 were accidentally beneficial, but when the road conditions vary only a little bit this will probably no longer be the case.

From this analysis we find that incorporating the motor into the ABS algorithm for braking maneuvers on relatively high friction surfaces ($\mu_{\max} \geq 0.6$) improves the performance marginally. However, for braking maneuvers on low friction surfaces the gain in performance diminishes and incorporating the motor into the ABS can even result in worse performance. This poses a problem since especially on these surfaces a driver is more likely to trigger the ABS.

Based on these results we think gradually shutting down the motor while entering an emergency braking maneuver is the best control allocation strategy.

# Chapter 6

# Conclusions

In this final chapter, the most important conclusions drawn in this work will be summarized. We will end this chapter with some recommendations for future work.

In chapter 2 we started by presenting control oriented models of the braking dynamics and tire-road contact forces. We also introduced a second order model of the electric motor and driveline and a first order model of a Hydraulic Actuated Brake (HAB) which was found in literature. We extended this model with an output uncertainty model to account for the uncertainty of the friction coefficient $\nu$ between the braking pad and disc.

We briefly discussed the advantage of wheel slip control over wheel deceleration control in chapter 3. Subsequently we presented a robust adaptive wheel slip controller which is able to identify the road conditions online and adapt whenever changes in road conditions occur. We improved the stability of the controller for low velocities by improving the update law. An extensive theoretical derivation of this update law was included.

The problem of control allocation was discussed in chapter 4. A dynamic allocation method based on the concept of sequential quadratic programming (SQP) was introduced and a numerically efficient solver was presented. Finally, the allocation weights for five allocation strategies were chosen based on the different properties of the actuators.

In chapter 5 the results of three different braking maneuvers in combination with five different control allocation strategies were presented. Shutting down the motor gradually when entering an emergency situation seems to be the best control allocation strategy. By incorporating the electric motor in the ABS algorithm we risk exciting the motor and driveline dynamics with a high frequency control signal when we are driving for example on a low friction road, which results in poor slip control performance.

## 6-1 Recommendations and Future Work

Although this work presented some initial findings on the topic of incorporating an electric motor into an Anti-lock Braking System (ABS) algorithm for certain hybrid vehicles nowadays on the market, there are still some matters which can be improved and/or investigated:

For verification purposes, it would be useful to have more detailed models of the hydraulic brakes and motor and driveline dynamics. In this work we used control-oriented models for both design and simulation purposes.

We restricted the scope of this work to braking on a symmetric road. This is an assumption that in reality is often invalid. In that case the allocation problem in chapter 4 can no longer be simplified by replacing equation (4-11) by equation (4-12) and only considering the torque allocation for a single rear wheel. The control allocator has to be extended to be able to cope with two controller outputs and three actuators.

In this work we compared the different allocation strategies using the same ABS controller. It would be interesting to test these allocation strategies on other types of controller to see how the performance of those controllers will be influenced.

# Appendix A

# Parameters

**Table A-1:** Burckhardt parameters for different road conditions

| road condition | $v_{r1}$ | $v_{r2}$ | $v_{r3}$ |
|---|---|---|---|
| dry asphalt | 1.28 | 23.99 | 0.52 |
| wet asphalt | 0.857 | 33.822 | 0.347 |
| cobblestone | 1.37 | 6.46 | 0.67 |
| snow | 0.19 | 94.13 | 0.06 |

**Table A-2:** Tuning parameters of the controller

| parameter | strategy #1 | strategy #2 | strategy #3 | strategy #4 | strategy #5 |
|---|---|---|---|---|---|
| $k_{\text{front}}$ | 133.2 | 133.2 | 133.2 | 133.2 | 133.2 |
| $\gamma_{\text{front}}$ | 480 | 480 | 480 | 480 | 480 |
| $\epsilon_{\text{front}}$ | 0.0075 | 0.0075 | 0.0075 | 0.0075 | 0.0075 |
| $k_{\text{rear}}$ | 59.2 | 65.12 | 71.04 | 71.04 | 71.04 |
| $\gamma_{\text{rear}}$ | 440 | 440 | 480 | 440 | 440 |
| $\epsilon_{\text{rear}}$ | 0.0075 | 0.0075 | 0.0075 | 0.0075 | 0.0075 |

## Appendix B

# Additional Plots of Braking Maneuvers

In this appendix additional plots are shown corresponding to the braking maneuvers carried out in chapter 5.

Some explanation on the definition of 'allocator states' is in order here. The allocator states represent the point in the algorithm where the output of the allocator is determined. See table B-1 for more information.

**Table B-1:** Explanation of the allocator states.

| allocator state | $T_m$ | $T_h$ |
|---:|:---:|:---:|
| 1.00 | $\overline{T_m}$ | $\overline{T_h}$ |
| 1.50 | $\underline{T_m}$ | $\underline{T_h}$ |
| 2.00 | $T_m^u$ | $T_h^u$ |
| 3.00 | $\overline{T_m}$ | $Tb - \overline{T_m}$ |
| 3.25 | $\underline{T_m}$ | $Tb - \underline{T_m}$ |
| 3.50 | $Tb - \overline{T_h}$ | $\overline{T_h}$ |
| 3.75 | $Tb - \underline{T_h}$ | $\underline{T_h}$ |

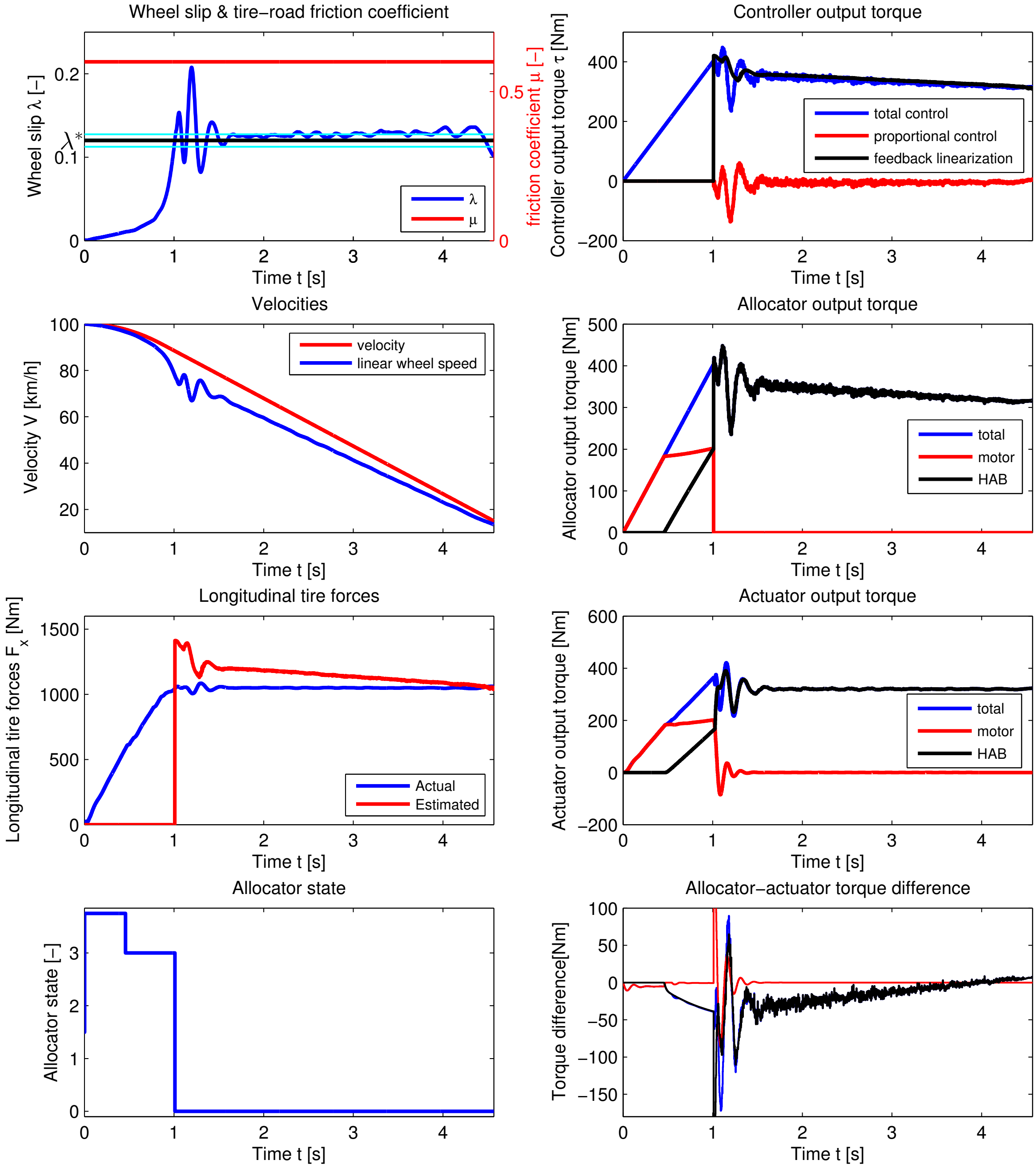

**Figure B-1:** Braking on a wet asphalt track ($\mu_{\max} = 0.6$) using allocator strategy $\#1$

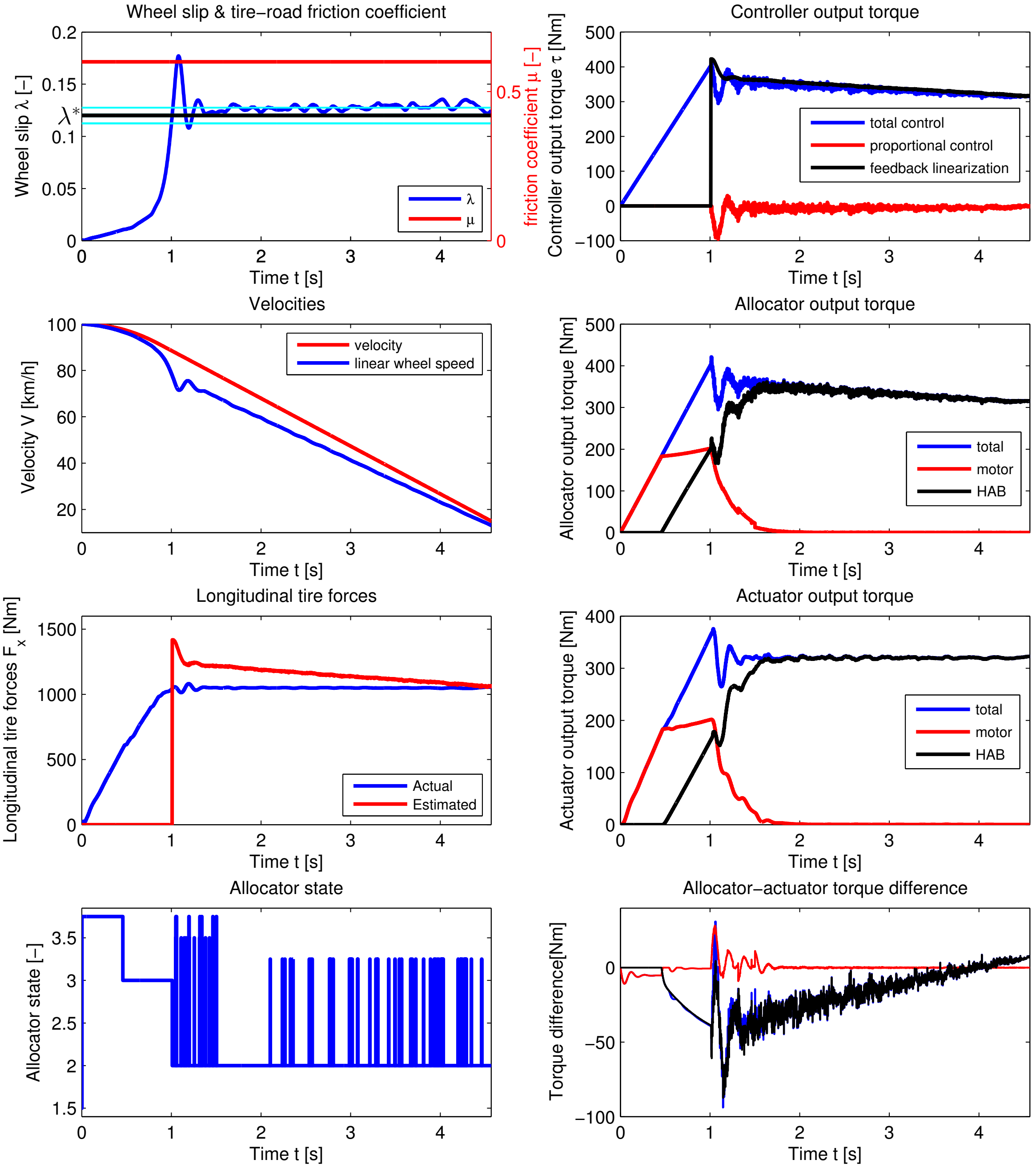

**Figure B-2:** Braking on a wet asphalt track ($\mu_{\max} = 0.6$) using allocator strategy $\#2$

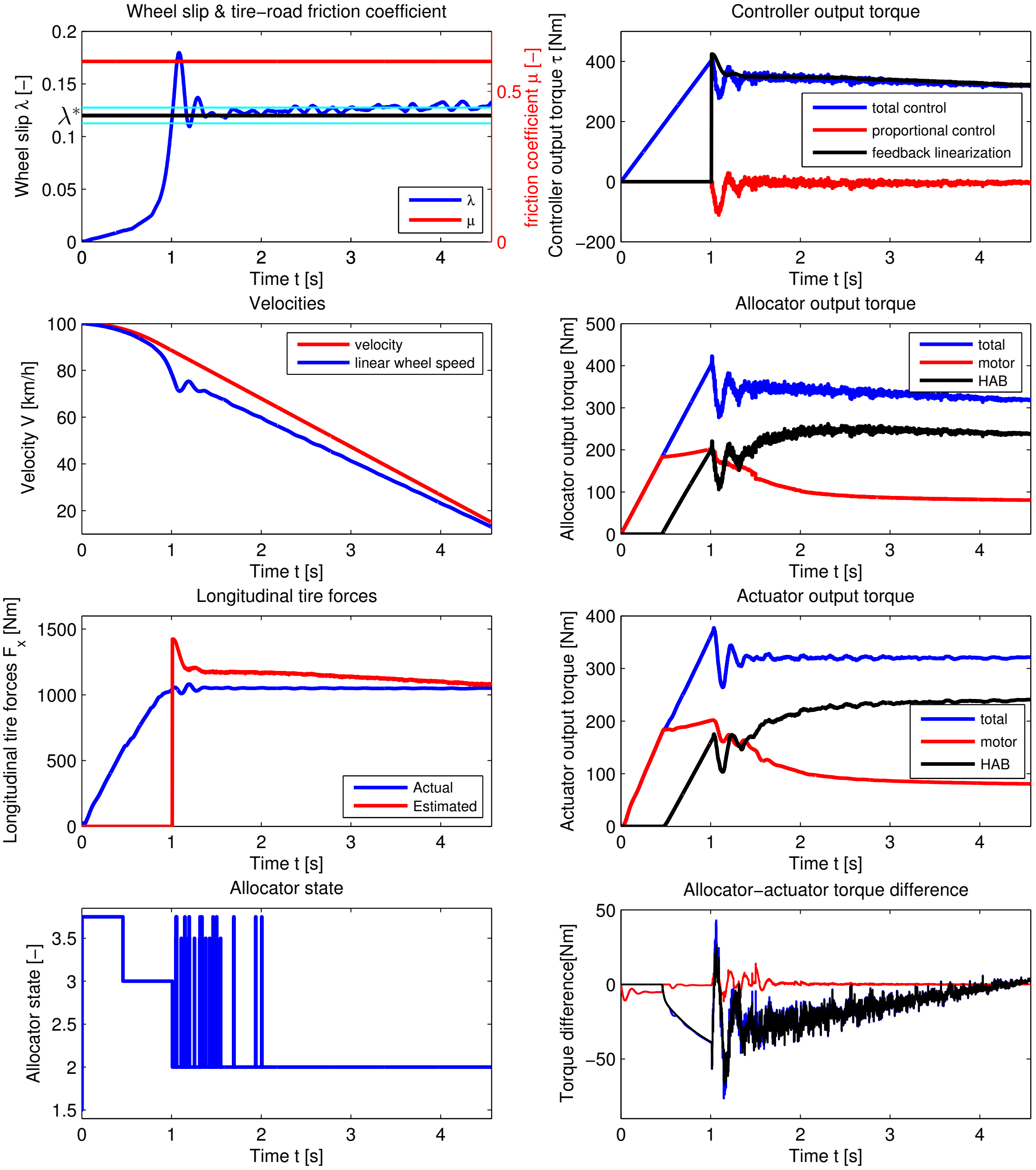

**Figure B-3:** Braking on a wet asphalt track ($\mu_{\max} = 0.6$) using allocator strategy $\#3$

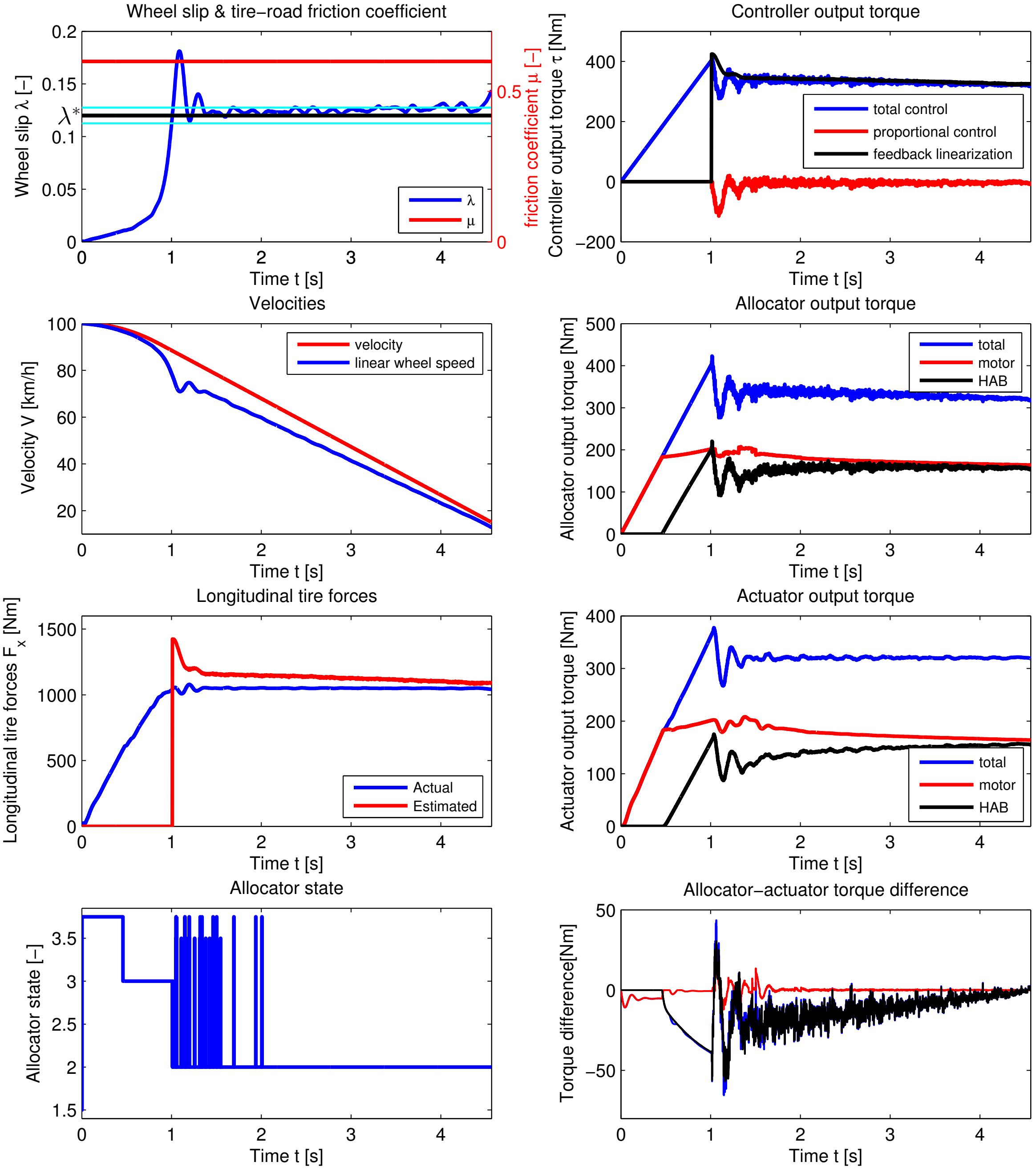

**Figure B-4:** Braking on a wet asphalt track ($\mu_{\max} = 0.6$) using allocator strategy $\#4$

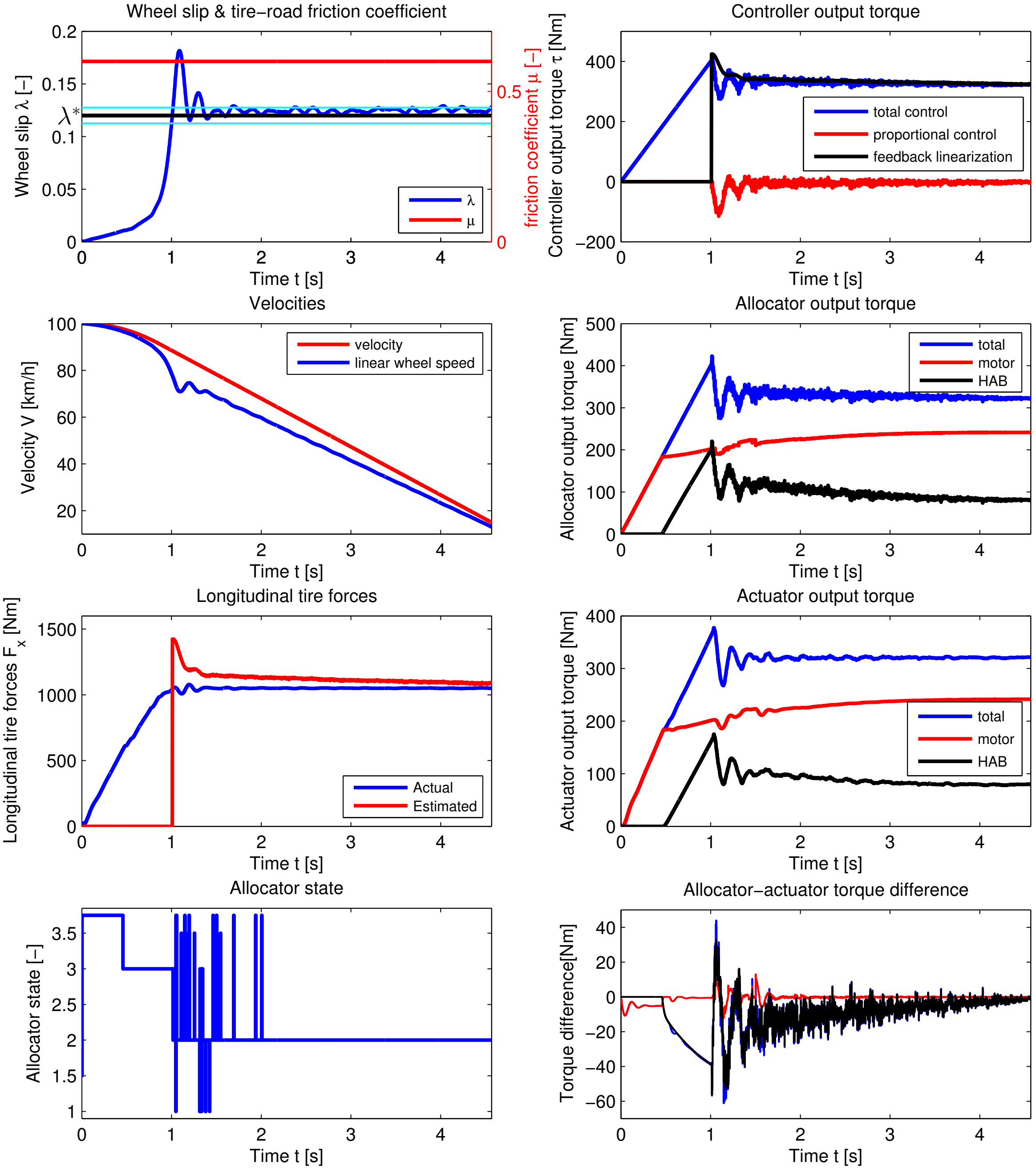

**Figure B-5:** Braking on a wet asphalt track ($\mu_{\max} = 0.6$) using allocator strategy $\#5$

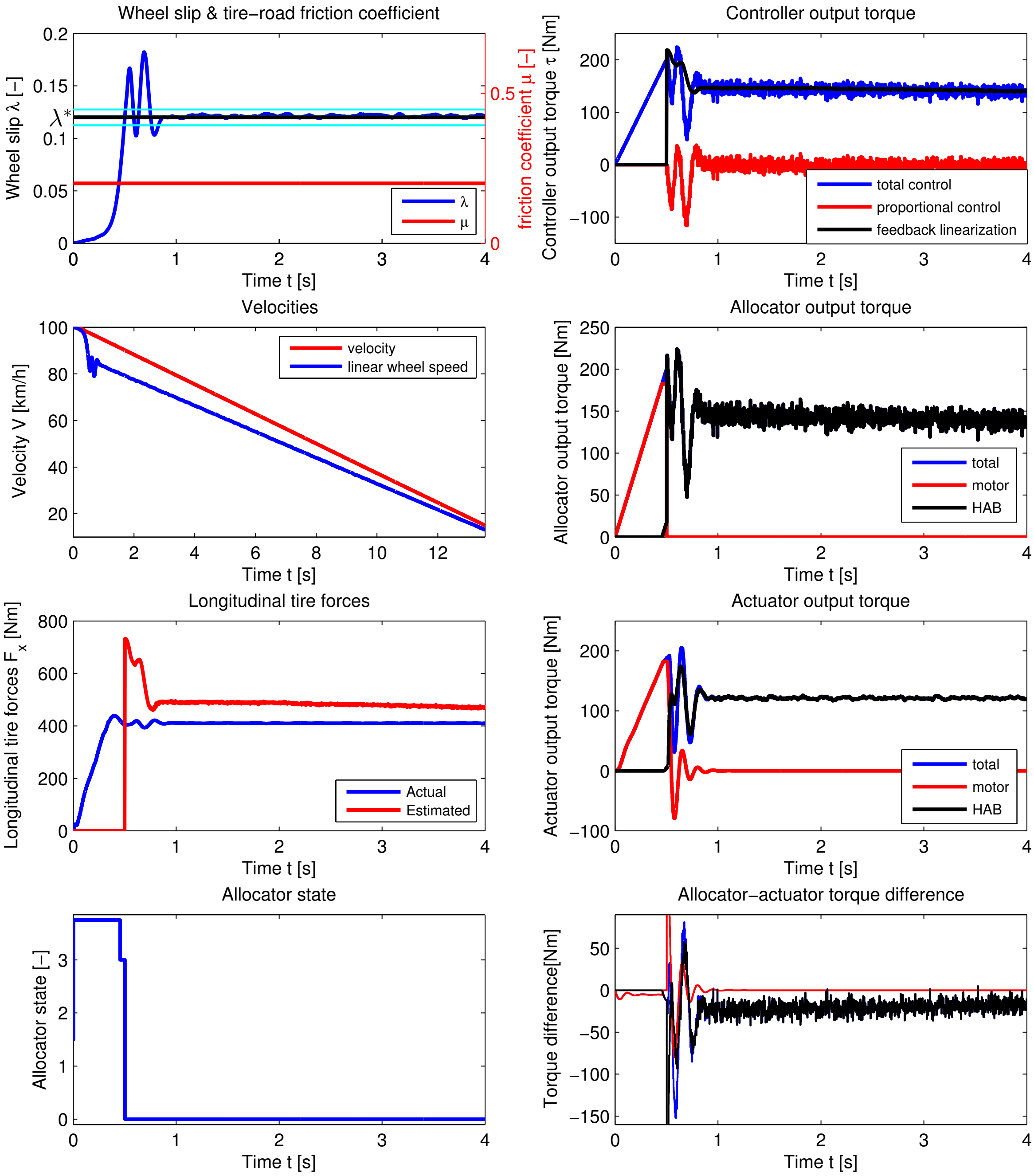

**Figure B-6:** Braking on a snow track ($\mu_{\max} = 0.2$) using allocator strategy $\#1$

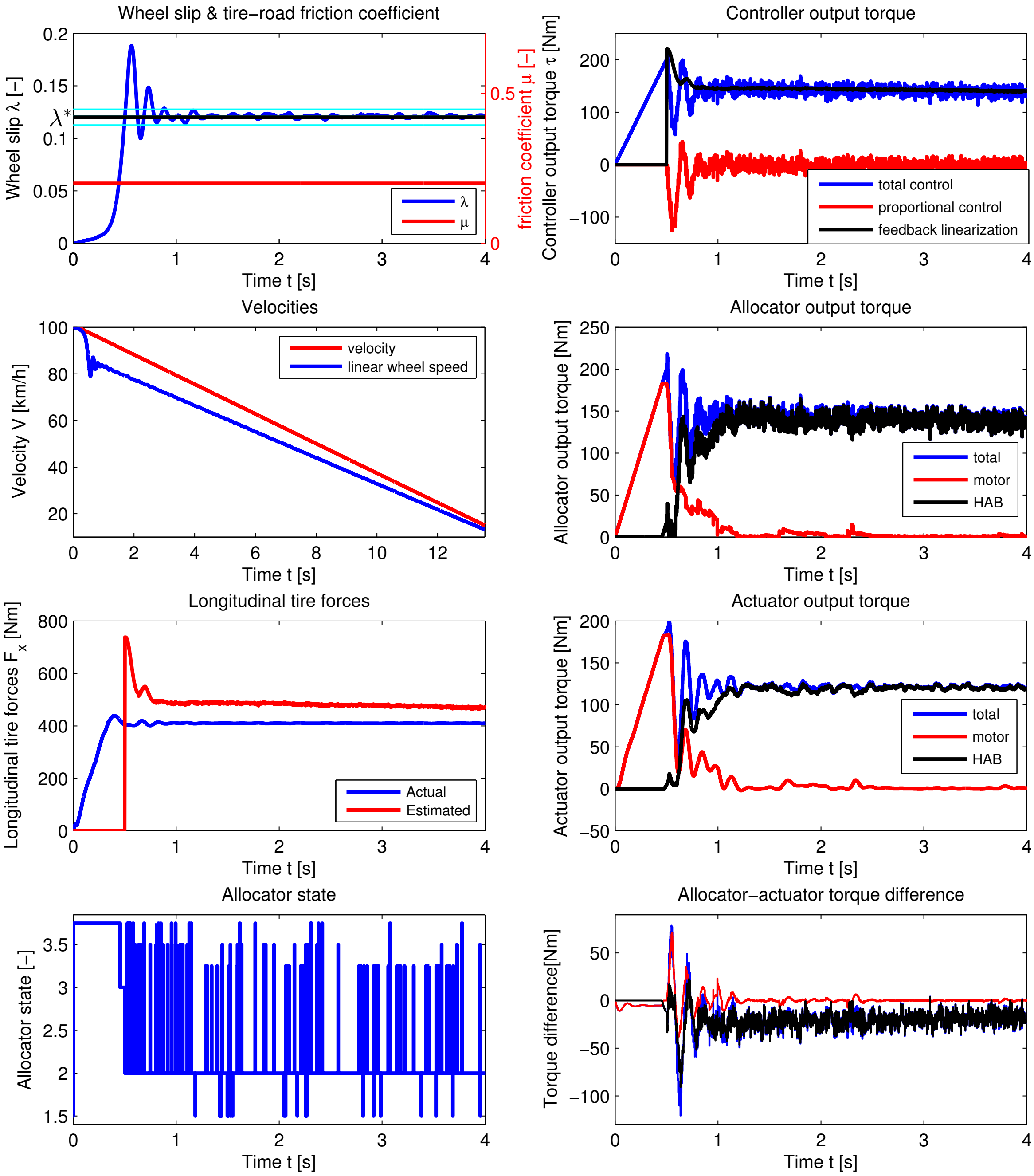

**Figure B-7:** Braking on a snow track ($\mu_{\max} = 0.2$) using allocator strategy $\#2$

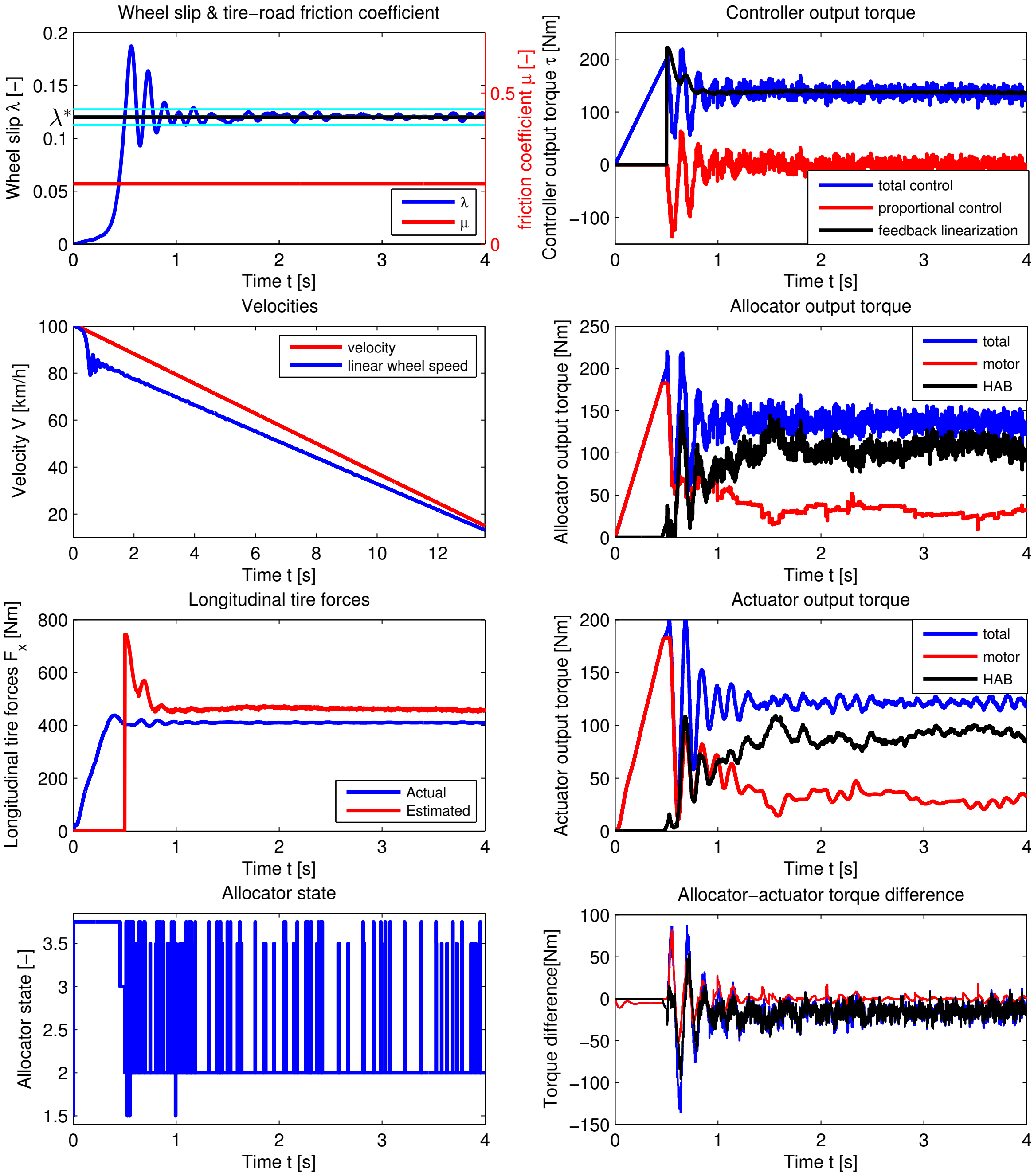

**Figure B-8:** Braking on a snow track ($\mu_{\max} = 0.2$) using allocator strategy $\#3$

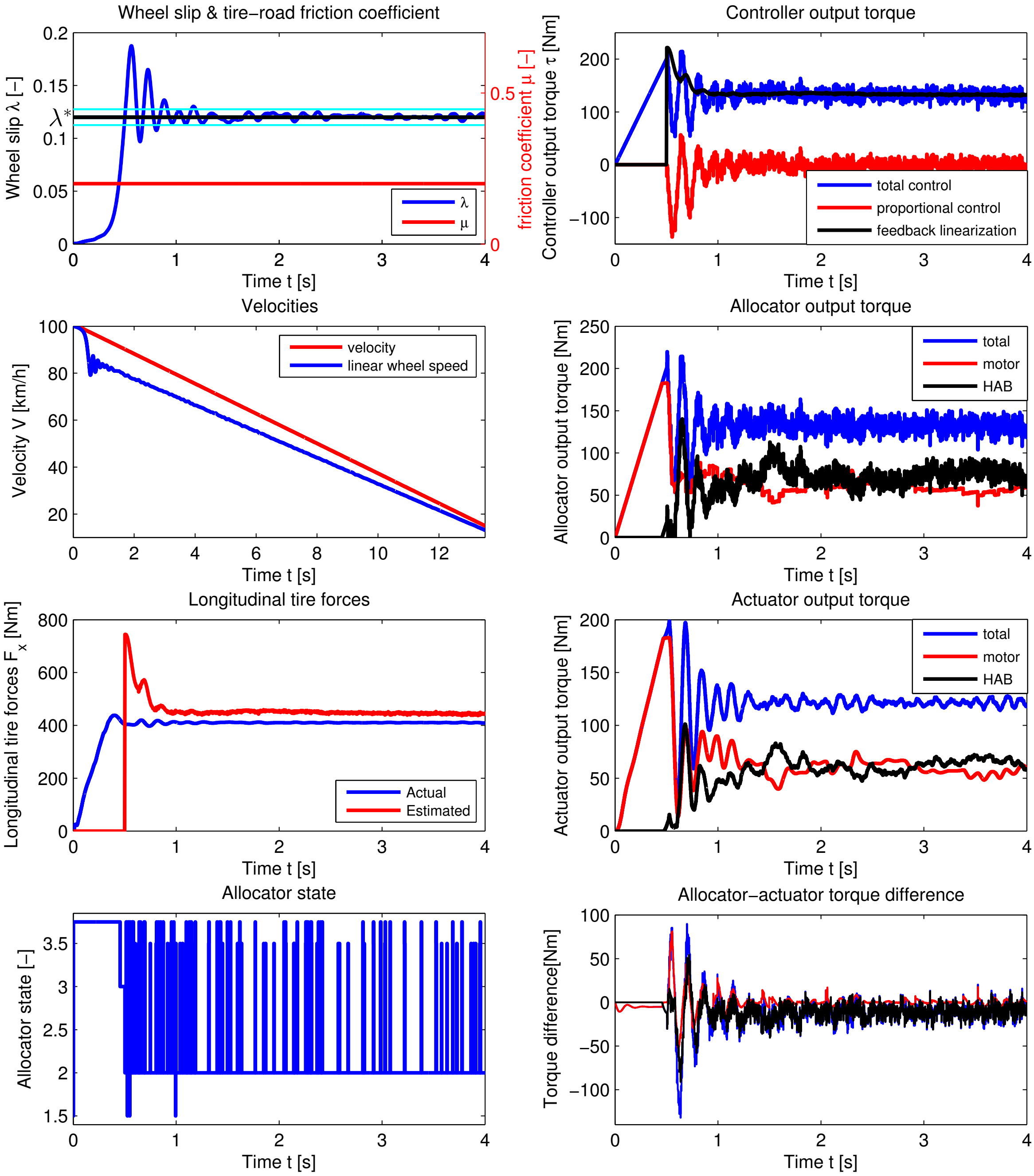

**Figure B-9:** Braking on a snow track ($\mu_{\max} = 0.2$) using allocator strategy $\#4$

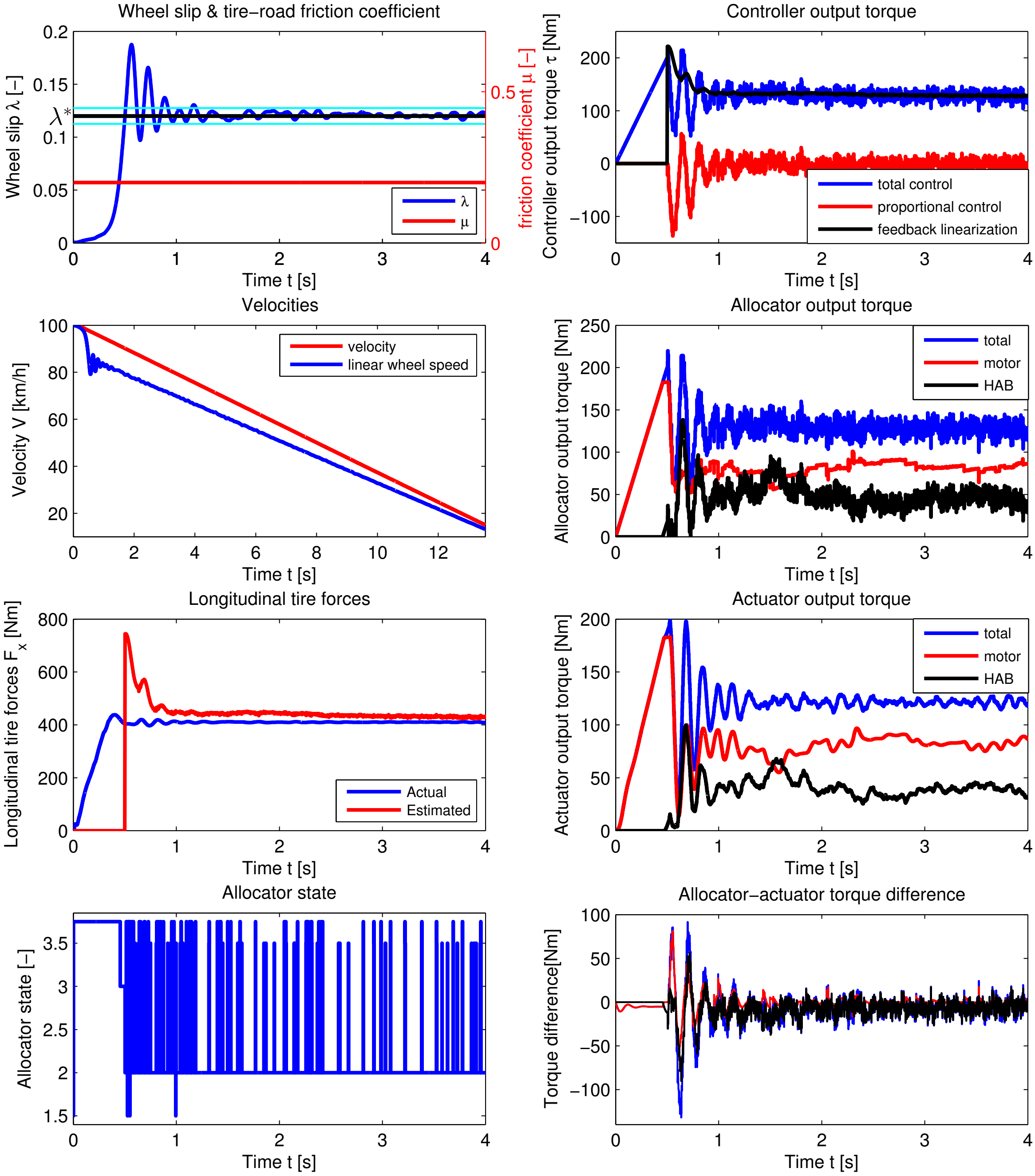

**Figure B-10:** Braking on a snow track ($\mu_{\max} = 0.2$) using allocator strategy $\#5$

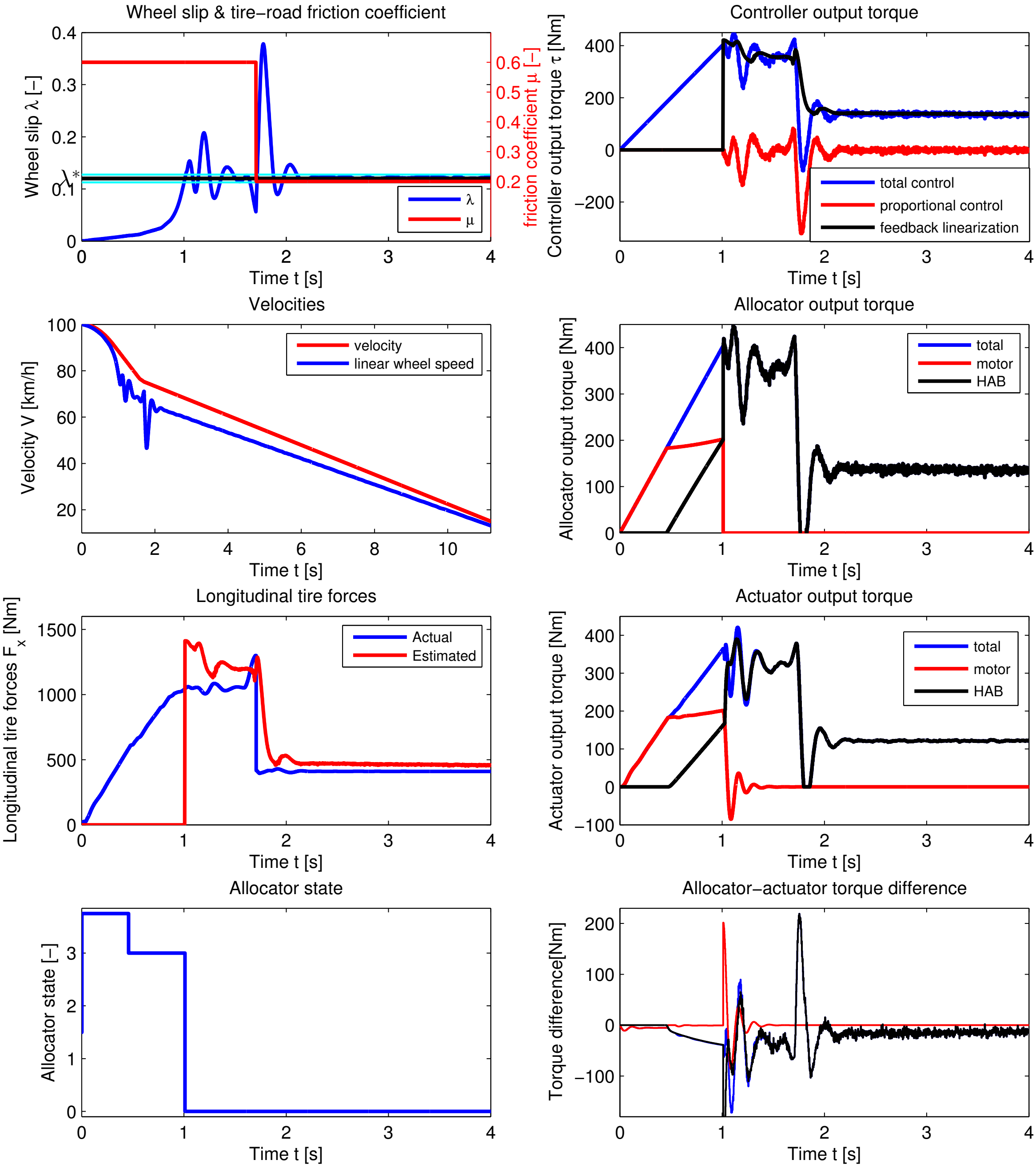

**Figure B-11:** Braking on a $\mu$-jump track ($\mu_{\max} = 0.6 \rightarrow \mu_{\max} = 0.2$) using allocator strategy $\#1$

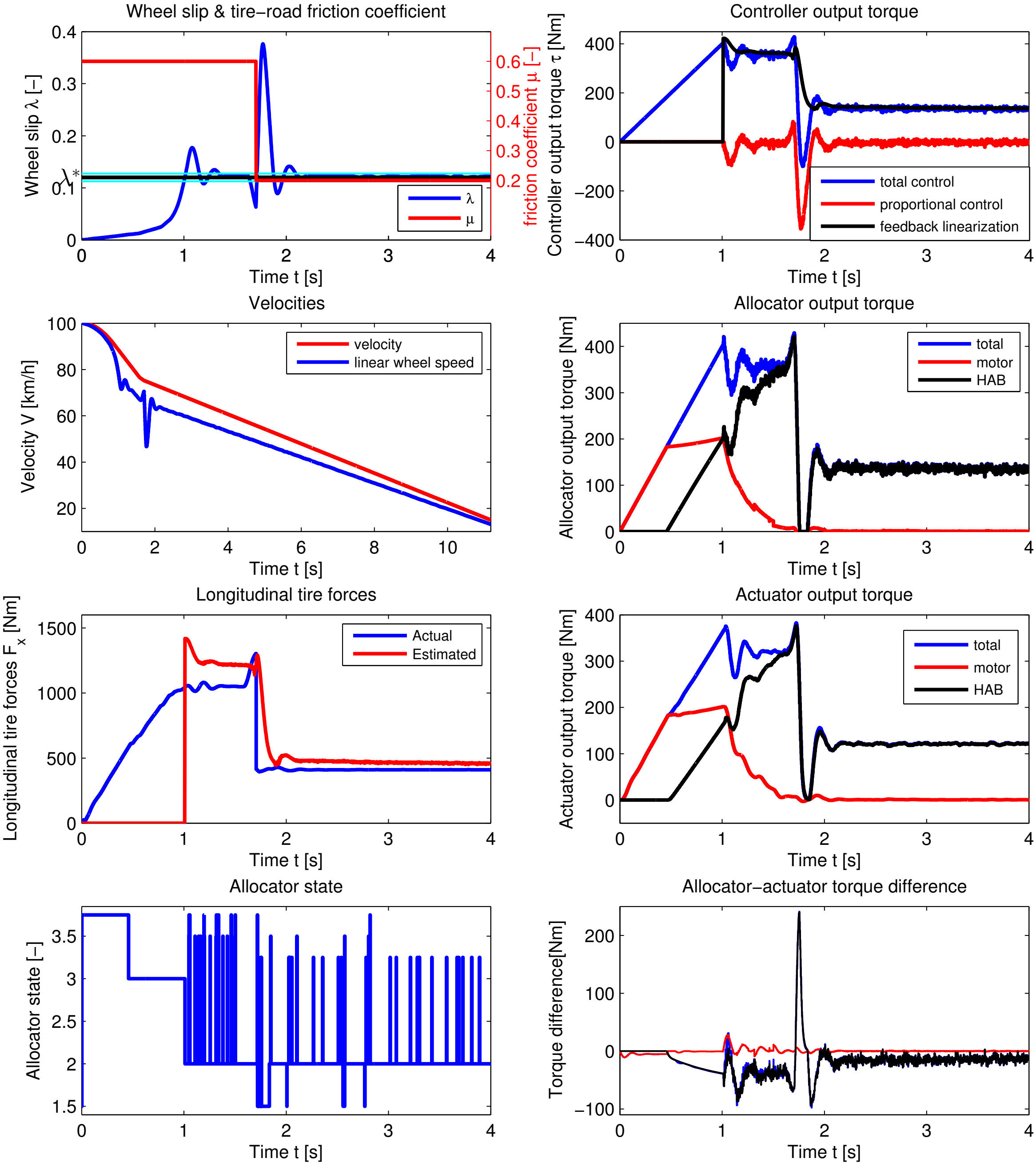

**Figure B-12:** Braking on a $\mu$-jump track ($\mu_{\max} = 0.6 \rightarrow \mu_{\max} = 0.2$) using allocator strategy #2

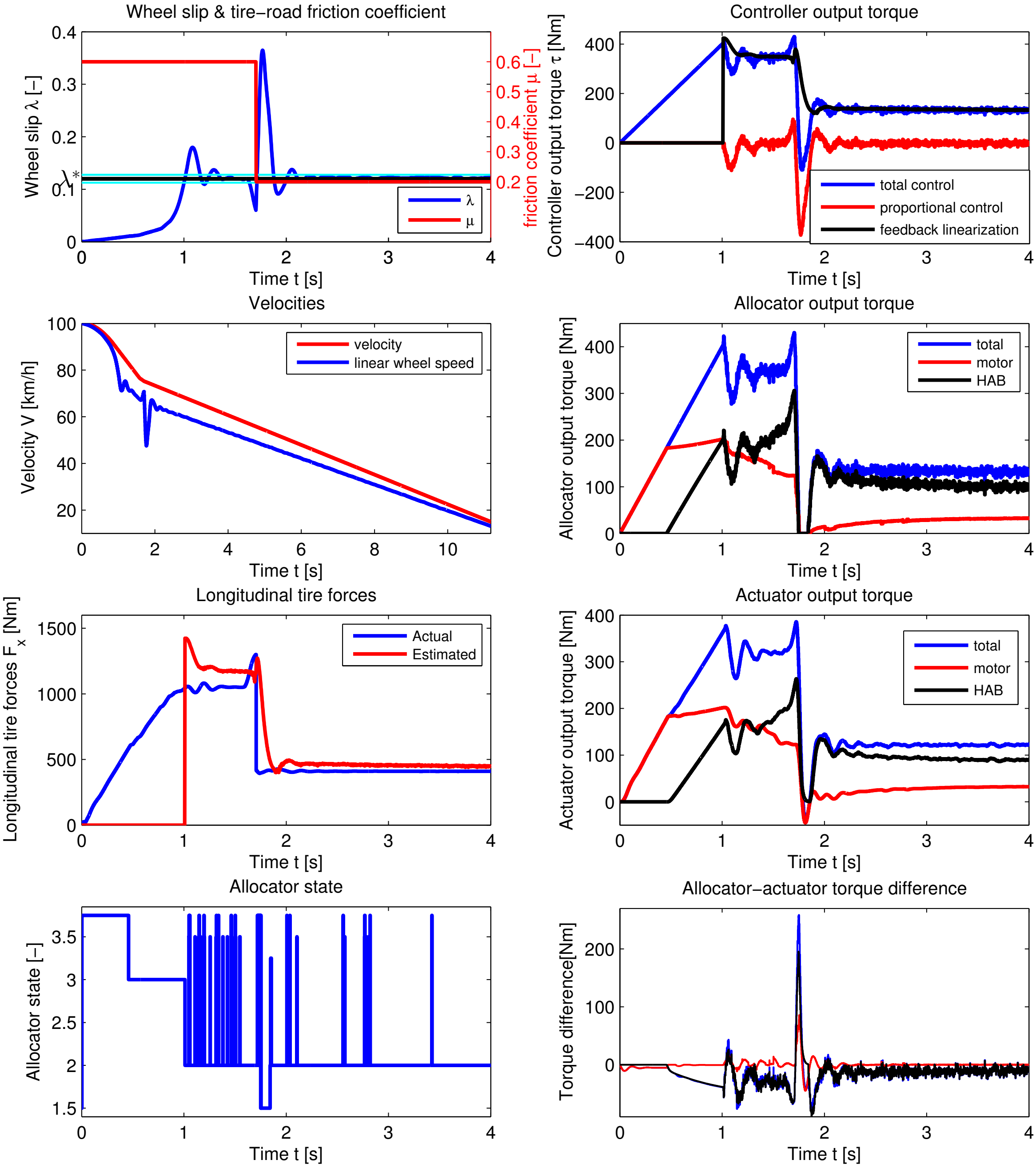

**Figure B-13:** Braking on a $\mu$-jump track ($\mu_{\max} = 0.6 \rightarrow \mu_{\max} = 0.2$) using allocator strategy #3

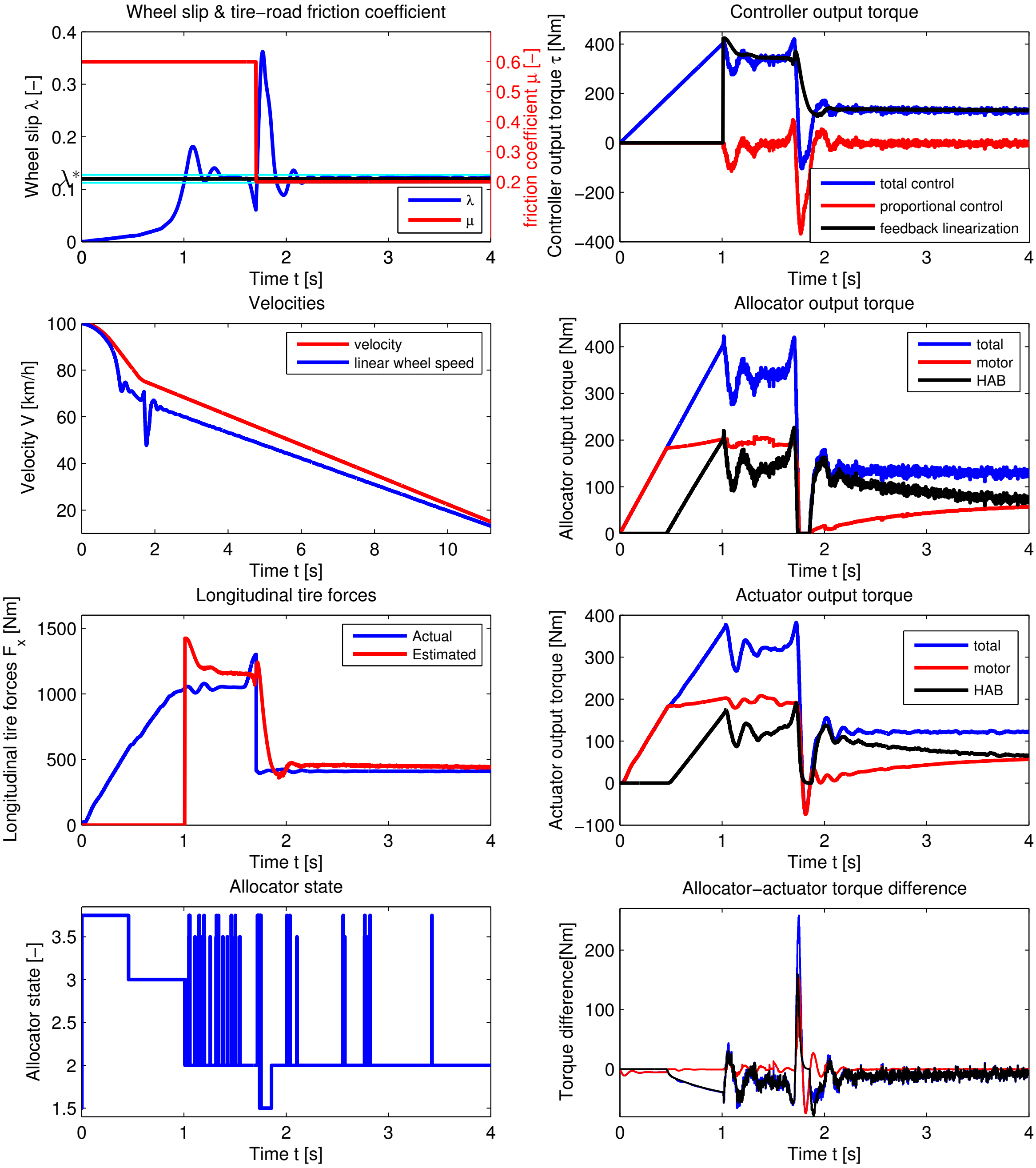

**Figure B-14:** Braking on a $\mu$-jump track ($\mu_{\max} = 0.6 \rightarrow \mu_{\max} = 0.2$) using allocator strategy $\#4$

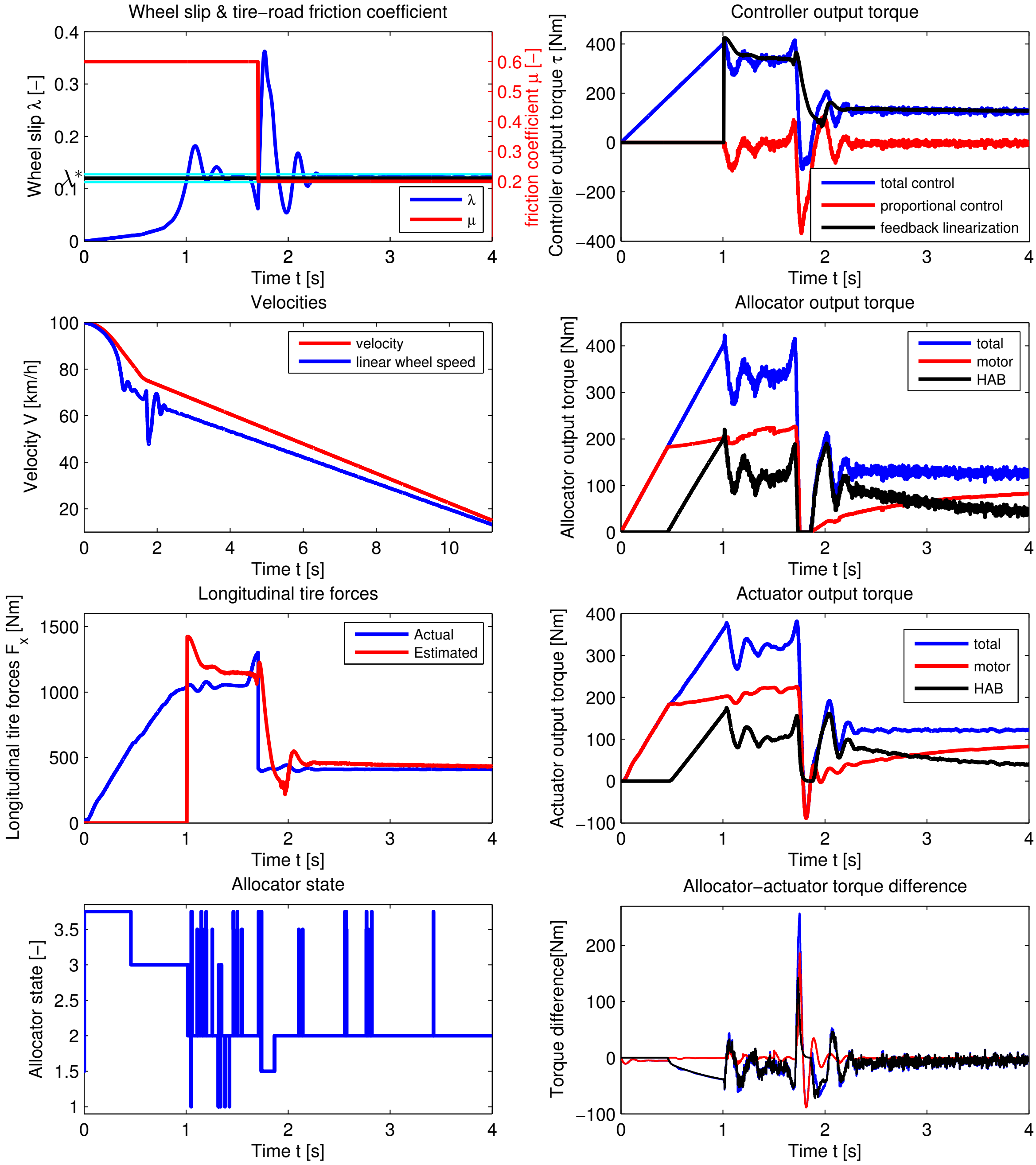

**Figure B-15:** Braking on a $\mu$-jump track ($\mu_{\max} = 0.6 \to \mu_{\max} = 0.2$) using allocator strategy $\#5$

# Bibliography

[1] J. Miller, *Propulsion Systems for Hybrid Vehicles.* The Institution of Electrical Engineers, 2004.

[2] M. Ehsani, *Modern Electric, Hybrid Electric, and Fuel Cell Vehicles.* CRC Press, 2010.

[3] F. Wang and B. Zhuo, "Regenerative braking strategy for hybrid electric vehicles based on regenerative torque optimization control," *Proceedings of the Institution of Mechanical Engineers, Part D: Journal of Automobile Engineering*, pp. 499–513, 2008.

[4] Y. Chen and J. Wang, "Fast and global optimal energy-efficient control allocation with applications to over-actuated electric ground vehicles," *Control Systems Technology, IEEE Transactions on*, vol. 20, no. 5, pp. 1202–1211, 2012.

[5] R. de Castro, R. Araujo, M. Tanelli, S. Savaresi, and D. Freitas, "Torque blending and wheel slip control in evs with in-wheel motors," *Vehicle System Dynamics*, vol. 50, pp. 71–94, 2012.

[6] R. de Castro, R. Araujo, and D. Freitas, "Wheel slip control of evs based on sliding mode technique with conditional integrators," *IEEE Transactions on Industrial Electronics.*

[7] M. Ringdorfer and M. Horn, "A robust wheel slip controller for a hybrid braking system," *World Academy of Science, Engineering and Technology*, vol. 59, pp. 1693–1697, 2011.

[8] K. Bayindir, M. Gözüküçük, and A. Teke, "A comprehensive overview of hybrid electric vehicle: Powertrain configurations, powertrain control techniques and electronic control units," *Energy Conversion and Management*, vol. 52, pp. 1305–1313, 2011.

[9] Mechanical Simulation Corporation, *CarSim Quick Start Guide Version 8*, 2011.

[10] S. Savaresi, *Active Braking Control Systems Design For Vehicles.* Springer, 2010.

[11] C. C. de Wit, P. Tsiotras, E. Velenis, M. Basset, and G. Gissinger, "Dynamic friction models for road/tire longitudinal interaction," *Vehicle System Dynamics (Draft).*

[12] H. Pacejka, *Tyre and Vehicle Dynamics.* Butterworth-Heinemann, 2002.

[13] U. Kiencke and L. Nielsen, *Automotive Control Systems.* Springer, 2005.

[14] R. de Castro, R. Araujo, and D. Freitas, "Optimal linear parametrization for on-line estimation of tire-road friction," in *IFAC World Congress.*

[15] M. Tanelli, A. Astolfi, and S. Savaresi, "Robust nonlinear output feedback control for brake by wire control systems," *Automatica*, vol. 44, pp. 1078–1087, 2008.

[16] T. Johansen, I. Petersen, J. Kalkkuhk, and J. Ludemann, "Gain-scheduled wheel slip control in automotive brake systems," *IEEE Transactions On Control Systems Technology*, vol. 11, pp. 799–811, 2003.

[17] S. Kerst, "Design and implementation of a novel force and brake pressure based anti-lock braking system," Master's thesis, Delft University of Technology.

[18] M. Kuang, M. Fodor, D. Hrovat, and M. Tran, "Hydraulic brake system modeling and control for active control of vehicle dynamics," in *Proceedings of the American Control Conference*, pp. 4538–4542, 1999.

[19] J. Gerdes and J. Hedrick, "Brake system modeling for simulation and control," *Transactions of the ASME*, vol. 121, pp. 496–503, 1999.

[20] H. Jang, K. Ko, S. Kim, R.H.Basch, and J. Fash, "The effect of metal fibers on the friction performance of automotive brake friction materials," *Wear*, vol. 256, no. 3âĂŞ4, pp. 406 – 414, 2004.

[21] V. Milanés, C. González, J. Naranjo, E. Onieva, and T. D. Pedro, "Electro-hydraulic braking system for autonomous vehicles," *International Journal of Automotive Technology*, vol. 11.

[22] L. Guzella and A. Sciaretta, *Vehicle Propulsion Systems - Introduction to Modeling and Optimization.* Springer, 2005.

[23] P. Wellstead and N. Pettit, "Analysis and redesign of an antilock brake system controller," *IEE Proceedings on Control Theory and Applications*, vol. 144, pp. 413–426, 1997.

[24] W. Pasillas-Lépine, "Hybdrid modeling and limit cycle analysis for a class of five-phase anti-lock brake algorithms," *Vehicle system dynamics*, vol. 44, pp. 173–188, 2006.

[25] M. Corno, M. Gerard, M. Verhaegen, and E. Holweg, "Hybrid abs control using force measurement," *IEEE Transactions on Control Systems Technology*, vol. 20, pp. 1223–1235, 2012.

[26] I. Petersen, *Wheel Slip Control in ABS Brakes using Gain Scheduled Optimal Control with Constraints.* PhD thesis, Norwegian University of Science and Technology Trondheim, 2003.

[27] M. Amodeo, "Wheel slip control via second-order sliding-mode generation," *IEEE Tansactions on Intelligent Transportation Systems*, vol. 11, pp. 122–131, 2010.

[28] M. Tanelli, C. Vecchio, M. Corno, A. Ferrara, and S. Savaresi, "Traction control for ride-by-wire sport motorcycles: A second-order sliding mode approach," *IEEE Transactions on Industrial Electronics*, vol. 56, pp. 3347–3356, 2009.

[29] T. Johansen and T. Fossen, "Control allocation - a survey," *Automatica*, vol. 49, pp. 1087–1103, 2013.

[30] M. Oppenheimer, D. Doman, and M. Bolender, "Control allocation for over-actuated systems," in *Control and Automation, 2006. MED '06. 14th Mediterranean Conference on*, pp. 1–6, 2006.

[31] Y. Luo, A. Serrani, S. Yurkovich, D. Doman, and M. Oppenheimer, "Dynamic control allocation with asymptotic tracking of time-varying control input commands," in *American Control Conference, 2005. Proceedings of the 2005*, vol. 3, pp. 2098–2103, 2005.

[32] O. Härkegård, "Dynamic control allocation using constrained quadratic programming," *Journal of Guidance, Control, and Dynamics*, vol. 27, pp. 1028–1034, 2004.

# Glossary

## List of Acronyms

| | |
|---|---|
| **ABS** | Anti-lock Braking System |
| **ESP** | Electronic Stability Program |
| **TCS** | Traction Control System |
| **HAB** | Hydraulic Actuated Brake |
| **QCM** | quarter car model |
| **ICE** | internal combustion engine |
| **SOSM** | second-order sliding-mode |
| **SQP** | sequential quadratic programming |
| **RMS** | root mean square |